

國立交通大學

機械工程學系

博士論文

奈秒脈衝Nd:YAG雷射系統於光電材料

表面製程之應用與研究



**Application and Study on Surface Process of Optoelectric  
Materials by a Nanosecond Pulsed Nd:YAG Laser System**

研究生：曾釋鋒

指導教授：周長彬 教授

中華民國一百年九月

奈秒脈衝 Nd:YAG 雷射系統於光電材料表面製程之應用與研究

Application and Study on Surface Process of Optoelectric Materials by a  
Nanosecond Pulsed Nd:YAG Laser System

研究生：曾釋鋒

Student : Shih-Feng Tseng

指導教授：周長彬

Advisor : Chang-Pin Chou

國立交通大學  
機械工程學系  
博士論文



Submitted to Department of Mechanical Engineering

College of Engineering

National Chiao Tung University

in partial Fulfillment of the Requirements

for the Degree of

Doctor of Philosophy

in

Mechanical Engineering

September 2011

Hsinchu, Taiwan

中華民國 一 百 年 九 月

# 奈秒脈衝 Nd:YAG 雷射系統於光電材料表面製程之應用與研究

研究生：曾釋鋒

指導教授：周長彬 教授

國立交通大學機械工程學系

## 摘要

近年來透明導電材料、非球面玻璃透鏡和高複雜形狀玻璃基板廣泛應用於 3C 商品(如電腦、通訊和消耗性電子產品)，以滿足光電和半導體產業迅速發展。為了要增加生產速度、降低生產設備沈重投資和減少對環境化學傷害，目前微奈米雷射製程紛紛被廣泛使用，其技術包括雷射剝蝕、雷射銑削、雷射退火、雷射刻紋、雷射處理、雷射沈積等。新穎雷射直寫和雷射背寫技術也被開發應用於材料表面製程。

本研究目的係使用奈秒脈衝 Nd:YAG 雷射系統發展材料表面製程技術應用於光電產業，並瞭解雷射與材料加工之間交互作用關係。在觸控面板電極絕緣研究方面，使用 1064 nm 波長之 Nd:YAG 雷射於氧化銻錫薄膜進行劃線，其薄膜分別鍍製於鈉鈣玻璃(Soda-lime glass)、聚碳酸酯(PC)和環烯烴共聚物(COC)三種不同基板上，薄膜厚度分別為 20 nm、30 nm 和 20 nm。最大雷射功率固定在 2.2 瓦，調整雷射照射時間從 10  $\mu$ s 到 100  $\mu$ s，探討薄膜劃線後寬度、深度和導電特性。另外，藉由掃描式電子顯微鏡、三維共焦雷射掃描顯微鏡、原子力顯微鏡和四點探針量測薄膜表面形貌、表面交互作用、表面粗糙度、光學性質和導電性質。雷射劃線後氧化銻錫薄膜表面形貌量測結果顯示：當雷射照射時間在 10  $\mu$ s 和 20  $\mu$ s 時，雷射劃線路徑上仍有殘留氧化銻錫薄膜；當雷射照射時間在 30  $\mu$ s 到 60  $\mu$ s 間，可獲得較佳品質之雷射劃線；當雷射照射時間大於 60  $\mu$ s 時，聚碳酸酯(PC)和環烯烴共聚物(COC)塑膠基板上雷射劃線薄膜會產生局部燒焦區域，且當雷射照射時間增加時，絕緣線寬度和薄膜電阻率也隨之增加。

矽基板表面粗糙圖案製程研究方面，係調整脈衝 Nd:YAG 雷射不同能量密度和脈衝作用時間，探討表面刻紋之微結構與表面粗糙度。掃描式電子顯微鏡和三維共焦雷射掃

描顯微鏡分別用於量測雷射表面刻紋後之矽基板表面微形貌和表面粗糙度，FTA 188 接觸角量測分析儀用於液珠與刻紋基板間接觸角量測。實驗結果指出：增加雷射密度和雷射脈衝作用時間，使得較多熔渣堆積在這些圖案周圍而形成微火山口，且會增加火山口高度和表面粗糙度。水滴在雷射刻紋後矽基板表面之典型例子顯示：水滴非常迅速攤開，幾乎在 0.5167 秒內就完全消失不見；相較於水滴在未經過雷射刻紋處理之表面，其接觸角為 47.9 度。另外，脈衝 Nd:YAG 雷射搭配雷射誘發背寫製程和雷射誘發電漿輔助剝蝕技術，用於鈉鈣玻璃表面加工粗糙陣列圖案。實驗結果顯示：隨雷射加工次數和單發雷射曝曬時間增加，加工後表面形成之火山口高度和深度也會增加。接著在雷射背寫加工後玻璃表面鍍製一層 695 nm 鐵氟龍薄膜後，其表面變成疏水特性。水滴在玻璃基板鍍製鐵氟龍薄膜表面之典型例子顯示：其水滴接觸角為 118.6 度；當水滴在環形溝槽樣板鍍製一層鐵氟龍薄膜，其水滴接觸角提高至 131.3 度。

Nd:YAG 雷射表面處理技術應用於玻璃模造模仁保護膜方面研究，係使用離子源輔助磁控濺鍍系統鍍製不同合金薄膜成分，包括鉑(25%)-鈹、鉑(50%)-鈹、鉑(75%)-鈹、鎳(25%)-鈹、鎳(50%)-鈹和鎳(75%)-鈹合金。在合金薄膜與碳化鎢模仁表面間鍍製一層鉻膜當作緩衝層，接著 Nd:YAG 雷射直接應用於表面處理製程，探討合金膜於高溫環境下之表面性質。在雷射表面處理 1500°C 後，當鉑和鎳成分增加時，表面粗糙度也隨之增加。因薄膜受到高溫工作環境而產生氧化，這些薄膜表面是較粗糙、低微硬度和低彈性模數。因此，建議這些鈹合金薄膜在真空環境和填充保護氣體操作對玻璃模造製程是有益的，可避免嚴重表面氧化和降低表面粗糙度值。

**關鍵字：**脈衝 Nd:YAG 雷射、電極絕緣、雷射劃線、氧化銻錫薄膜、表面刻紋技術、接觸角、雷射誘發背寫、雷射誘發電漿輔助剝蝕、鐵氟龍薄膜、保護膜、鉑-鈹合金、鎳-鈹合金、表面處理、玻璃模造模仁、表面氧化

# **Application and Study on Surface Process of Optoelectric Materials by a Nanosecond Pulsed Nd:YAG Laser System**

Student : Shih-Feng Tseng

Advisors : Prof. Chang-Pin Chou

Department of Mechanical Engineering  
National Chiao Tung University

## **ABSTRACT**

In recent years, transparency conductive materials, aspheric glass lenses, and glass plates of highly complex shape with fine edges were extensively used in 3C market products (i.e. computer, communication, and consumer electronics) to meet the rapid development of the electro-optical and semiconductor industry. In order to increase the processing speeds, to reduce the heavy investment of the processing equipment, and to decrease the chemical harm to the environment, current laser micro- or nano-machining processes employ techniques including laser ablation, laser milling, laser annealing, laser texturing, laser treatment, laser deposition, etc. Moreover, novel techniques, laser direct writing and laser backside writing methods, are also developed to use in the surface process of materials.

The purposes of this dissertation aim to develop the surface processing techniques on materials used for the optoelectric applications by a nanosecond pulsed Nd:YAG laser system and to better understand the interaction between laser beam and materials. In the electrode isolation for touch panels, the Nd:YAG laser with wavelength of 1064 nm is used to scribe the indium tin oxide (ITO) thin films coated on three types of substrate materials, i.e. soda-lime glass, polycarbonate (PC), and cyclic-olefin-copolymer (COC) materials with thickness of 20 nm, 30 nm, and 20 nm, respectively. The effect of exposure time adjusted from 10  $\mu$ s to 100  $\mu$ s on the ablated mark width, depth, and electrical properties of the scribed film was investigated. The maximum laser power of 2.2 watts was used to scribe these thin films. In addition, the surface morphology, surface reaction, surface roughness, optical properties, and electrical conductivity properties were measured by a scanning electron

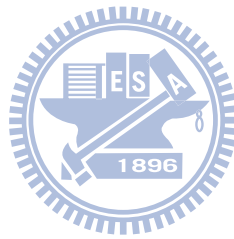
microscope, a three-dimensional confocal laser scanning microscope, an atomic force microscope, and a four-point probe. After laser scribing, the measured results of surface morphology show that the residual ITO layer was produced on the scribed path with the laser exposure time at 10  $\mu\text{s}$  and 20  $\mu\text{s}$ . The better edge qualities of the scribed lines can be obtained when the exposure time extends from 30  $\mu\text{s}$  to 60  $\mu\text{s}$ . When the laser exposure time is longer than 60  $\mu\text{s}$ , the partially burned areas of the scribed thin films on PC and COC substrates are observed. Moreover, the isolated line width and resistivity values increase when the laser exposure time increases.

In a surface-texturing technique to create rough patterns on a silicon substrate by the pulsed Nd:YAG laser system, the different degrees of microstructure and surface roughness were adjusted by the laser fluence and laser pulse duration. A scanning electron microscope (SEM) and a 3D confocal laser scanning microscope are used to measure the surface micrograph and roughness of the patterns, respectively. The contact angle variations between droplets on the textured surface were measured using an FTA 188 video contact angle analyzer. The results indicate that increasing the values of laser fluence and laser pulse duration pushes more molten slag piled around these patterns to create micro-sized craters and leads to an increase in the crater height and surface roughness. A typical example of a droplet on a laser-textured surface shows that the droplet spreads very quickly and almost disappears within 0.5167 s, compared to a contact angle of  $47.9^\circ$  on an untextured surface. In addition, the pulsed Nd:YAG laser is also utilized to fabricate rough array-patterns on a soda-lime glass plate by a laser-induced backside writing (LIBW) process and a laser-induced plasma assisted ablation (LIPAA) technique. The measured results show that crater height and depth gradually increases with increasing number of passes and single-shot laser exposure time. After a 695 nm thick Teflon thin film is deposited on the glass plate, the micro-machined template surface becomes hydrophobic. The typical measured contact angle on a planar glass substrate coated with Teflon is  $118.6^\circ$ . The contact angle increases to  $131.3^\circ$  when the water drop is added on a round annular-grooved template coated with Teflon.

In the Nd:YAG laser surface treatment technology for the protective coatings of glass-molding dies, a variety of alloy films, including Ir-25 at.% Pt, Ir-50 at.% Pt, Ir-75 at.% Pt, Ir-25 at.% Ni, Ir-50 at.% Ni, and Ir-75 at.% Ni compositions are deposited by the ion source assisted magnetron sputtering system (ISAMSS). A Cr layer that functioned as a buffer layer is deposited between the alloy film and die surface. After an alloy film and the buffer Cr layer were sequentially coated on tungsten carbide (WC) surface, Nd:YAG laser was directly

applied in the surface treatment process. The temperature profile of the film stacks structure is simulated by ANSYS software. After laser surface treatment at 1500°C, the values of surface roughness are obviously increased as increasing concentrations of Pt or Ni. These surface films are high roughness, low microhardness and low reduced modulus because of the film oxidation occurred in high working temperature process. Therefore, these Ir-alloy coatings operated under the vacuum environment and filled with protective gas are useful in glass molding to avoid the severe surface oxidation and to reduce surface roughness.

**Keywords:** *Pulsed Nd:YAG laser, electrode isolation, laser scribing, indium tin oxide (ITO) thin films, surface-texturing technique, contact angle, laser-induced backside writing (LIBW), laser-induced plasma assisted ablation (LIPAA), Teflon thin film, protective coatings, Pt-Ir alloy, Ni-Ir alloy, surface treatment, glass-molding die, surface oxidation.*



## 誌謝

感謝指導教授周長彬博士在我博士班就讀期間的悉心指導與關懷，使學生在雷射加工與材料分析專業領域受益良多，且順利完成博士論文研究。師恩浩瀚，永銘我心，特誌卷首，謹致上衷心之謝忱。

感謝交通大學機械系鄭璧瑩副教授、台北科技大學機械系湯華興教授、彰化師範大學機電系陳明飛教授和國研院儀器科技研究中心黃國政博士，撥冗擔任博士論文口試委員，並於口試過程中提供寶貴意見及斧正，使論文內容能更臻完整。

感謝國研院儀器科技研究中心蔣東堯博士和蕭文澤博士，對於研究期間給予論文指導與討論，使論文發表更加順利。感謝儀科中心同事李昭德博士、陳維鈞先生、蘇健穎先生、朱念南小姐、卓文浩先生、光學廠與機械廠同仁，於研究期間對實驗試片量測與加工之協助。感謝彰化師範大學機電系陳明飛教授提供 Nd:YAG 雷射實驗設備，感謝龍華科技大學工程技術研究所丁鯤教授提供奈米壓痕量測儀，及實驗室同學建堯和治豪、學弟彥彬和治偉在研究期間的協助，使論文得以順利完成，在此，謹致上最誠摯的謝意。

最後，感謝父母、老婆及家人在求學過程中，給予最大的支持與鼓勵，讓我在無後顧之憂的環境下，全力以赴的完成學業，謹獻上內心無限的感激。



曾釋鋒 謹識

中華民國一百年九月



# Contents

|   |     |
|---|-----|
| Abstract (in Chinese).....  | i   |
| Abstract (in English).....  | iii |
| Acknowledgements (in Chinese).....  | vi  |
| Contents.....   | vii |
| Table captions.....   | x   |
| Figure captions.....  | ix  |
| Chapter 1 Introduction.....   | 1   |
| 1.1 Backgrounds.....  | 1   |
| 1.1.1 Electrode forming of TCO thin films.....  | 3   |
| 1.1.2 Wettability of material surfaces.....   | 5   |
| 1.1.3 Hard coatings for glass-molding dies.....   | 7   |
| 1.2 Motivation and objectives.....  | 9   |
| 1.3 Structure of the dissertation.....  | 10  |
| Chapter 2 Literatures review.....   | 12  |
| 2.1 Laser scribing of TCO thin films.....   | 12  |
| 2.2 Wetting effects of various textured surfaces.....   | 18  |
| 2.3 Protective coating compositions for glass-molding dies.....   | 26  |
| 2.4 Laser treatment technology of material surfaces.....  | 29  |
| Chapter 3 Laser processing mechanisms and parameters.....   | 32  |
| 3.1 Laser processing mechanisms.....  | 32  |
| 3.1.1 Laser radiation absorption mechanisms.....  | 32  |
| 3.1.2 Laser direct writing and laser-induced backside writing.....  | 34  |
| 3.2 Laser processing parameters.....  | 36  |
| Chapter 4 Experimental apparatus and sample preparation.....  | 39  |
| 4.1 Laser scribing of indium tin oxide (ITO) thin films deposited on various substrates for touch panels..... | 39  |
| 4.1.1 Laser scribing system.....  | 39  |
| 4.1.2 Sample preparation.....   | 40  |
| 4.1.3 Isolation line patterning parameter.....  | 45  |
| 4.2 Surface wettability of silicon substrates enhanced by laser ablation.....                                 | 45  |
| 4.2.1 Apparatus and sample.....   | 45  |

|           |  |    |
|-----------|--|----|
| 4.2.2     | Surface texturing by laser ablation.....   | 47 |
| 4.2.3     | Wettability characteristics of the textured surfaces.....  | 48 |
| 4.3       | Hydrophobic templates with rough patterns fabricated by laser micromachining for liquid droplets generation..... | 49 |
| 4.3.1     | Laser micromachining system.....   | 49 |
| 4.3.2     | Templates made by hydrophobic processes.....   | 50 |
| 4.4       | Characteristics of Ni-Ir and Pt-Ir hard coatings surface treated by pulsed Nd:YAG laser irradiation.....         | 52 |
| 4.4.1     | Numerical simulation process.....  | 52 |
| 4.4.2     | Laser surface treatment system.....  | 54 |
| 4.4.3     | Sample preparation.....  | 55 |
| Chapter 5 | Experimental results and discussion.....   | 57 |
| 5.1       | Laser scribing of indium tin oxide (ITO) thin films deposited on various substrates for touch panels.....        | 57 |
| 5.1.1     | Surface morphology, isolation line width, and depth.....   | 57 |
| 5.1.2     | Electrical conductivity measurement.....   | 63 |
| 5.1.3     | Summary.....   | 64 |
| 5.2       | Surface wettability of silicon substrates enhanced by laser ablation.....  | 64 |
| 5.2.1     | Square patterning on silicon substrates.....   | 64 |
| 5.2.2     | Surface morphologies.....  | 65 |
| 5.2.3     | Surface roughness.....   | 69 |
| 5.2.4     | Enhanced wettability of liquid droplets on laser textured surfaces.....  | 69 |
| 5.2.5     | Summary.....   | 70 |
| 5.3       | Hydrophobic templates with rough patterns fabricated by laser micromachining for liquid droplets generation..... | 71 |
| 5.3.1     | Surface morphologies of machined templates.....  | 71 |
| 5.3.2     | Surface profiles of machined templates.....  | 73 |
| 5.3.3     | Contact angle of water droplets on the hydrophobic template.....   | 75 |
| 5.3.4     | Summary.....   | 76 |
| 5.4       | Characteristics of Ni-Ir and Pt-Ir hard coatings surface treated by pulsed Nd:YAG laser irradiation.....         | 77 |
| 5.4.1     | SEM observations on different composition alloy films.....   | 77 |
| 5.4.2     | The temperature distribution profile of the different composition alloy films.....                               | 77 |
| 5.4.3     | Description of surface roughness of Pt-Ir and Ni-Ir films treated by laser                                       |    |

|   |     |
|---|-----|
| annealing.....  | 79  |
| 5.4.4 Oxidation analysis using EDS.....               | 81  |
| 5.4.5 Microhardness and reduced modulus property..... | 83  |
| 5.4.6 Summary.....                                    | 83  |
| Chapter 6 Conclusions and future work.....            | 86  |
| 6.1 Conclusions.....                                  | 86  |
| 6.2 Future work.....                                  | 88  |
| References.....                                       | 89  |
| Vita.....   | 98  |
| Publications.....                                     | 100 |

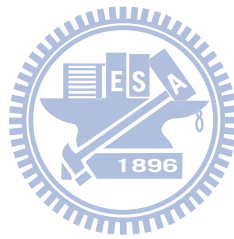


## Table captions

|   |    |
|---|----|
| Table 4.1 Fundamental Nd:YAG laser system parameters.....                                     | 40 |
| Table 4.2 Optical and electrical properties of ITO film deposited on different substrates ... | 42 |
| Table 4.3 Physical characteristics of Tungsten carbide (WC) mold for glass molding.....       | 54 |
| Table 5.1 Machining parameters of the annular groove and measured results.....                | 72 |
| Table 5.2 Summarized table of processing parameters for laser treatment.....                  | 79 |
| Table 5.3 Comparison of surface roughness before and after laser treatment.....               | 80 |

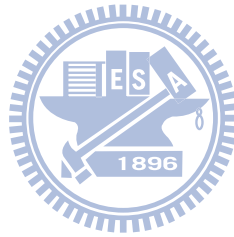


## Figure captions

|   |    |
|---|----|
| Figure 1.1 Common high-power laser sources for industry.....  | 2  |
| Figure 1.2 Long-pulse laser matter interaction [1].....   | 2  |
| Figure 1.3 Short-pulse laser matter interaction [2].....  | 2  |
| Figure 1.4 Products of touch panel application. (a) Elonex e-Book reader [9] and (b) Apple iPhone [10].....   | 3  |
| Figure 1.5 Schematic diagram of fundamental structure for resistive touch panel [11].....   | 4  |
| Figure 1.6 Semiconductor processes for patterning electrodes of transparent conductive oxide ...  | 5  |
| Figure 1.7 Schematic diagram of a wettable surface [13]. (a) Superhydrophobic surface, (b) hydrophobic surface, and (c) hydrophilic surface .....   | 6  |
| Figure 1.8 Products of surface wettability application [22]. (a) Digital microfluidic biochip and (b) multifunctional biochemical detection biochip system .....  | 6  |
| Figure 1.9 Pictures of a glass-molding system [23]. (a) Glass-molding machine of Toshiba-GMP207HV and (b) glass-molding die .....   | 8  |
| Figure 1.10 Flow diagram for glass-molding processes [24].....  | 8  |
| Figure 1.11 Application of glass-molding process for fabricating various lenses [24] .....  | 9  |
| Figure 2.1 SEM images of Ag/Au pattern (a), Al/Ag pattern (b), edge-peeled Al/Ag stripe pattern fabricated by two-beam interference (c), and micro-tubes formed by furtherincreasing the pulse power (d) [26] ..... | 13 |
| Figure 2.2 Schematic illustration of high-resolution ITO patterning process [27] .....  | 14 |
| Figure 2.3 Optical profiler images of patterned Au (top) and ITO (bottom) films (a) and ITO patterns created using holographically patterned Al layers (b) [29].....  | 14 |
| Figure 2.4 Ablation depths and widths at different fluences measured by increasing the number of laser pulses [34].....   | 15 |
| Figure 2.5 UV laser direct writing of ITO thin films with different feed rates [35] .....   | 16 |
| Figure 2.6 Schematic diagram of laser beam transmittance [36] .....   | 17 |
| Figure 2.7 SEM images of the surface morphology of ablated by the Nd:YAG laser at different overlapping rate: (a) 0%, (b) 25%, and (c) 62% [38] .....   | 18 |
| Figure 2.8 Pictures of 1 mg water droplets on prepared pillar structures [18].....  | 19 |
| Figure 2.9 Spreading-process images of water droplets with different impact conditions on the hydrophobic grooved surface [40].....   | 20 |
| Figure 2.10 SEM photos of the textured surfaces fabricated by using the standard lithography process, (a) chain-configuration and (b) concentric circular configuration [47].....                                   | 21 |

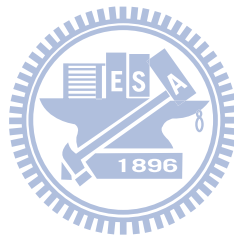
|  |    |
|--|----|
| Figure 2.11 Dynamic motion of a droplet on a separated route [47].....   | 21 |
| Figure 2.12 FESEM images (top), EDX analysis spectra (middle), and water contact angles (bottom) of various nanopatterned aluminum films [48].....   | 22 |
| Figure 2.13 Variation in roughness factor (a) and critical wetting angle with laser fluence for groove and pillar patterns (b) [49].....   | 23 |
| Figure 2.14 System of two immiscible liquids with suppressed evaporation and accurate positioning of the aqueous liquid: (a) schematic diagram of laser-ablated patterns and (b) picture of a water droplet contained within hexadecane [50].....                | 24 |
| Figure 2.15 SEM images of a natural lotus leaf (a, b) and SEM images of laser-ablated micro- and nano-structures and ripple formation (d, e) [54].....   | 26 |
| Figure 2.16 Cross-sectional micrographs of Cr, Pt-Ir and Ni-Ir coatings [56]. (a) Pt-Ir 1 (27.67 at.% Pt), (b) Pt-Ir 2 (55.25 at.% Pt), (c) Pt-Ir 3 (79.42 at.% Pt), (d) Ni-Ir 1 (26.10 at.% Ni), (e) Ni-Ir 2 (51.44 at.% Ni), (f) Ni-Ir 3 (73.45 at.% Ni) ..... | 27 |
| Figure 2.17 Cross-sectional micrographs of chromium nitride based coatings [57]. (a) CrN and (b) CrWN4 (16.7 at.% W) .....   | 28 |
| Figure 2.18 Cross-sectional TEM images of (a) Mo <sub>56.7</sub> Ru <sub>43.3</sub> /Cr/Ti(O)/WC deposit and (b) detailed structure of the oxide scale, the transition zone, and the columnar grains [59] .....  | 29 |
| Figure 2.19 Temperature distributions at welding procedure of laser diode pump on erbium doped fiber amplifier [62] .....  | 30 |
| Figure 2.20 Cross-sectional views of the alloyed layer textured with different laser power: (a) P = 500 W, (b) P = 700 W, (c) P = 900 W [65].....  | 31 |
| Figure 3.1 Schematic diagram of Beer-Lambert absorption of an incident light.....  | 32 |
| Figure 3.2 Sequence diagrams of absorption events varying with absorbed energy.....  | 34 |
| Figure 3.3 Schematic of laser direct writing (a) and laser-induced backside writing (b).....   | 35 |
| Figure 3.4 Schematic diagram of laser pulse output parameters.....   | 37 |
| Figure 3.5 Characteristics of a focusing laser beam .....  | 38 |
| Figure 4.1 Schematic diagram of Nd:YAG laser system .....  | 39 |
| Figure 4.2 Dimensions and shapes of cell phone touch panels used in this study .....   | 41 |
| Figure 4.3 SEM cross-section views of ITO films deposited on different types of substrates. (a) ITO/Glass, (b) ITO/PC, and (c) ITO/COC.....  | 42 |
| Figure 4.4 Surface roughnesses of different substrates and ITO films deposited on substrates. (a) Soda-lime glass substrate, (b) PC substrate, (c) COC substrate, (d) ITO/Glass, (e) ITO/PC, and (f) ITO/COC.....  | 43 |

|  |    |
|--|----|
| Figure 4.5 A photo of a spectrometer (Lambda 900 UV/Vis/NIR) [71] .....  | 44 |
| Figure 4.6 Light transmittance and reflectance versus wavelength for ITO thin film at various substrates .....   | 44 |
| Figure 4.7 A photo of a 3D laser confocal microscope (KEYENCE VK-9700, Japan) .....  | 44 |
| Figure 4.8 A photo of a four-point probe measurement system (QUATEK CH-5601Y) .....  | 45 |
| Figure 4.9 Schematic diagram of the Nd:YAG laser set-up.....   | 46 |
| Figure 4.10 A photo of a FTA 188 video contact angle analyzer [72].....  | 47 |
| Figure 4.11 The illustration of laser ablation path.....   | 47 |
| Figure 4.12 Cross-sectional view of the droplet on target surfaces.....  | 49 |
| Figure 4.13 Schematic representation of the Nd:YAG laser process set-up for backside writing process.....  | 50 |
| Figure 4.14 Major fabricated processes of the hydrophobic template. (a) Polished soda-lime glass substrate on top and bottom surfaces, (b) laser-induced backside writing process on glass backside surface, (c) Teflon thin film coating, and (d) template top view ..... | 51 |
| Figure 4.15 Schematic of the cross-section view of the droplet on a machined template .....  | 52 |
| Figure 4.16 The experimental setup of the Nd:YAG laser system .....  | 54 |
| Figure 4.17 A photo of an atomic force microscope (Veeco di Dimension 3100, USA).....  | 55 |
| Figure 4.18 A photo of a field emission scanning electron microscope (FESEM, Model JEOL JSM-7401F).....  | 56 |
| Figure 4.19 A photo of a nanoindentation tester (Hysitron TriboLab, USA) [77] .....  | 56 |
| Figure 5.1 Pictures of laser scribing of isolated lines on different substrates.....   | 57 |
| Figure 5.2 Surface morphologies of laser scribing of isolated lines at laser exposure time of 10 $\mu$ s and 20 $\mu$ s on different types of substrates coated indium tin oxide thin films. (a) ITO/Glass, (b) ITO/PC, and (c) ITO/COC.....                               | 59 |
| Figure 5.3 Surface morphologies of laser scribing of isolated lines at laser exposure time of 30 $\mu$ s and 60 $\mu$ s on different types of substrates coated indium tin oxide thin films. (a) ITO/Glass, (b) ITO/PC, and (c) ITO/COC.....                               | 60 |
| Figure 5.4 Surface morphologies of laser scribing of isolated lines at laser exposure time of 70 $\mu$ s and 100 $\mu$ s on different types of substrates coated indium tin oxide thin films. (a) ITO/Glass, (b) ITO/PC, and (c) ITO/COC.....                              | 61 |
| Figure 5.5 Relationship of isolated line width and depth on various exposure times. (a) Isolated line width versus different laser exposure time, and (b) isolated line depth versus different laser exposure time .....   | 62 |
| Figure 5.6 Electrical properties of ITO thin films coated on glass, PC, and COC with un-scribing   |    |

|   |    |
|---|----|
| and after laser scribing at different laser exposure time .....   | 63 |
| Figure 5.7 Optical characteristics of untextured silicon substrate.....   | 65 |
| Figure 5.8 Some examples for laser-ablated squares on silicon substrate under different test parameters. (a) $F=49.5 \text{ J/cm}^2$ , $Pd=100 \text{ }\mu\text{s}$ , (b) $F=53.8 \text{ J/cm}^2$ , $Pd=100 \text{ }\mu\text{s}$ , (c) $F=11.8 \text{ J/cm}^2$ , $Pd=300 \text{ }\mu\text{s}$ , (d) $F=53.8 \text{ J/cm}^2$ , $Pd=300 \text{ }\mu\text{s}$ , (e) $F=53.8 \text{ J/cm}^2$ , $Pd=500 \text{ }\mu\text{s}$ ..... | 65 |
| Figure 5.9 SEM micrographs showing the effect of laser pulse duration on surface structures at $F=53.8 \text{ J/cm}^2$ : (a) $Pd=100 \text{ }\mu\text{s}$ , (b) $Pd=300 \text{ }\mu\text{s}$ , (c) $Pd=500 \text{ }\mu\text{s}$ .....   | 66 |
| Figure 5.10 SEM micrographs showing the effect of laser fluence on surface structures at $Pd=300 \text{ }\mu\text{s}$ : (a) $F=17.1 \text{ J/cm}^2$ , (b) $F=29.1 \text{ J/cm}^2$ , (c) $F=37.5 \text{ J/cm}^2$ .....   | 67 |
| Figure 5.11 SEM micrographs showing the effect of laser fluence on surface structures at $Pd=500 \text{ }\mu\text{s}$ : (a) $F=29.1 \text{ J/cm}^2$ , (b) $F=42.1 \text{ J/cm}^2$ , (c) $F=92 \text{ J/cm}^2$ .....   | 67 |
| Figure 5.12 Typical 3D confocal laser scanning microscope topographies of texture formed on silicon surface at $F=70.7 \text{ J/cm}^2$ : (a) $Pd=100 \text{ }\mu\text{s}$ , (b) $Pd=300 \text{ }\mu\text{s}$ , (c) $Pd=500 \text{ }\mu\text{s}$ .....   | 68 |
| Figure 5.13 The effect of the laser fluence on the surface roughness for different conditions .....   | 69 |
| Figure 5.14 Comparison with images of spreading liquid droplets on untextured and laser-textured surfaces within $0.516 \text{ s}$ .....  | 70 |
| Figure 5.15 Optical characteristics of soda-lime glass substrate.....   | 72 |
| Figure 5.16 Optical microscope pictures of the annular groove fabricated by various $T_s$ and $N_p$ : (a) $2000 \text{ }\mu\text{s}$ , 20 times, (b) $3000 \text{ }\mu\text{s}$ , 20 times, (c) $2000 \text{ }\mu\text{s}$ , 22.5 times, (d) $3000 \text{ }\mu\text{s}$ , 22.5 times .....  | 72 |
| Figure 5.17 A SEM planar and cross-section image of rough patterned template fabricated by $T_s = 3000 \text{ }\mu\text{s}$ and $N_p = 20$ times.....   | 73 |
| Figure 5.18 A single sided profile of annular groove fabricated by $T_s = 2000 \text{ }\mu\text{s}$ and $N_p = 22.5$ times .....  | 74 |
| Figure 5.19 Plots of the crater height and depth via the three different $T_s$ . (a) Crater height versus $T_s$ and $N_p$ , (b) crater depth versus $T_s$ and $N_p$ .....   | 74 |
| Figure 5.20 A SEM cross-section photograph of a planar glass substrate coated with Teflon thin film.....  | 75 |
| Figure 5.21 The contact angle versus droplet volume relation between the annular-grooved and planar templates coated with thin Teflon .....   | 76 |
| Figure 5.22 Cross-section views of Ni-Ir and Pt-Ir films deposited on silicon substrates observed by SEM. (a) Ir-50 at.% Ni, (b) Ir-50 at.% Pt .....  | 77 |
| Figure 5.23 Optical reflectance versus wavelength for different composition alloys .....  | 78 |
| Figure 5.24 A cross-section view of temperature distribution on WC mold with Ir-25 at.% Ni  |    |



|  |    |
|--|----|
| coating calculated by ANSYS simulation .....   | 79 |
| Figure 5.25 Surface roughness of different alloy coatings after laser surface treatment. The coatings composition are (a) Ir-25 at.% Ni, (b) Ir-50 at.% Ni, (c) Ir-75 at.% Ni, (d) Ir-25 at.% Pt, (e) Ir-50 at.% Pt and (f) Ir-75 at.% Pt..... | 81 |
| Figure 5.26 Oxygen concentration of Pt-Ir and Ni-Ir coatings after laser surface treatment.....  | 82 |
| Figure 5.27 Plot of microhardness testing under different compositions of Pt-Ir and Ni-Ir coatings .....   | 84 |
| Figure 5.28 Plot of reduced modulus testing under different contents of Pt-Ir and Ni-Ir coatings .....   | 85 |



# Chapter 1 Introduction

## 1.1 Backgrounds

With the rapid development of the optoelectric and biomedical industries, the number of applications for transparent conductive oxide (TCO) thin films, aspheric glass lenses, and hydrophobic and hydrophilic templates has increased tremendously, especially in touch screen and disease testing task applications. To reduce heavy investment in processing equipment, minimize chemical impact on the environment, and increase processing speeds, laser dry etching has become an important manufacturing method, and is widely used to remove superfluous materials. Moreover, laser-machining technologies include milling, drilling, cutting, marking, scribing, annealing, and texturing.

Common high-power laser sources for industry include the CO<sub>2</sub> laser, with 10.6 μm and 9.3 μm wavelengths; the Nd:YAG laser, with 1064 nm, 532 nm (doubled), 355 nm (tripled), and 266 nm (4<sup>th</sup> harmonic) wavelengths; the fiber laser, with 1070 nm; and the excimer laser, with wavelengths from 157 nm to 351 nm (figure 1.1). Figure 1.2 to 1.3 show schematic diagrams of the machined results for different laser pulse widths [1,2]. The pulse width for Nd:YAG laser ( $\lambda$ : 1064 nm) is short than for the CO<sub>2</sub> laser ( $\lambda$ : 10.6 μm), thus, the Nd:YAG machined quality, including heat affected zones (HAZs), micro cracks, surface debris, and shock waves, is much better than that produced by CO<sub>2</sub> laser machining. Moreover, the cost of Nd:YAG and CO<sub>2</sub> laser sources are less than others of similar power output. Therefore, manufacturers adopt the nanosecond pulsed Nd:YAG laser for the manufacture of indium tin oxide (ITO) thin films for touch panels, surface texturing of silicon substrates for hydrophilic surface applications, backside writing of glass substrates for hydrophobic surface applications, and surface treatment of hard coatings for glass-molding applications. In this dissertation, a pulsed Nd:YAG laser was used to investigate the mechanical, optoelectric, and surface characteristics of machined specimens.

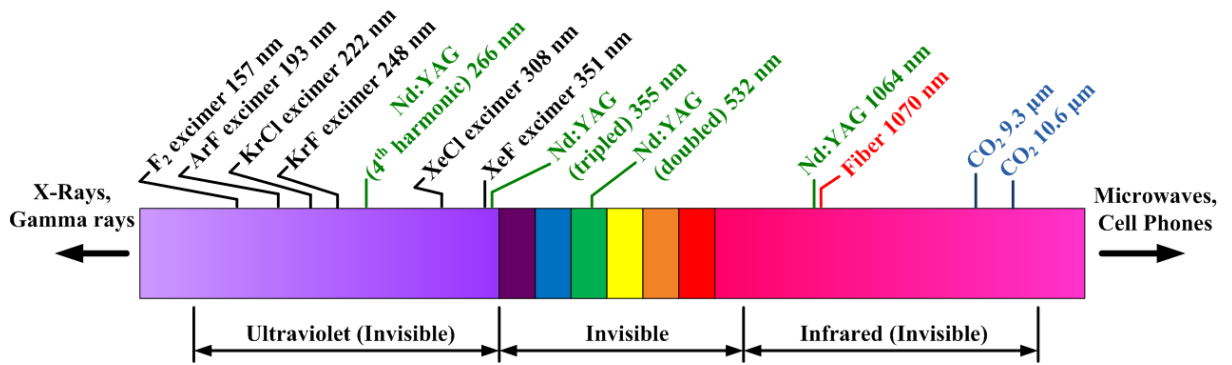


Figure 1.1 Common high-power laser sources for industry.

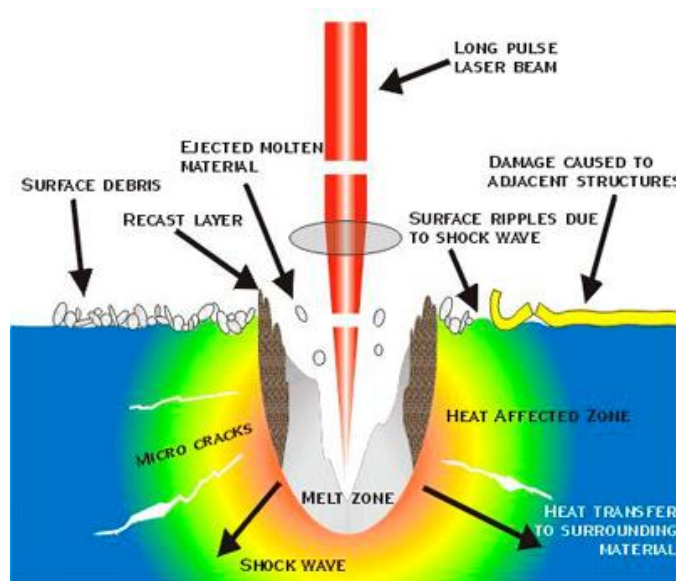


Figure 1.2 Long-pulse laser matter interaction [1].

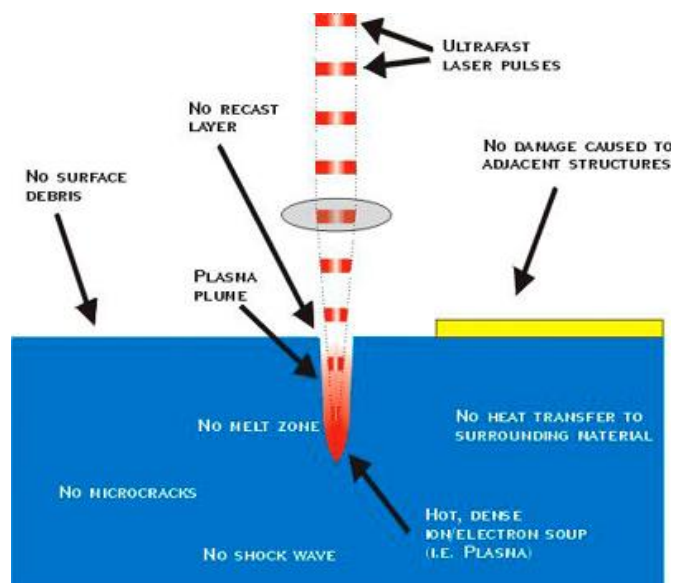


Figure 1.3 Short-pulse laser matter interaction [2].

### 1.1.1 Electrode forming of TCO thin films

In recent years, transparency conductive materials were extensively used in 3C market products (i.e. computer, communication, and consumer electronics) to meet the rapid development of the electro-optical and semiconductor industry. Common transparent conductive oxide thin film materials, such as  $\text{TiO}_2$ ,  $\text{SnO}_2$ ,  $\text{In}_2\text{O}_3$ , and  $\text{ZnO}$  are used. The thin films of  $\text{ZnO}$  composition doped with aluminum, gallium, and tin elements are named aluminum zinc oxide (Al:ZnO), the gallium zinc oxide (Ga:ZnO), and the zinc tin oxide (ZTO) [3] films, respectively. Particularly, among them, indium tin oxide (ITO) material is popularly used in the flat panel display industry. Due to the high optical transparency and better electrical conductivity, ITO films have attracted great interests for various electrode or conductor applications in solar cells [4,5], flat panel displays [6], liquid crystal displays (LCDs) [7], and in organic light emitting diodes [8]. Figure 1.4 shows the touch panel applications including an Elonex e-Book reader and an Apple iPhone [9,10].



Figure 1.4 Products of touch panel application. (a) Elonex e-Book reader [9] and (b) Apple iPhone [10].

In order to fulfill light, thin, short, small, and flexible requirements in the electronic gadgets, plastic substrates are developed and convinced to be better candidates to replace the glass substrate in portable electronic products. The most common used substrate materials include polycarbonate (PC), polyestersulfone (PES), polyethylene terephthalate (PET),

polyimide (PI), polyarylate (PAR), and polyolefin. Figure 1.5 shows the schematic diagram of fundamental structure for resistive touch panel [11]. In the electrode manufacturing process, the transparent conductive material films were coated on these substrates first using the various deposition methods, and then etching the deposited film to become the electrode of the pre-determined pixel sizes.

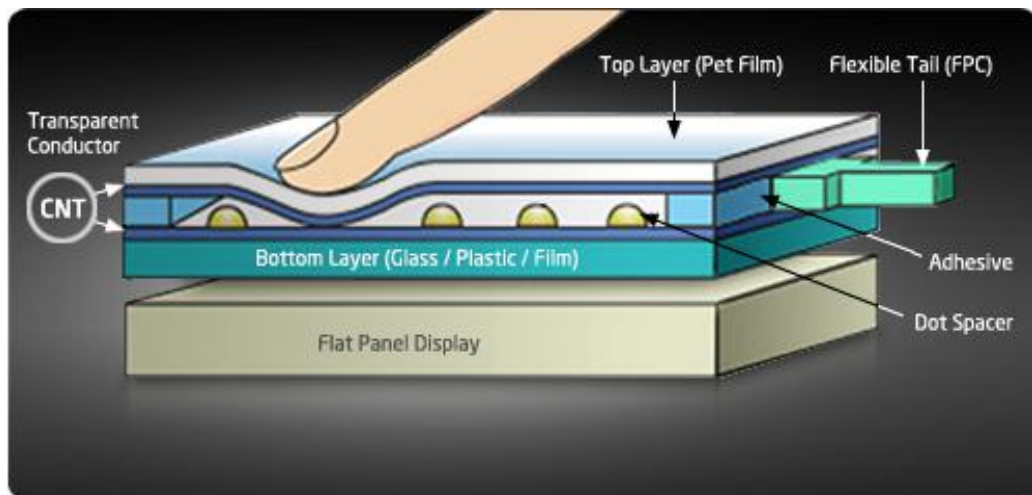


Figure 1.5 Schematic diagram of fundamental structure for resistive touch panel [11].

Traditional electrode patterning techniques used the photolithography and chemical wet etching to form the patterns on the thin deposited films. The film electrodes manufacturing process includes sequentially (a) photoresist coating, (b) soft bake, (c) exposure, (d) lithography, (e) hard bake, (f) etch, and (g) photoresist stripping [12]. Figure 1.6 shows the semiconductor processes for patterning electrodes of transparent conductive oxide. Because of these processes increasing the heavy investment of semiconductor lithography process equipment and the chemical harm to the environment, a novel technique of direct laser writing is applied on the film surface to obtain the designed electrode.

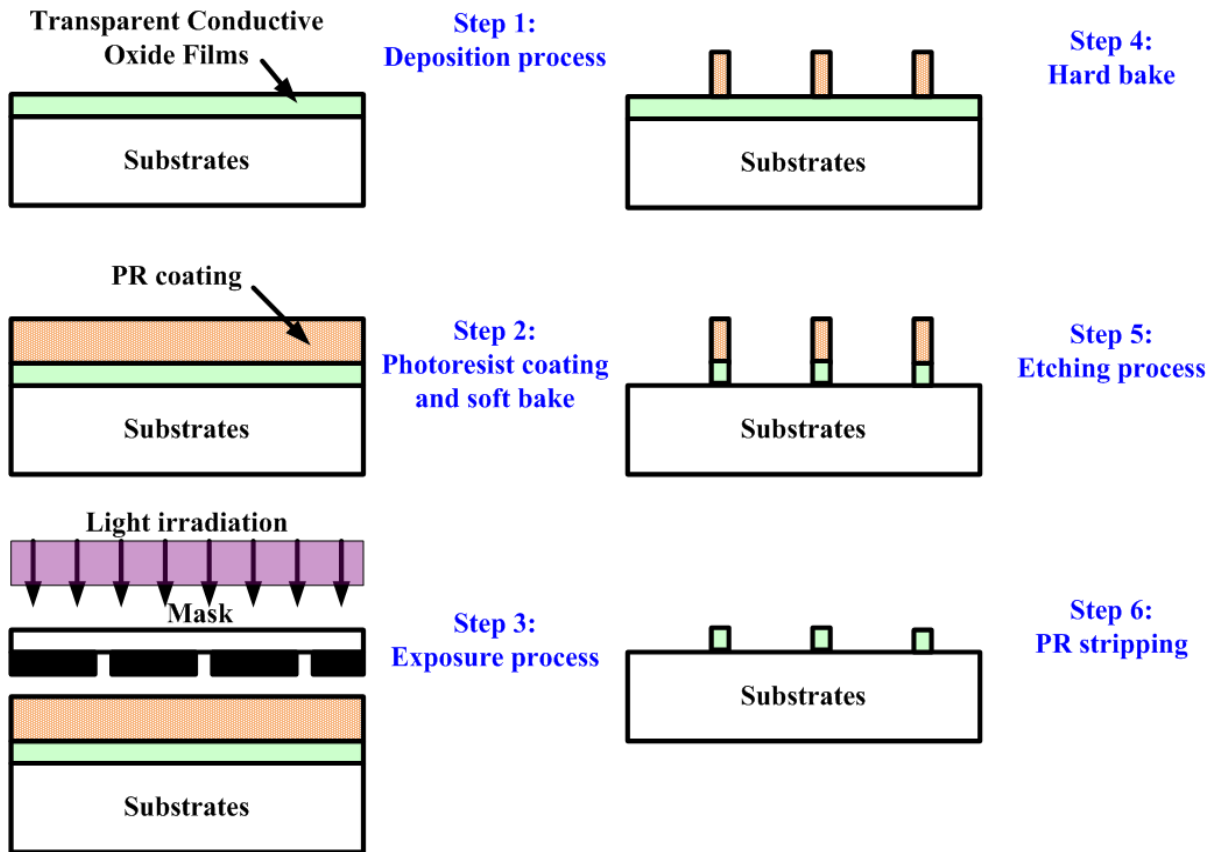


Figure 1.6 Semiconductor processes for patterning electrodes of transparent conductive oxide.

### 1.1.2 Wettability of material surfaces

Wettability is an important characteristic of solid surfaces. Due to continual development in the field of nanotechnology in recent years, a deeper understanding of the relationship between the microstructure of solid surfaces and wettability has been obtained. Wettability can usually be shown through the contact angle between water and a solid surface. Figure 1.7 shows the schematic diagram of a wettable surface [13]. When the contact angle is smaller than  $90^\circ$ , the surface is referred to as a hydrophilic surface, and when the contact angle is greater than  $90^\circ$ , it is referred to as a hydrophobic surface. A solid surface with a contact angle greater than  $150^\circ$  is referred to as a superhydrophobic surface.

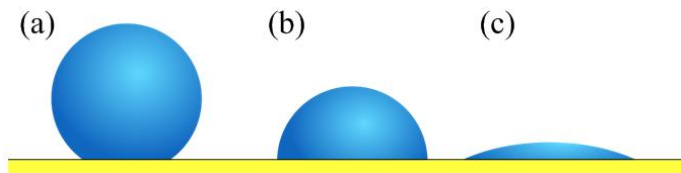


Figure 1.7 Schematic diagram of a wettable surface [13]. (a) Superhydrophobic surface, (b) hydrophobic surface, and (c) hydrophilic surface.

The wettability of a solid surface is decided by the chemical composition and microscopic geometric structure. Under the effects of the solid surface chemical composition, the higher than free energy of the solid surface, the higher the wettability is. The opposite is also true. However, when adjusting the surface free energy using chemical methods, the contact angle cannot usually be increased beyond  $120^\circ$ . In order to achieve a larger contact angle, the surface material must be planned on a microscopic level. The microstructure of the surface must be smaller than the micro-size of the liquid droplet. This micro structure can effectively increase the hydrophilic or hydrophobic qualities of the material. Hydrophobic materials are widely used to prevent pollution [14], prevent corrosion [15], reduce fluid resistance [16-18] and also include self-cleaning mechanisms [19-21]. Hydrophilic materials are widely used to disperse water evenly, dry faster, dissipate static electricity, and resist the dirt and spots. Figure 1.8 shows a digital microfluidic biochip and a multifunctional biochemical detection biochip system for the surface wettability application [22].

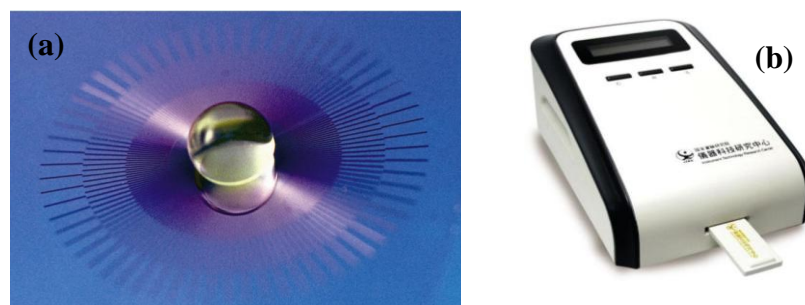


Figure 1.8 Products of surface wettability application [22]. (a) Digital microfluidic biochip and (b) multifunctional biochemical detection biochip system.

### 1.1.3 Hard coatings for glass-molding dies

Glass materials have excellent optical properties, such as a high refractive index and low optical energy absorption in visible light spectrum, and high chemical and heat resistance, and are one of important materials used in the variety of key components and devices. Glass materials are much more suitable than plastic materials applied for high temperature, humid or harsh environments. For those reasons, glass lenses are dominantly used in optoelectronic, chemical, and biomedical devices. Low cost and high performance glass lenses are mostly produced by high precision molding technology. Figure 1.9 shows the photo-pictures of a glass-molding machine and a glass-molding die [23]. Consequently, the protective films are necessary for the glass molding dies to resist elevated temperature and pressure. The protective films of different chemical compositions and processes are developed to satisfy the different glasses operated conditions and to improve and extend the molding die lifetime.

In the glass-molding processes, several steps were needed, including (a) set glass material onto molds, (b) vacuuming inside of the chamber, (c) purging exposure inside of the chamber by nitrogen gas, (d) heat mold and glass materials to specified temperature by infrared lamps, (e) vacuuming inside of the chamber, (f) clamping molds and pressing glass materials, (g) cooling down molds and molded lenses with nitrogen gas, and (h) un-loading molded lenses from molds after cooling to the specified temperature as shown in the Fig. 1.10 [24]. Figure 1.11 shows the application of glass-molding process for fabricating various lenses such as bi-concave lens, bi-convex lens, meniscus lens, insertion lens, prism, f- $\theta$  lens, micro lens array, fiber array, etc [24].



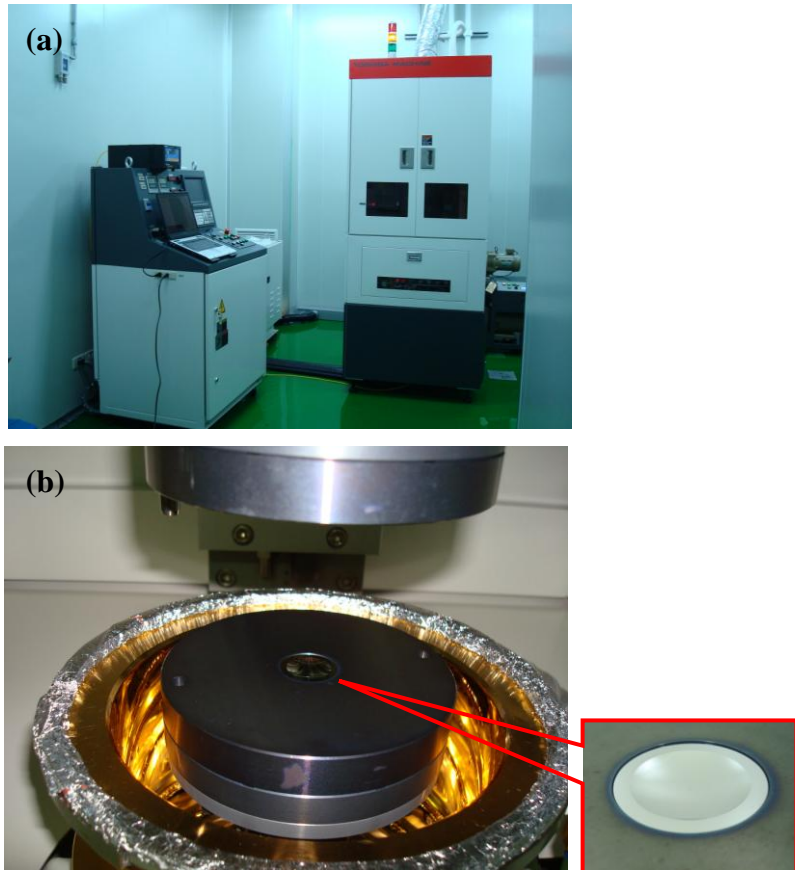


Figure 1.9 Pictures of a glass-molding system [23]. (a) Glass-molding machine of Toshiba-GMP207HV and (b) glass-molding die.

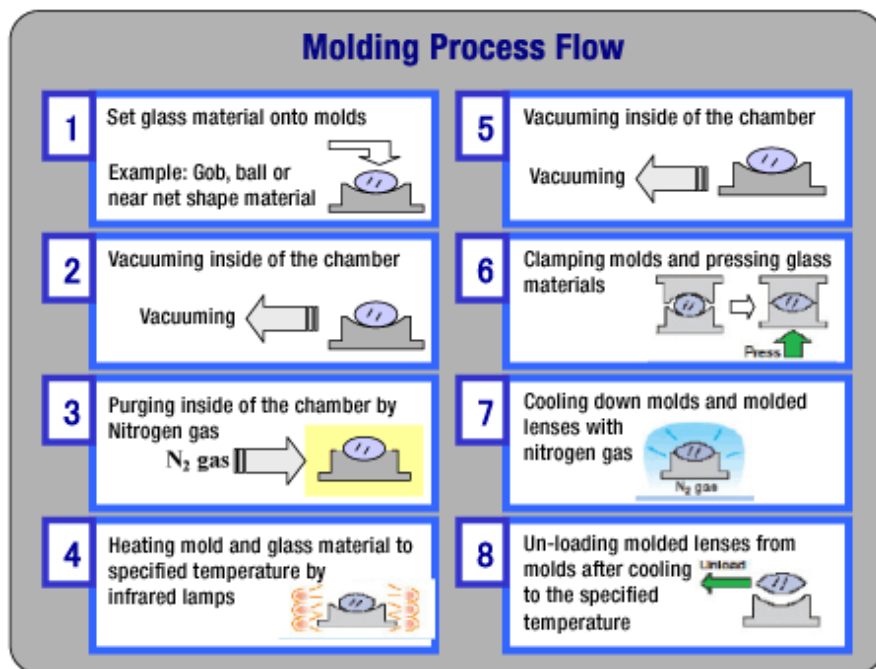


Figure 1.10 Flow diagram for glass-molding processes [24].



Figure 1.11 Application of glass-molding process for fabricating various lenses [24].

## 1.2 Motivation and objectives

The purposes of this dissertation are to develop surface processing technologies including surface scribing, surface texturing, backside writing, and surface treatment of materials and to better understand the interaction between laser beam and materials by the nanosecond pulsed Nd:YAG laser processing system. The electrode isolation using laser direct writing techniques on ITO films deposited on substrates is used in the various mobile phones. The candidates substrates include soda-lime glass, polycarbonate (PC), and cyclic-olefin-copolymer (COC). The operation parameters for the thin films material removal in laser scribing are laser exposure time and scanning speed. The advantages of this method are to reduce the heavy investment of semiconductor lithography process equipment and to decrease the chemical harm to the environment compared with the wet etching process.

To reduce the production costs and increase the processing speeds, current laser micro- or nano-machining processes employ techniques such as laser ablation, laser milling, and laser deposition. These techniques have been effectively used to manufacture components with enhanced wettability properties. A laser-ablated technique has been used to create rough patterns on a silicon substrate to enhance the surface wettability. Moreover, a laser-induced backside writing (LIBW) process and laser-induced plasma assisted ablation (LIPAA) technique on a soda-lime glass substrate via ablation of metal target are to fabricate hydrophobic templates by the nanosecond pulsed Nd:YAG laser and to discuss the droplet

characteristics, such as contact angle, size and shape, can be measured by a surface tension analyzer.

In the glass-molding or in the glass hot embossing process, a preform glass is heated 20 °C to 40 °C above its yield point and pressed in a pumped nitrogen gas atmosphere. The working temperatures are approximately 500 °C for glasses such as P-SK57, N-PK51, L-LAM69, which are usually used in most molding applications with a low transformation temperature ( $T_g$ ). However, the fused silica has a high  $T_g$  point, and must be heated to 1400 °C -1500 °C before pressed. This study aims to find an operation environment of the glass-molding process by laser irradiations and to investigate the interaction between a laser beam and protective coatings under an ambient atmosphere and a temperature of 1500 °C. A commercial finite element analysis (FEA) software was used to simulate the temperature profile of these Ir-based alloy films irradiated by pulsed Nd:YAG laser because the temperature generated by pulsed laser is difficult to monitor by practical measured methods. The pulsed laser treatment technique has many advantages such as fast, energy-saving, and novel excelling over other traditional furnace treatment. In addition, the properties such as surface roughness, morphology, oxidation, microhardness, and reduced modulus are also discussed. Finally, the simulation results and experimental results are compared.

### **1.3 Structure of the dissertation**

The mechanical, optoelectric, and surface characteristics of materials processed by the nanosecond pulsed Nd:YAG laser system are completely discussed in this dissertation. The contents of each chapter are briefly described as follows:

Chapter 1: Introduction. The backgrounds including (a) electrode forming of transparent conductive oxide (TCO) deposited on various substrates for touch panels, (b) wettability of material surfaces, and (c) hard coatings of glass-molding dies, motivation and objectives, and structure of the dissertation are introduced.

Chapter 2: Literatures review. The literatures review of (a) laser scribing of TCO thin films, (b) wetting effects of various textured surfaces, (c) protective coating compositions for glass-molding dies, and (d) laser treatment technology of material surfaces are introduced.

Chapter 3: Laser processing mechanisms and parameters. Laser radiation absorption mechanisms, laser direct writing techniques, laser-induced backside writing techniques, and laser processing parameters are introduced and defined.

Chapter 4: Experimental apparatus and sample preparation. In this dissertation, laser processing experiments for various materials include (a) laser scribing of indium tin oxide (ITO) thin films deposited on various substrates for touch panels, (b) surface wettability of silicon substrates enhanced by laser ablation, (c) hydrophobic templates with rough patterns fabricated by laser micromachining for liquid droplets generation, and (d) characteristics of Ni-Ir and Pt-Ir hard coatings surface treated by pulsed Nd:YAG laser irradiation. The Nd:YAG laser processing setup, the laser processing parameter, the sample preparation, the numerical simulation, the wettability characteristic, the measured method and instrument are illustrated in this chapter.

Chapter 5: Experimental results and discussion. After numerical simulation and laser processing, all the experimental and simulation results of mechanical, optoelectronic, and/or surface characteristics are measured and discussed.

Chapter 6: Conclusions and future work. The conclusions of current studies and suggestions of future studies are summarized in this chapter.

## Chapter 2 Literatures review

### 2.1 Laser scribing of TCO thin films

The conventional manufacturing method of the electrode forming was generally carried out by photolithography and wet chemical etching. A complete-cycle process of the conventional method required several processing steps consisting of photoresist (PR) coating, soft bake, exposure, lithography, hard bake, chemical etching, and PR stripping. Moreover, these high investment equipments and multi-steps increased the production cost and were time-consuming. Simultaneously, the PR coating, acid etching, and PR stripping processes also caused extra environmental pollution. Therefore, several issues to reduce fabricating cost and environmental pollution were proposed recently. Among them, laser ablating techniques were widely adopted in the microelectronic industries including (a) front-end and back-end semiconductor fabrication processes, (b) advanced test and interconnects, (c) flat panel display, (d) micromachining, and (e) others (i.e. solar cell, disk device, and nano-fabrication) [25]. A novel approach, laser direct-writing method, was purposed to reduce the high investment of semiconductor lithography processing equipment and to decrease the chemical harm to the environment.

Some researches discussed the thin film ablation using different laser sources. Venkat and Dunskey [6] proposed the laser patterning of indium tin oxide (ITO) films in panel display manufacturing using different types of laser source: Nd :YVO<sub>4</sub>, Nd :YLF, and Nd :YAG. Additionally, the direct write and mask based process were explained for micromachining applications. Yoo et al. [26] proposed the different combination layers of Al, Ag, and Au deposited on glass or plastic substrates. In the experimental procedure, the pulsed Nd :YAG laser beam with 1064 nm wavelength, 10 Hz the pulse repetition frequency, 6 ns the pulse width, and 8.5 W the maximum average power was performed to the sharp-edged patterns of double-layered films. Figure 2.1 shows the SEM image of surface morphology after laser

patterning different thin-film layers [26].

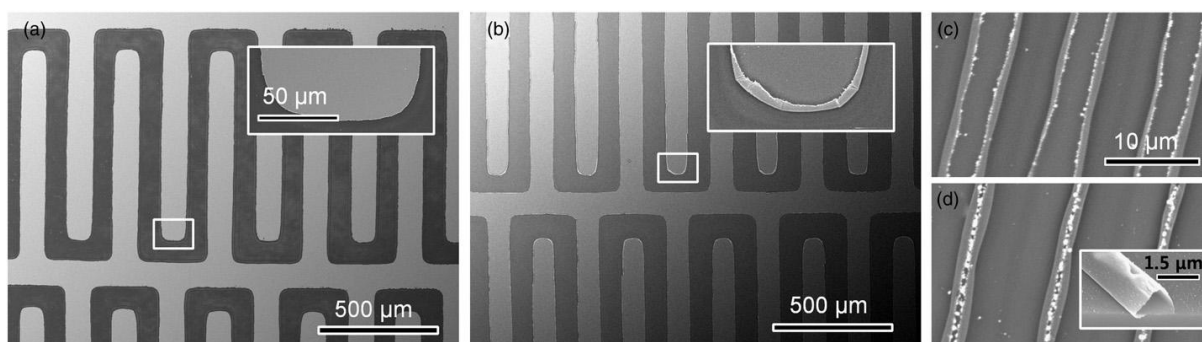


Figure 2.1 SEM images of Ag/Au pattern (a), Al/Ag pattern (b), edge-peeled Al/Ag stripe pattern fabricated by two-beam interference (c), and micro-tubes formed by further increasing the pulse power (d) [26].

Chae et al. [27] presented a high resolution patterning of ITO thin films using an excimer laser scanning projection process. Figure 2.2 shows the schematic illustration of high-resolution ITO patterning process [27]. The amorphous ITO (a-ITO) films were deposited on substrates by sputtering process at room temperature. These films then were crystallized selectively after excimer laser crystallization projection. Finally, the ITO patterns could be obtained by wet etch process for removal of the residual a-ITO films. Solieman [28] conducted a spin coating method to deposit nanoparticles on glass substrates. The patterning was cured by a laser processing system, and the emitted light wavelengths could be modulated ranging from 200 nm to 600 nm. Moreover, this system could adjust different feed speeds of moving stages ranging from 0.01- 0.35 mm/s for controlling the energy density and the film temperature. Shin et al. [29] fabricated high resolution patterning of ITO thin films for electronic devices by using a pulsed Nd :YAG laser. The Nd :YAG laser patterning technique was used to ablate the ITO films that could generate the circuit on the conductive films and reduce the traditional processing steps. Figure 2.3 shows the optical profiler images

of patterned films [29].

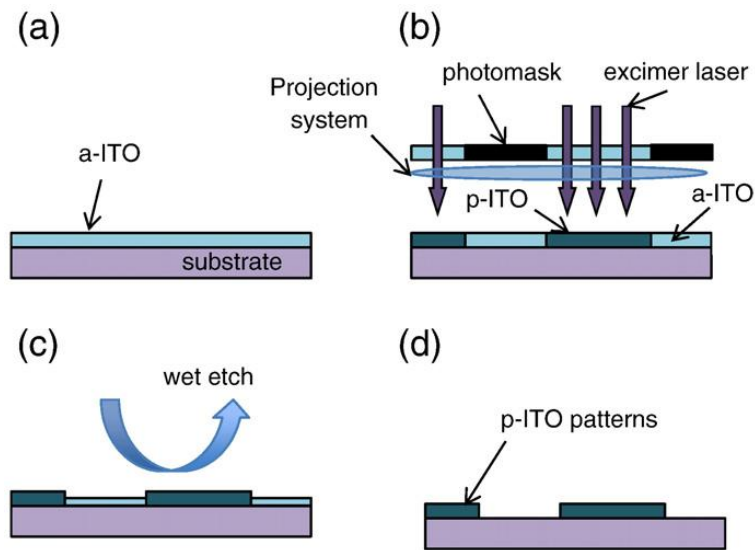


Figure 2.2 Schematic illustration of high-resolution ITO patterning process [27].

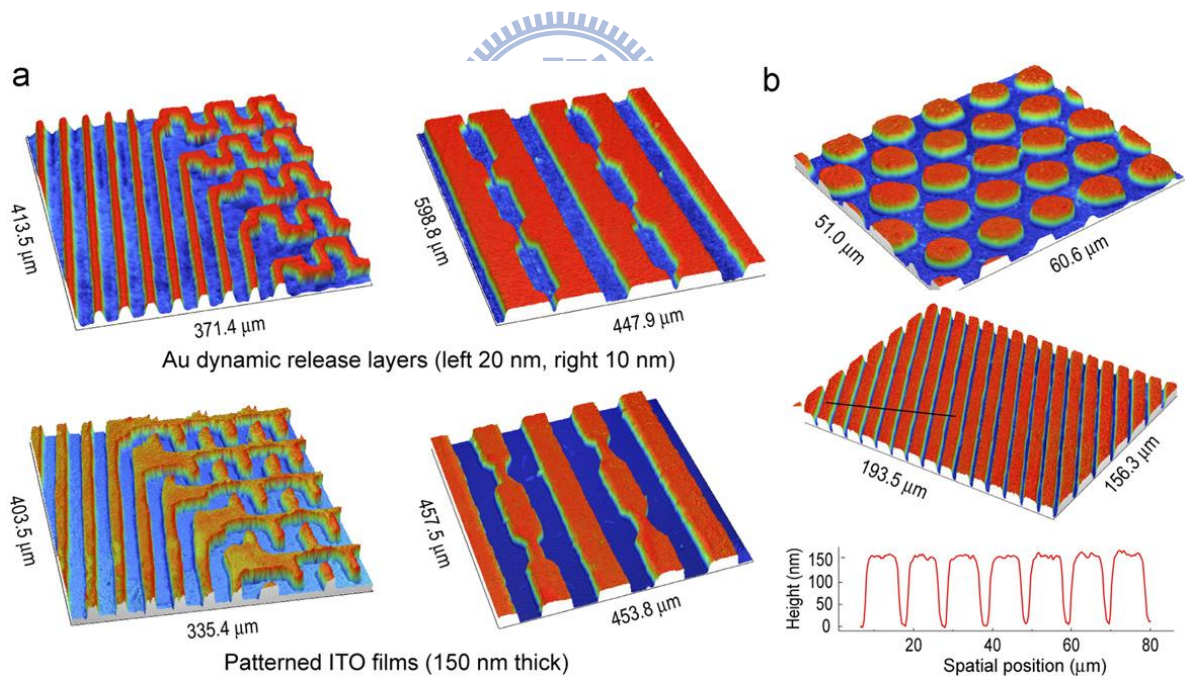


Figure 2.3 Optical profiler images of patterned Au (top) and ITO (bottom) films (a) and ITO patterns created using holographically patterned Al layers (b) [29].

Yavas and Takai [30,31] used the Q-switch Nd:YLF laser and flash lamp-pumped Nd:YAG laser to ablate ITO thin films, and investigated the relationship between different

absorption of ITO thin films and the observed morphology differences. Moreover, the temperature model was used to confirm that ITO films were removed by the evaporative mechanism. Lunney et al. [32] used the KrF excimer laser to ablate the fluorine-doped tin oxide and indium tin oxide transparent conductive thin films. The 50  $\mu\text{m}$  wide conducting channel was ablated and measured by a scanning electron microscope. Molpeceres et al. [33] used three types of laser source, including KrF excimer laser, Nd:YAG laser, and diode pumped solid state (DPSS) laser, for patterning the amorphous silicon (a-Si) and ITO thin films.

Park et al. [34] used an ultrafast laser with wavelength of 810 nm and pulse width of 150 fs to ablate the ITO thin film coated on the glass substrate. Both laser fluence and number of pulses affect the ablation region depth. Figure 2.4 shows the ablation depths and widths at different fluences measured by increasing the number of laser pulses [34]. With increasing the number of pulses at the laser fluence well above the ablation threshold, the ablated depth increases and then converges to a constant value of about 200 nm. The ablation threshold of the ITO film conducted by the ultrafast laser was found to be  $0.07 \text{ J/cm}^2$  that is much lower than that of the glass substrate (about  $1.2\text{-}1.6 \text{ J/cm}^2$ ), which leads to a selective ablation of ITO films without damage on glass substrate.

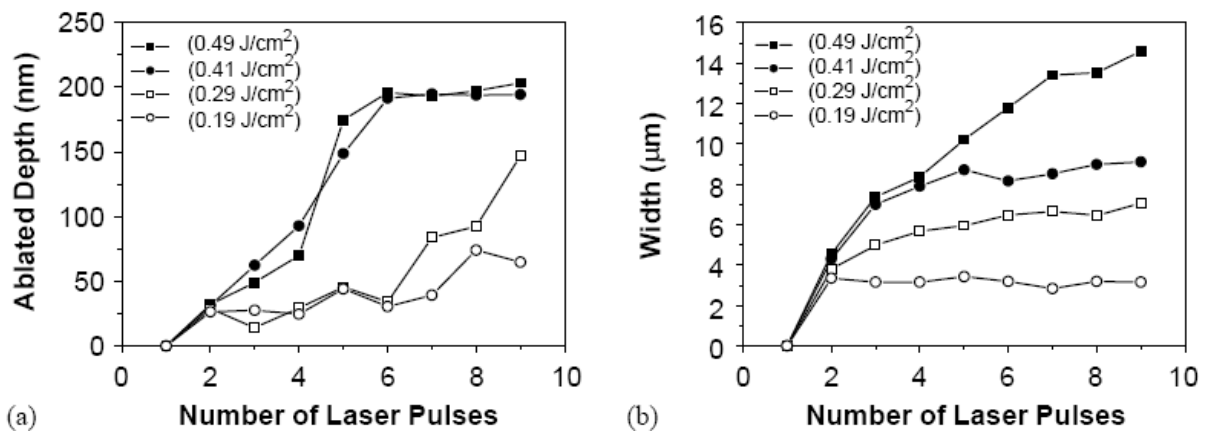
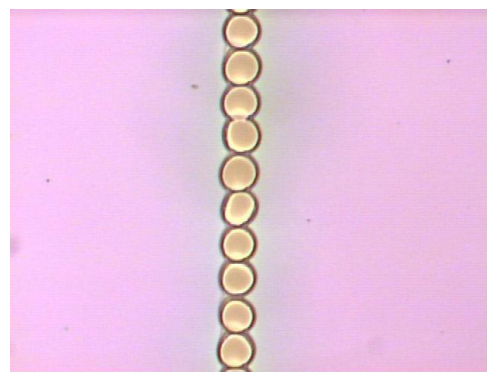


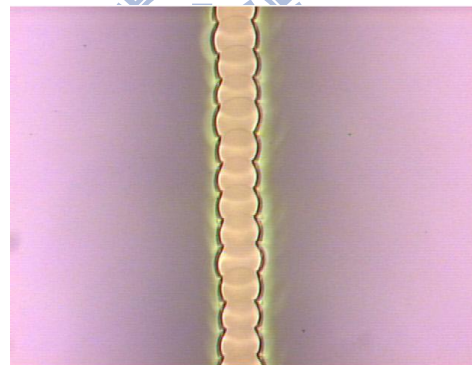
Figure 2.4 Ablation depths and widths at different fluences measured by increasing the number of laser pulses [34].



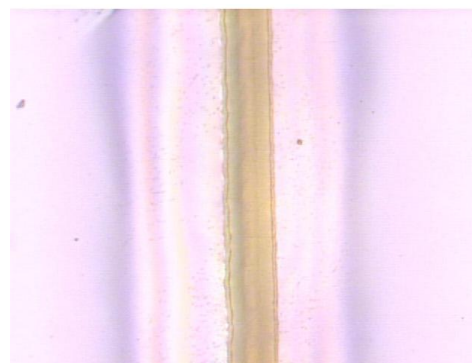
Chen et al. [35] developed a third harmonic Nd:YAG laser system to direct writing patterns on ITO films and discussed the effect of the different feeding speeds and pulse repetition frequencies on the patterned line overlapping rate. Figure 2.5 shows the UV laser direct writing of ITO thin films with different feed rates [35]. By increasing the laser scanning speed and pulse repetition frequency, the patterned line width decreased.



**(a) OL rate = 0%**



**(b) OL rate = 34%**



**(c) OL rate = 75%**

Figure 2.5 UV laser direct writing of ITO thin films with different feed rates [35].

Chen et al. [36] also used the laser beam shape technique to obtain top-hat intensity distribution laser beam to perform line scribing and to perform electrode patterning on ITO thin films deposited on glass and plastic substrates. Figure 2.6 shows the schematic diagram of laser beam transmittance [36]. The obtained morphology of the complex patterning electrode was uniform, smooth, and free from damage in substrates after the laser patterning was performed. Qiao et al. [37] used a Nd:YAG laser with wavelength of 1064 nm and pulse duration of 40 ns, and also used a Nd:YVO<sub>4</sub> laser with wavelength of 355 nm, pulse duration of 40 ns, and a Gaussian-to-top-hat convert to scribe in-house textured gallium-doped zinc oxide (GZO) thin films coated on glass substrates for amorphous silicon photovoltaic (PV) applications. The smooth edges and flat bottoms of the scribed lines were achieved by an ultraviolet (UV) laser system.

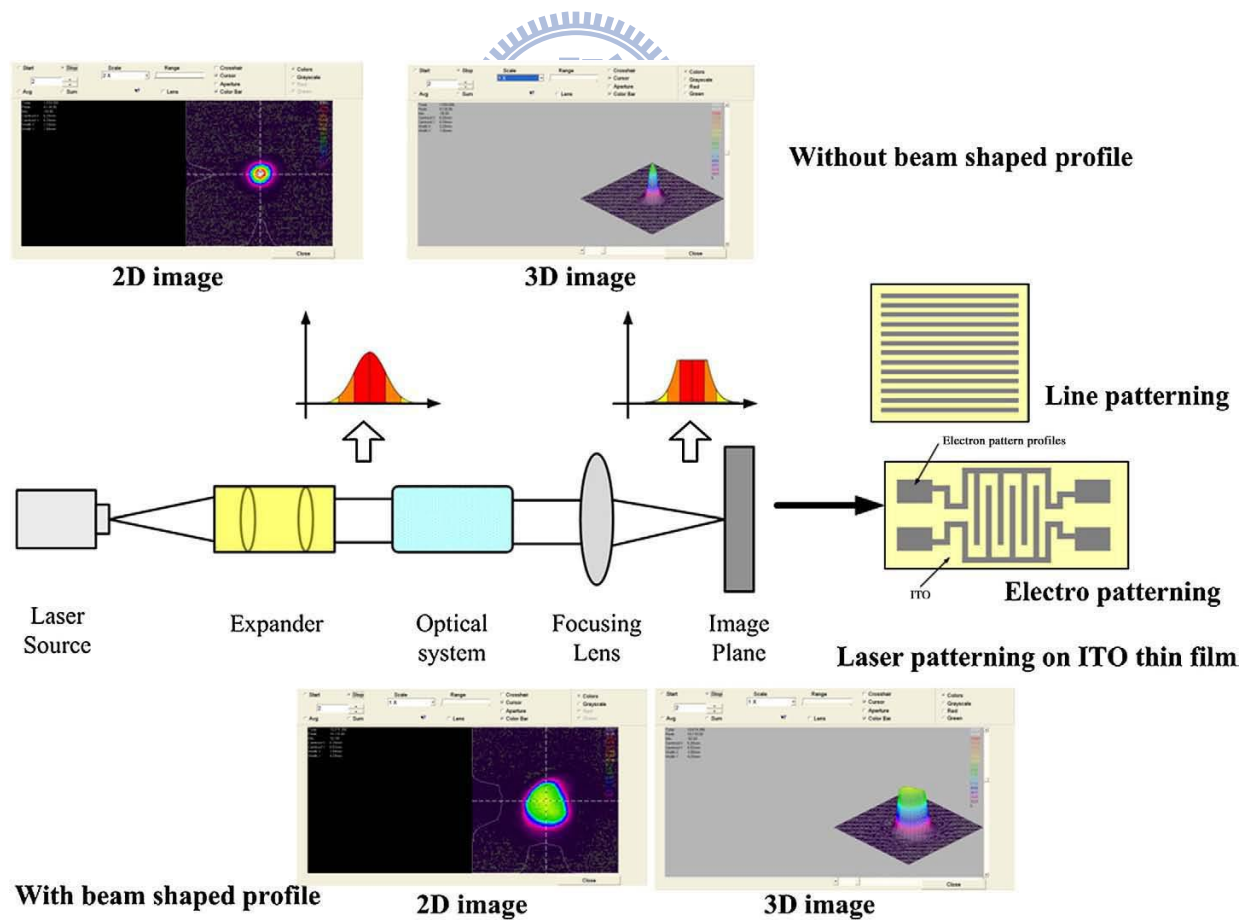


Figure 2.6 Schematic diagram of laser beam transmittance [36].

Kim et al. [38] adopted a pulsed Nd:YAG laser with TEM<sub>00</sub> mode and ablated the FTO thin films coated on soda-lime glass substrates. The experimental results showed that a pin-hole size of 1.6 mm diameter had the perfect TEM<sub>00</sub> mode and the parameters of the best ablation trace included the overlapping rate of 62%, the feeding speed of 6.08 mm/s, the pulse repetition frequency of 10 Hz, and the charging voltage of 1000 V. Figure 2.7 shows the SEM images of the surface morphology ablated by the Nd:YAG laser at different overlapping rates: (a) 0%, (b) 25%, and (c) 62% [38]. Hass et al. [39] used pulsed lasers with wavelength of 1064 nm and 532 nm for patterning of ZnO/Ag back contact on the thin-film silicon modules. For the microcrystalline silicon, a good patterning quality could be obtained by a green laser or a NIR-laser with short pulse duration.

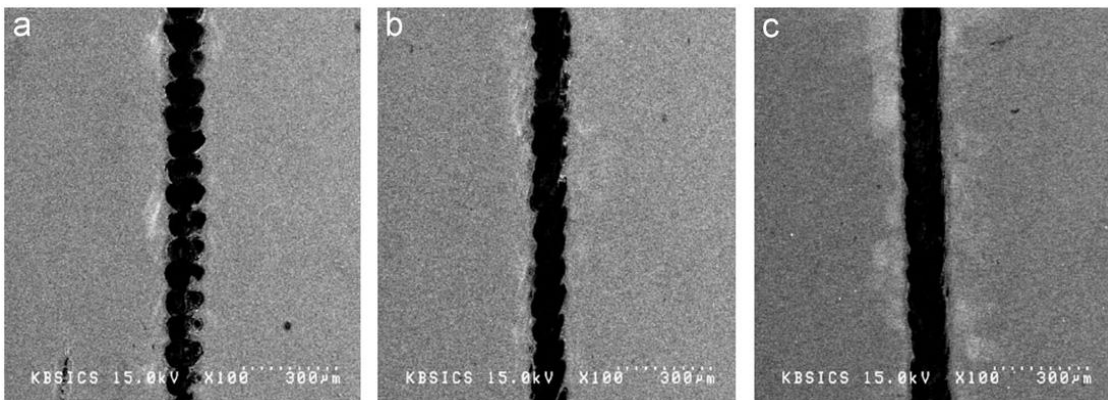


Figure 2.7 SEM images of the surface morphology of ablated by the Nd:YAG laser at different overlapping rate: (a) 0%, (b) 25%, and (c) 62% [38].

## 2.2 Wetting effects of various textured surfaces

With improvements in material processing, orderly microstructure rough surfaces are usually created by advanced surface processing techniques such as laser [40-43], dry-etching or wet-etching [44], diamond dicing [18], and lithography [45]. In addition, the coating technology is used to obtain superhydrophobic surfaces by creating nanostructures on the microstructure of processed substrates. The flat silicon surfaces processed using dicing

machines by Yoshimitsu et al. [18] are orderly one-dimensional microgroove structures and pillarlike microgroove structures. The surface is then coated with a layer of fluoroalkylsilane (FAS), and water droplets are then used to compare the hydrophobicity and sliding behavior. The results showed that the difference in surface feature and surface roughness will affect the hydrophobicity and sliding angle of the surface. Figure 2.8 shows the pictures of 1 mg water droplets on prepared pillar structures, corresponding different water contact angles, roughness factors, and pillar heights machined by a dicing machine [18].

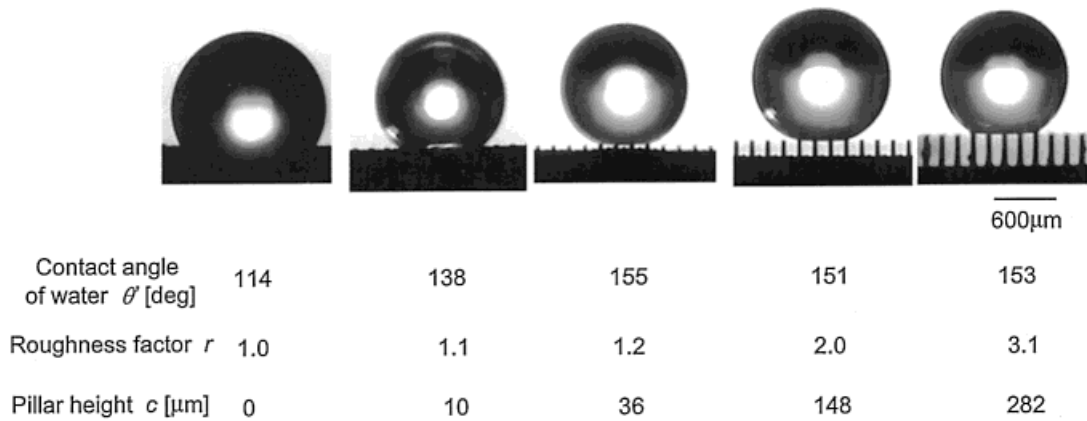


Figure 2.8 Pictures of 1 mg water droplets on prepared pillar structures [18].

Kannan and Sivakumar [40] utilized the diamond paste-polishing machine and laser processing machine to individually manufacture stainless steel materials. They obtained a  $0.013 \mu\text{m}$  smooth surface roughness and a single direction groove surface. They also studied the impact process of water droplets on the hydrophobic surface as shown in Fig. 2.9 [40]. The geometry of the groove structure determines the liquid spreading after impacting the surface. The liquid spreads along the direction of the groove. Due to the solid pillars of the groove surface, the vertical spreading of the liquid in the groove is comparatively slower. Lee et al. [46] utilized different surface roughness to design and manufacture a switchable membrane device. This device attaches a thin polydimethylsiloxane (PDMS) membrane bounded the top of the rough PDMS base board. The thickness of the PDMS membrane is less

than 2  $\mu\text{m}$ . This membrane device can switch from moderate hydrophobicity to superhydrophobicity by deflecting the membrane with a pneumatic method after testing.

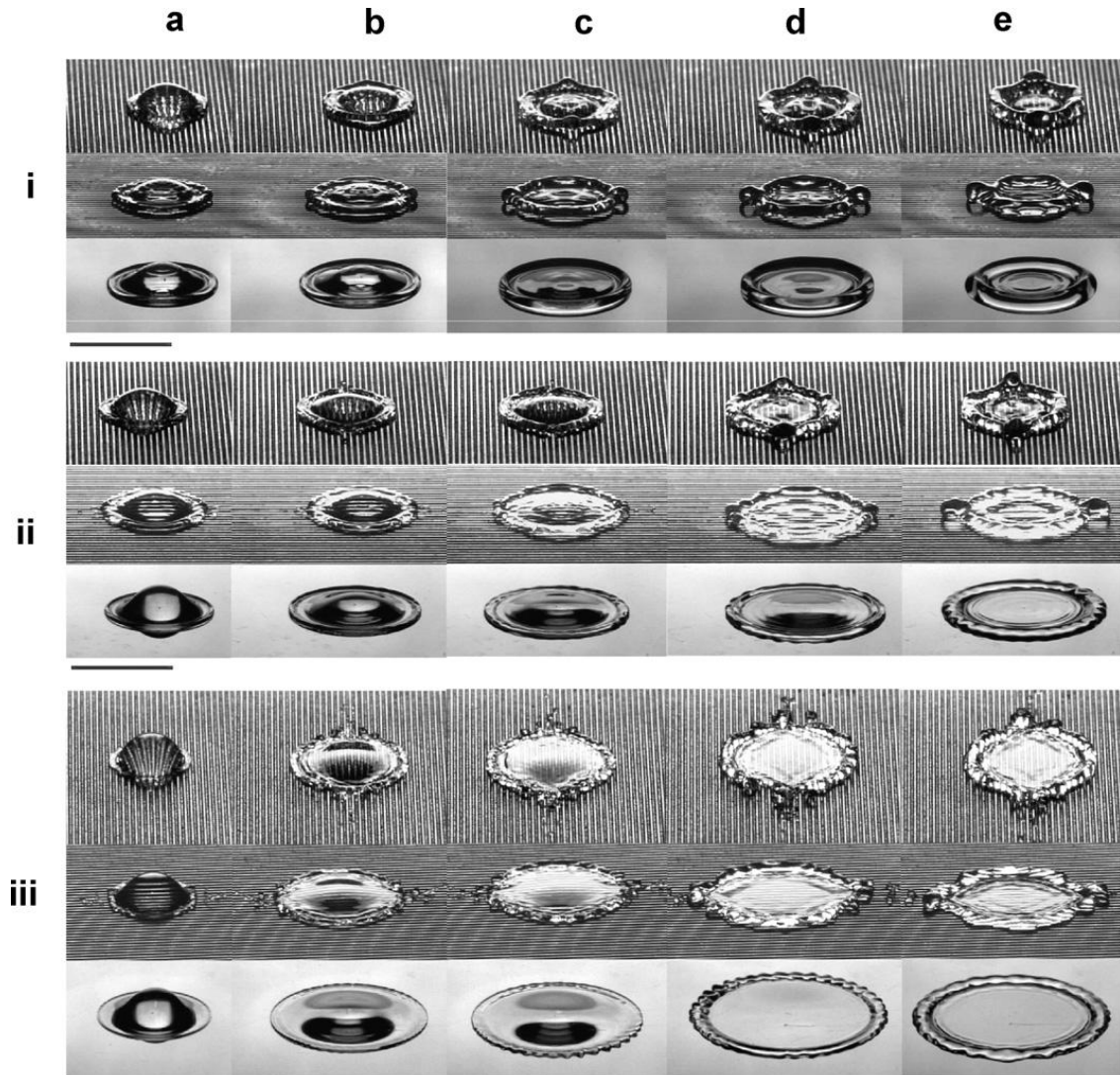


Figure 2.9 Spreading-process images of water droplets with different impact conditions on the hydrophobic grooved surface [40].

Chen et al. [47] adopted four types of hydrophobic materials including AZ6112, Teflon, Parylene C, and plasma polymerization fluorocarbon film (PPFC) to fabricate the hydrophobic textured surfaces with microstructures by using the standard lithography process. The machined templates of the chain configuration and the concentric circular configuration

were used to develop a droplet manipulating device as shown in Fig. 2.10 [47]. Because of these templates without external power consumption and without side effect problems, the proposed device can be applied in the droplet manipulation of microfluidic systems and in thermal or electrical applications. Figure 2.11 shows the dynamic motion of a droplet on a separated route [47].

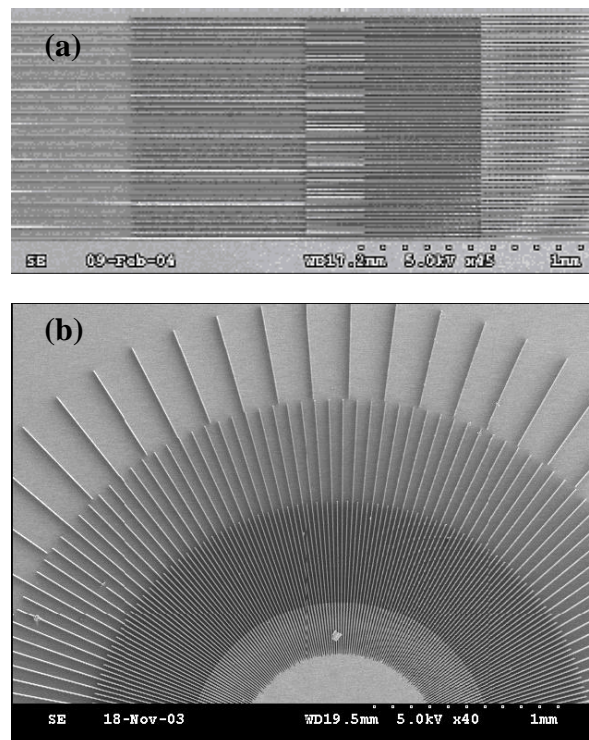


Figure 2.10 SEM photos of the textured surfaces fabricated by using the standard lithography process, (a) chain-configuration and (b) concentric circular configuration [47].

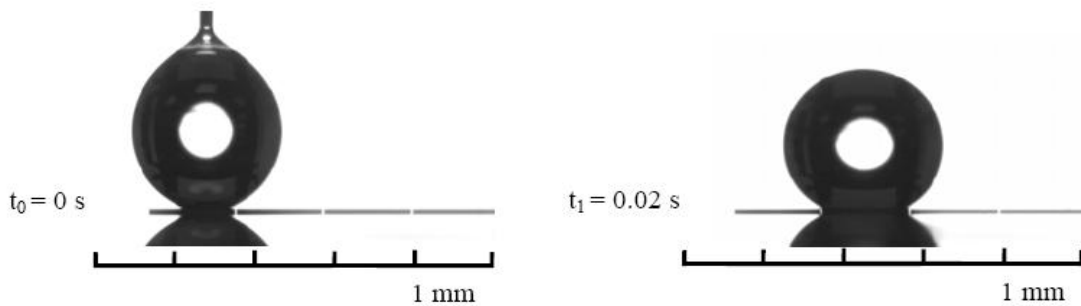


Figure 2.11 Dynamic motion of a droplet on a separated route [47].

Kim et al. [48] developed hexagonally arranged closed-packed concave nanotextures of master surface of nanoporous alumina to imprint on aluminum films and gold films by thermal evaporation and on polystyrene films by spin coating. The nanotextured templates were used to calculate with measured water contact angles that decreased with depending strongly on the materials and shapes of duplicating nanotextures. Figure 2.12 shows the topology, the chemical reactivity, and the wettability of various nanopatterned aluminum films [48].

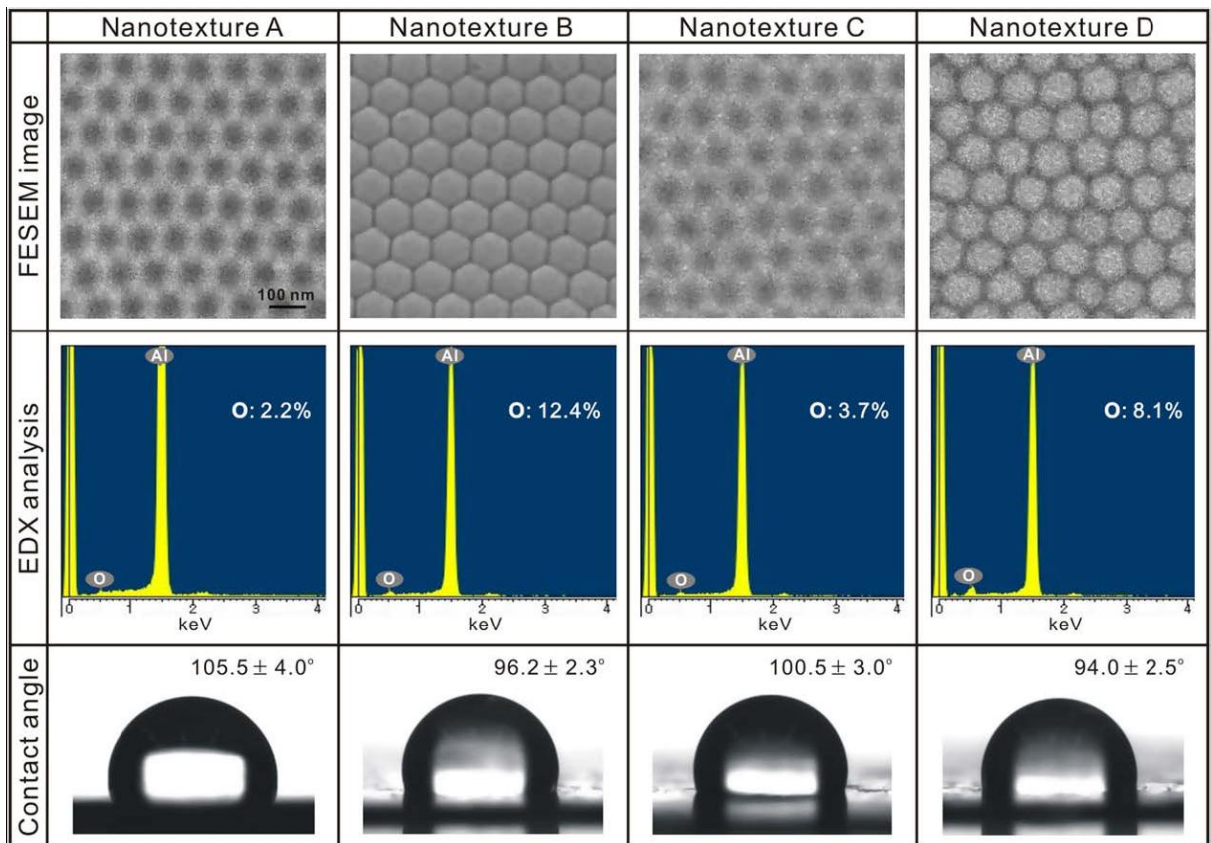


Figure 2.12 FESEM images (top), EDX analysis spectra (middle), and water contact angles (bottom) of various nanopatterned aluminum films [48].

Dahotre et al. [49] demonstrated a laser-based surface modification technology to improve the wettability of the Ti-6Al-4V alloys to physiological fluids. The groove and pillar patterns obtained using an interference patterning technology for increasing the apparent

contact angle. The roughness factors of these patterns were measured and plotted as a function of laser fluence, as shown in Fig. 2.13(a) [49]. The measured results could be observed that the roughness factor increased slightly with increasing laser fluence for both patterns. Furthermore, the critical wetting angles of these patterns were measured and plotted as a function of laser fluence, as shown in Fig. 2.13(b) [49]. The measured results could be observed that the critical wetting angle increased with increasing laser fluence for both patterns. The roughness factor of pillar patterns was higher than that of groove patterns; therefore, the critical wetting angle of pillar patterns was larger than that of groove patterns.

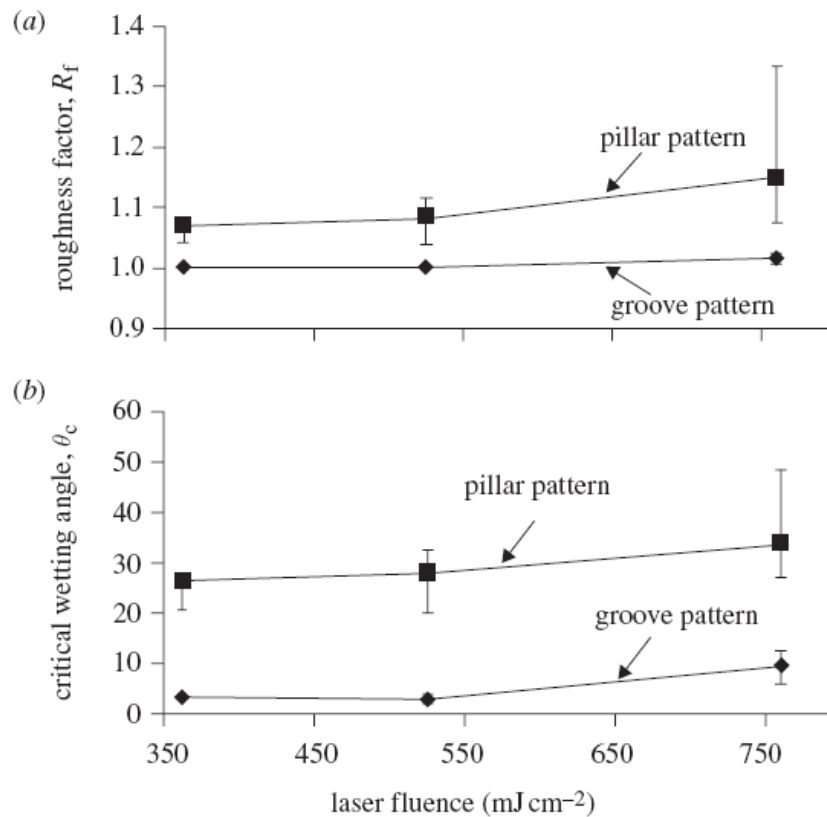


Figure 2.13 Variation in roughness factor (a) and critical wetting angle with laser fluence for groove and pillar patterns (b) [49].

Stojanovic et al. [50] demonstrated a developed coating composed of superhydrophobic silicon nanofilaments combined with laser-ablated lines to investigate the surface wettability



on machined templates. A near-ultraviolet Nd:YAG laser with a wavelength of 355 nm and a pulse repetition frequency of 10 kHz were used to perform the nanofilament. Figure 2.14 shows the system of two immiscible liquids with suppressed evaporation and accurate positioning of the aqueous liquid [50]. This approach can be used for open channel microfluidics and microarray analysis due to its simplicity, the low cost, and the chemical and environmental stability. Oliveira et al. [51] used a KrF laser to ablate polyimide surfaces that had different microstructures as a function of the laser fluence ranging from 35 J/cm<sup>2</sup> to 155 J/cm<sup>2</sup>. The surface morphology and static contact angle of these laser-ablated surfaces were measured and discussed. The measured results revealed that the apparent contact angle of the laser-ablated surfaces increased with increasing the laser fluence. Moreover, the apparent contact angle of the laser-ablated surfaces could reach values as high as 162° compared with 75° for the un-ablated polyimide surfaces.

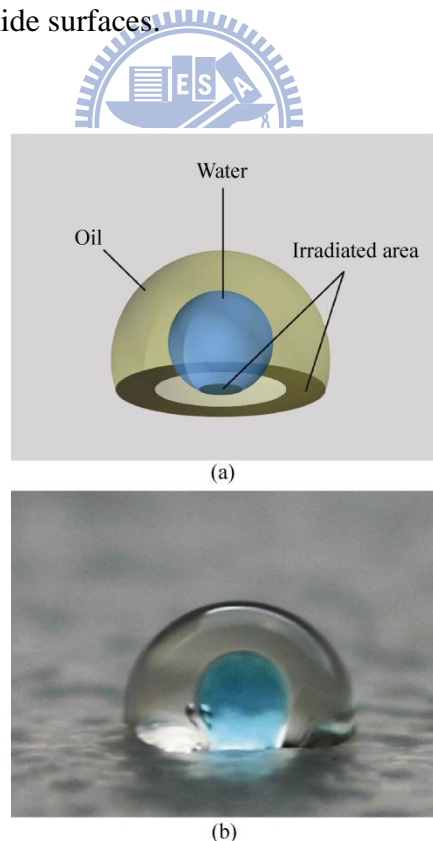


Figure 2.14 System of two immiscible liquids with suppressed evaporation and accurate positioning of the aqueous liquid: (a) schematic diagram of laser-ablated patterns and (b) picture of a water droplet contained within hexadecane [50].

Luo et al. [52] used an excimer laser with a wavelength of 248 nm to etch the steel surface to form different micro-patterns. The patterned surface became more hydrophobic after depositing amorphous carbon (a-C) thin films using a magnetron sputtering technology. The contact angle of a-C coating on laser patterned surface was approximately large than  $10^\circ$  to  $20^\circ$  that of on the laser patterned surface. Bekesi et al. [53] used a short-pulse UV laser combined with a fused silica-based diffractive optical element (DOE) to rapidly fabricate a steel mold. This DOE was applied to distribute the laser energy into a  $25 \times 25$  dot matrix and as a transmission mask for laser ablation of steel mold. The laser-ablated mold was used to replicate superhydrophobic surfaces on polypropylene by using variothermal injection molding processes. The measured results showed that these contact angles of superhydrophobic surfaces were more than  $160^\circ$ . Noh et al. [54] conducted a study of hierarchically micro- and nano-structured mold surfaces using laser ablation for mass production of superhydrophobic surfaces. The picoseconds laser source used in this experiment was a Nd:YVO<sub>4</sub> laser with a wavelength of 1064 nm, a pulse width of 12 ps, and maximum pulse repetition frequency of 640 kHz. These microstructures on the mold surface were replicated onto polydimethylsiloxane (PDMS) using a polymer casting method to fabricate low-cost superhydrophobic surfaces. Figure 2.15 shows the micro- and nano-structures of a nature lotus leaf and a laser-ablated mold [54]. The measured results showed that the maximum contact angle of the water on the smooth PDMS surface and on the replicated PDMS surface were  $91^\circ \pm 1.5^\circ$  and  $157^\circ \pm 3^\circ$ , respectively. Tang et al. [55] proposed superhydrophobic surfaces fabricated by the femtosecond laser micromachining and chemical vapor deposition to constitute micro- and nano-structures formed for carbon nanotube (CNT) cluster. Plasma treatment was subsequently executed on growth of CNT clusters to enhance the surface hydrophobicity. The wetting property of CNT surface with plasma treatment was improved from hydrophilicity to superhydrophobicity, and the contact angle was  $161^\circ$ . This manufacturing process can be applied to produce the self-cleaning glass for solar panels,

vehicles, home windows, road lamps, and so on.

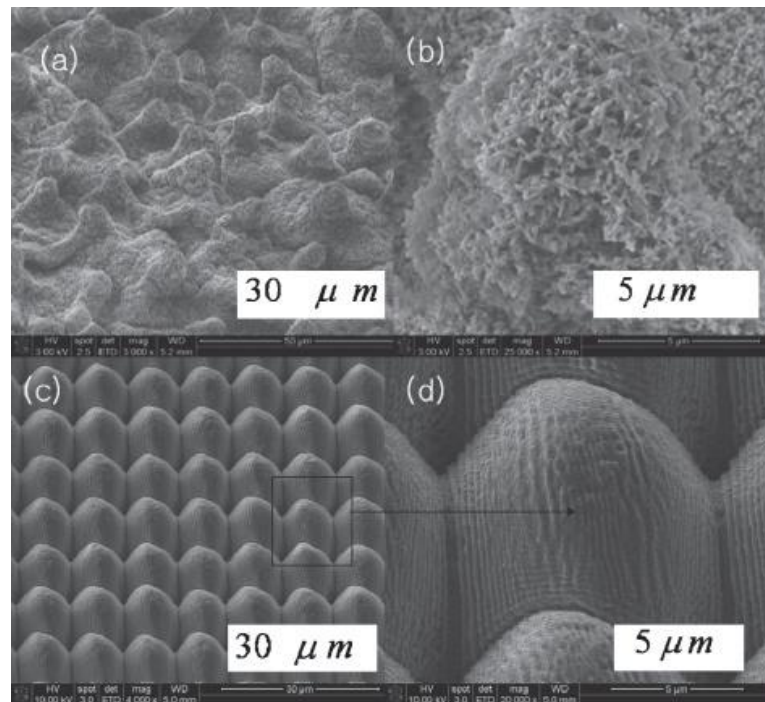


Figure 2.15 SEM images of a natural lotus leaf (a, b) and SEM images of laser-ablated micro- and nano-structures and ripple formation (d, e) [54].

### 2.3 Protective coating compositions for glass-molding dies

Tungsten carbide (WC) was used as the mold material in glass-molding process. This material is very hard and brittle but offers good performance in glass-molding dies. Pt-Ir, CrN, CrWN, and Mo-Ru thin films are reported to coat mold surface and to increase the lifetime of molds. Tseng et al. [56] discussed mechanical properties of Pt-Ir and Ni-Ir binary alloys for glass-molding dies coating. Figure 2.16 is SEM pictures and shows a series of cross sectional structures of the Ir-based deposits on the silicon wafer with Cr as buffer layer [56]. With increasing Pt and Ni doping contents in Ir-based coatings, the microhardness of both coatings decreased significantly and the values of reduced modulus of Pt-Ir alloys are larger than that of Ni-Ir alloys. After the oxidation testing of these Ir-based coatings exposed at 700°C by a glass-molding machine, the oxygen concentration in Pt-Ir coatings does not obviously change

with increasing Pt contents. However, the oxygen concentration of Ni-Ir coatings shows large variations even though the glass molding operation was conducted under the N<sub>2</sub> atmosphere.

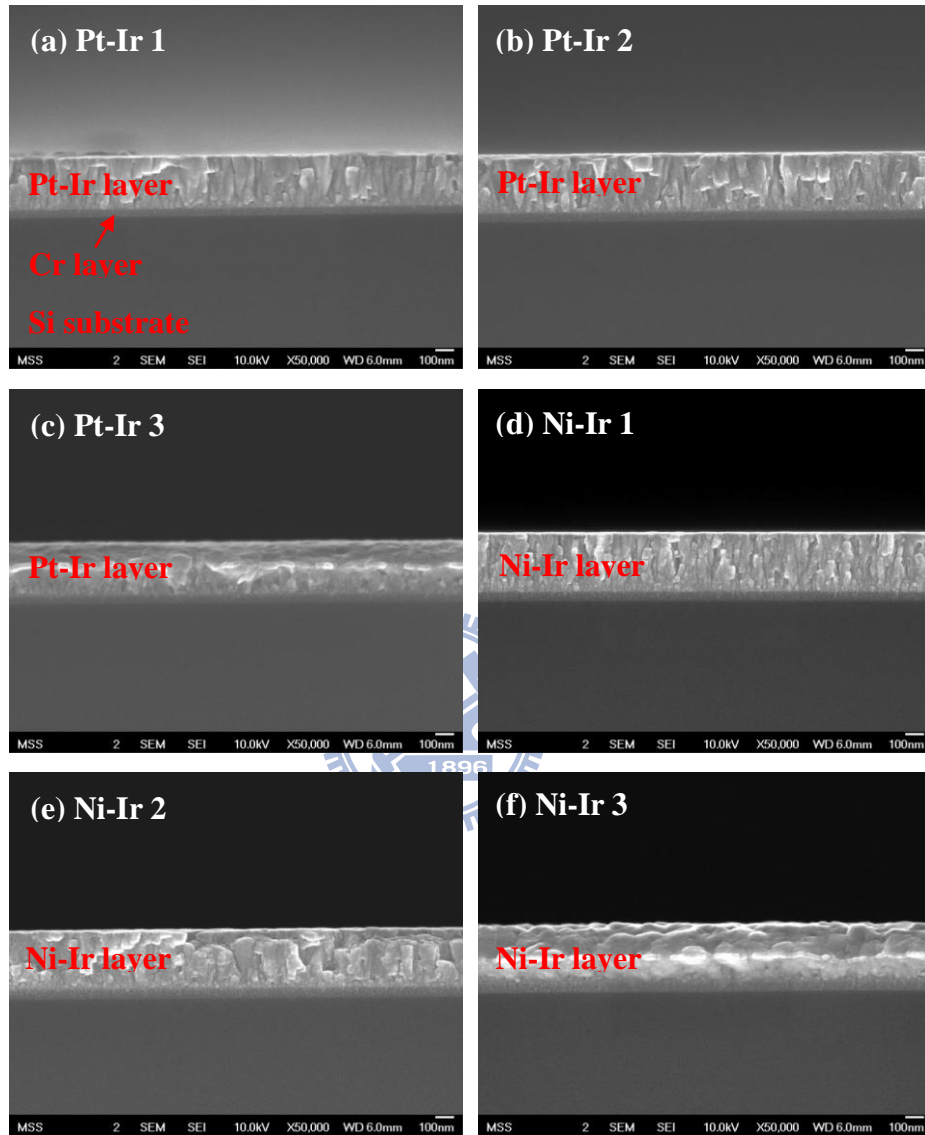


Figure 2.16 Cross-sectional micrographs of Cr, Pt-Ir and Ni-Ir coatings [56]. (a) Pt-Ir 1 (27.67 at.% Pt), (b) Pt-Ir 2 (55.25 at.% Pt), (c) Pt-Ir 3 (79.42 at.% Pt), (d) Ni-Ir 1 (26.10 at.% Ni), (e) Ni-Ir 2 (51.44 at.% Ni), (f) Ni-Ir 3 (73.45 at.% Ni).

Lin et al. [57] proposed CrWN coatings with the tungsten contents of 0–23.4 at.% coated on WC substrates by ion beam assisted deposition. Figure 2.17 shows the

cross-sectional micrographs of chromium nitride based coatings [57]. With 4.4 at.%, 7.1 at.%, 13.1 at.%, and 19.7 at.% tungsten doping contents in CrN coatings, the smooth surfaces were obtained and surface roughness Ra less than 2 nm. After oxidation test at 750°C in air atmosphere, the Cr<sub>2</sub>O<sub>3</sub> precipitates were formed and resulted in the large roughness of more than 40 nm on the CrN and CrWN coatings surface. However, the CrWN coatings with 4.4 at.% to 16.7 at.% tungsten contents revealed smooth surface and improved hardness that can be applied in glass-molding die coatings.

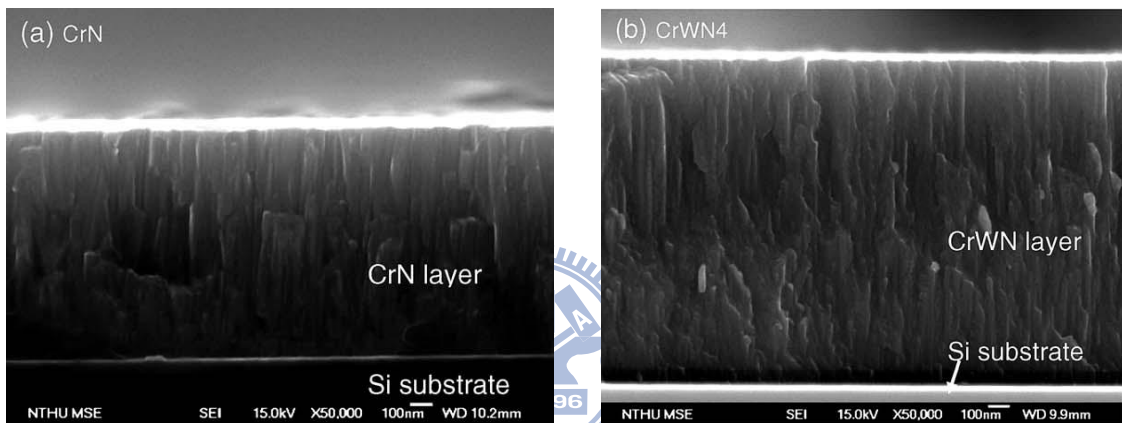


Figure 2.17 Cross-sectional micrographs of chromium nitride based coatings [57]. (a) CrN and (b) CrWN4 (16.7 at.% W).

The Mo-Ru binary alloys with Cr and Ti twin buffer layers deposited on WC substrates as the protective coatings was investigated [58,59]. Figure 2.18 shows the cross-sectional TEM images of (a) Mo<sub>56.7</sub>Ru<sub>43.3</sub>/Cr/Ti(O)/WC deposit and (b) detailed structure of the oxide scale, the transition zone and the columnar grains [59]. With the higher Ru doping contents in Mo-based coatings, the results show that the Mo-Ru alloys have better oxidation resistance but also have a higher surface roughness. Moreover, Wei and Shieh [60] proposed the TaN binary compounds and Ta<sub>1-x</sub>W<sub>x</sub>N<sub>y</sub> ternary compounds deposited on the WC dies and silicon wafers by ion beam sputtering. The Ta<sub>1-x</sub>W<sub>x</sub>N<sub>y</sub> films reveal better high temperature performance than the TaN films for glass-molding die coatings such as high melting point,

high hardness, and chemical resistance. These films are anti-adhesive and have excellent chemical stability and good coating stability under working environment. Moreover, laser surface treatment can improve the toughness and durability of film materials to further enhance the performance of the mold surface.

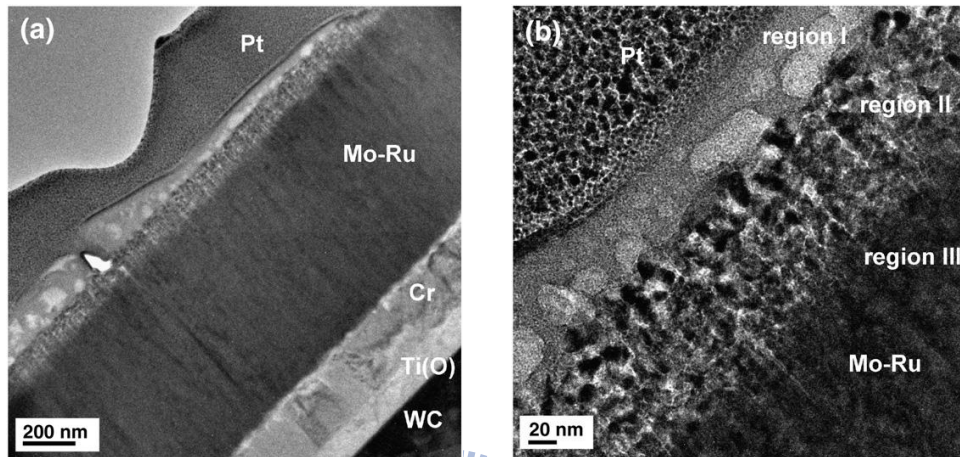


Figure 2.18 Cross-sectional TEM images of (a) Mo<sub>56.7</sub>Ru<sub>43.3</sub>/Cr/Ti(O)/WC deposit and (b) detailed structure of the oxide scale, the transition zone, and the columnar grains [59].

## 2.4 Laser treatment technology of material surfaces

In 1941, Rosenthal [61] proposed a mathematic model to thermally evaluate the transient temperature field of working pieces for point, line, and surface heating laser sources. Kang et al. [62] applied a finite element program ABAQUS to analyze the heat transfer and residual distortion for laser welding LD (laser diode) pump on EDFA (erbium doped fiber amplifier). Figure 2.19 shows the temperature distributions at welding procedure of laser diode pump on erbium doped fiber amplifier [62]. In the Nd:YAG laser welding process, distortion occurs at the ferrule and saddle during the heating and cooling processes of welding. Gordon et al. [63] provided a simulation tool for a laser manufacturing process. He discussed the relationship between the pulse energy, the etch rate, the pulse frequency and the preheating temperature of the substrates. Laser processing is another surface heat treatment that usually provides the

advantages of no contact between the tools and work specimens, high temperature, lack of tool wear, high speed, and few thermal effects [64].

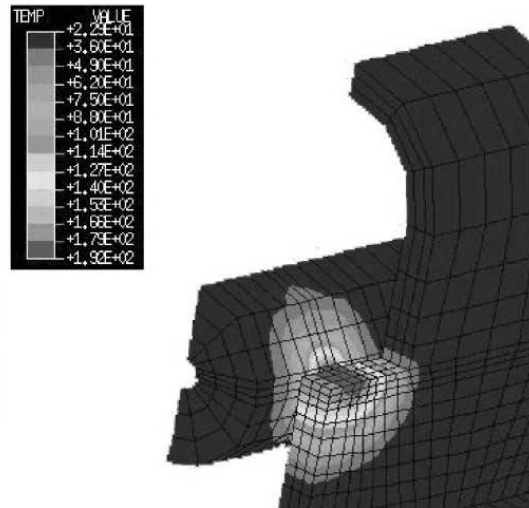


Figure 2.19 Temperature distributions at welding procedure of laser diode pump on erbium doped fiber amplifier [62].

Liu et al. [65] discussed a pulse laser-textured method that uses a Co-based WC-TiC sintered carbide coating. They also investigated the resulting microstructure, roughness, hardness, and wear resistant properties of coatings. Figure 2.20 shows the cross-sectional views of the alloyed layer textured with different laser power [65]. These measured results reveal that the micrographs have three distinct regions including the laser melting zone (LMZ), the heat affected zone (HAZ), and the non-affected zone (NAZ) existed in the interface between the substrate and the coating. Textured surfaces have many advantages and the most important one is to improve mechanical performance, such as surface hardness [66], tribological behaviour [67], and lubricating of friction [68,69]. Wan [70] proposed a novel laser coating and texturing technique to improve surface topographies and friction behaviour. Tseng [43] reported a surface-texturing technique to create rough patterns on a silicon substrate and to investigate the wettability on laser-textured surface.

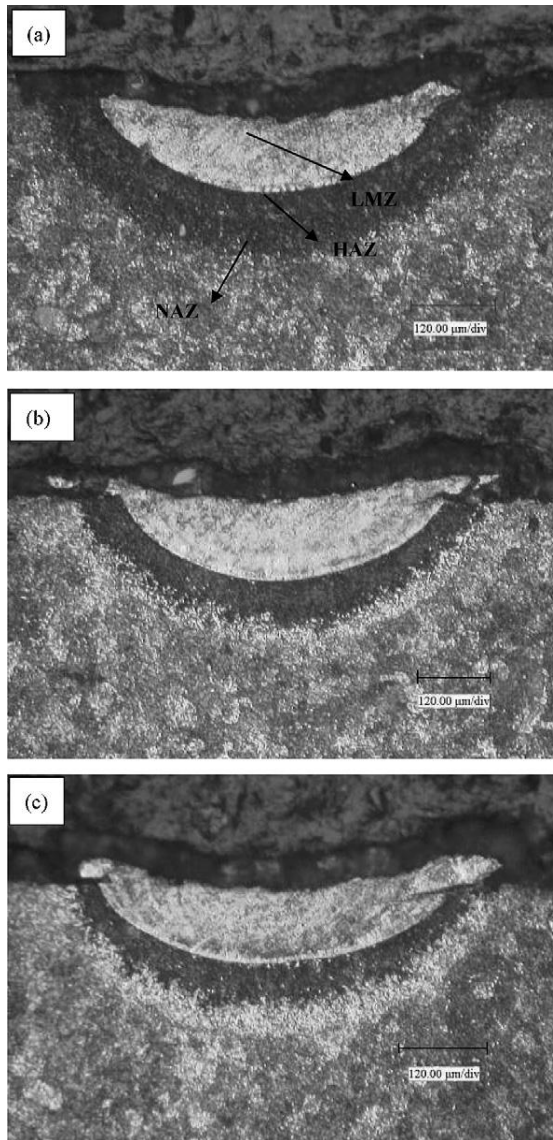


Figure 2.20 Cross-sectional views of the alloyed layer textured with different laser power: (a) P = 500 W, (b) P = 700 W, (c) P = 900 W [65].



## Chapter 3 Laser processing mechanisms and parameters

### 3.1 Laser processing mechanisms

#### 3.1.1 Laser radiation absorption mechanisms

Laser intensity can be adjusted to raise the temperature by increasing the laser exposure time (pulse duration), pulse repetition frequency, laser fluence (energy density), or power density (intensity). Optical and thermal characteristics of the workpiece are important factors to affect the material machining efficiency after the laser radiations. Figure 3.1 shows the schematic diagram of behaviors of reflectance, transmittance and absorbance as an incident light passes through a material with thickness  $l$ . According to the Beer-Lambert's law [71], the intensity of light  $I$  transmitted from a material can be obtained by following equation.

$$I(l) = I_0 e^{-\alpha l} \quad (3.1)$$

where  $I_0$  and  $\alpha$  are the intensity of the incident light and light absorption coefficient for that specific material, respectively, and  $l$  is the light travel distance through the material. According to the electromagnetic wave theory, the light absorption coefficient of the material is given by:

$$\alpha = \frac{4\pi k}{\lambda} \quad (3.2)$$

where  $k$  and  $\lambda$  are the extinction coefficient and wavelength of light, respectively.

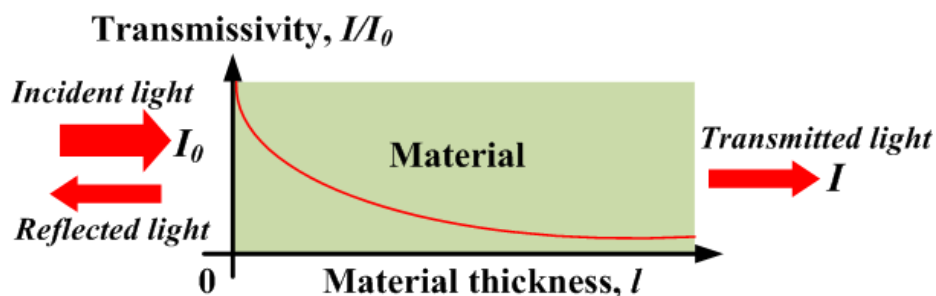


Figure 3.1 Schematic diagram of Beer-Lambert absorption of an incident light.

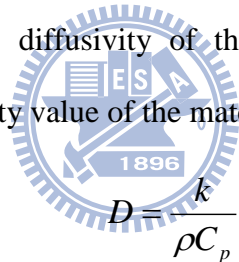
The transmissivity ( $T$ ),  $I/I_0$ , is defined as the ratio of the intensity of light that passes through the material over the intensity of the incident light. If the part of the incident light is reflected, the absorptivity ( $A$ ) by the material can be calculated as follows:

$$A = 1 - (R + T) \quad (3.3)$$

where  $R$  is the reflectivity of the material. In general, a higher light absorption of the material leads to enhance the machining efficiency. Hence the laser absorptivity of the machined material can be increased in a number of different ways, for instance, by increasing surface roughness, oxide, and microstructure or depositing a thin film on material surface [72]. On the other hand, thermal diffusion depth  $d$  of the machined material is another key factor that affects the surface temperature distribution and can be represented as follows [37]:

$$d = 2(D\tau)^{1/2} \quad (3.4)$$

where  $D$  and  $\tau$  are the thermal diffusivity of the lattice and the laser pulse duration, respectively. The thermal diffusivity value of the material is given by:



$$D = \frac{k}{\rho C_p} \quad (3.5)$$

where  $k$  is the thermal conductivity,  $\rho$  is the material density, and  $C_p$  is the specific heat. Based on the Eqs. (3.4) and (3.5), the thermal diffusion depth of the machined material increases with increasing the thermal diffusivity, the laser pulse duration, or decreasing the material density and the specific heat.

The processing efficiency is affected by the dimensions of the heat affected zone, the optical characteristics of the material, and other energy losses (such as laser ablation and vaporization processes). Figure 3.2 shows the sequence diagrams of absorption events varying with absorbed energy. Typical processing phenomena between the pulsed laser radiations and interacted materials can be divided to six steps that include the heating, melting, vaporizing, ablating, ionizing, and burning, depending on laser fluence (or laser power density) and

interaction time. For instance, low melting point materials such as Pb, Zn, Sb, Sn, and Cd metals in the corresponding power density values for melting and vaporizing are approximately from 2-5 W/mm<sup>2</sup> to 10<sup>2</sup> W/mm<sup>2</sup>. Ferrous materials such as nickel alloys in the corresponding power density values for melting and vaporizing are approximately from 10<sup>2</sup> W/mm<sup>2</sup> to 10<sup>4</sup> W/mm<sup>2</sup>. Moreover, good thermal and electrical conductors such as Cu, Al, and Au metals and refractory materials such as W, Va, Ta, and Mo in the corresponding power density values for melting and vaporizing are approximately from 10<sup>4</sup> W/mm<sup>2</sup> to 10<sup>6</sup> W/mm<sup>2</sup>, respectively [73].

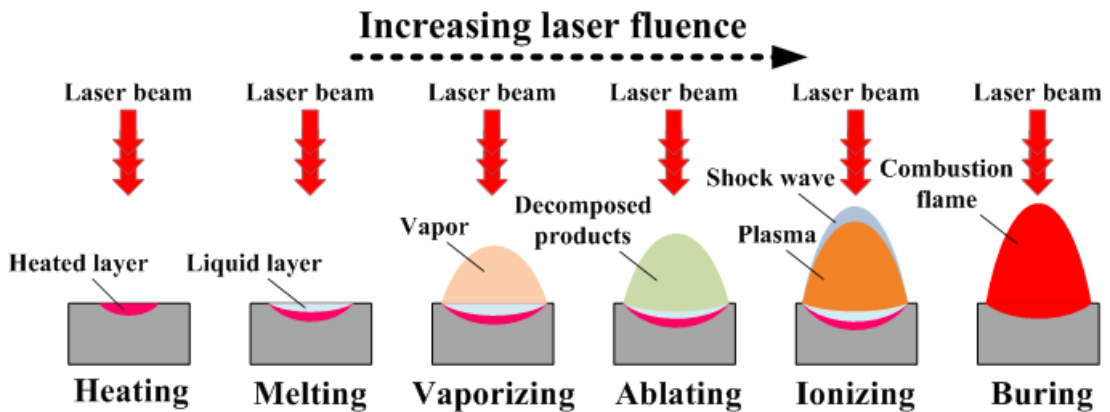


Figure 3.2 Sequence diagrams of absorption events varying with absorbed energy.

### 3.1.2 Laser direct writing and laser-induced backside writing

Laser direct writing is defined that the laser beam passes through the focusing lens and directly focuses on the workpiece upper surface. Laser direct writing can create the designed patterns and remove unnecessary materials, as shown in Fig. 3.3(a). This processing method has been developed to produce the surface texturing, scribing, marking, grooving, depositing, milling, cutting, drilling, and patterning by varying laser-material interactions. However, the laser direct writing on the normal transparent materials such as glass, sapphire, and fused silica substrates requires very high laser fluence to generate nonlinear absorption through multi-photon ionization; moreover, this method implies a low machining efficient and a poor

process [74]. In order to enhance the laser machining efficiency for transparent materials, laser-induced backside writing (often called laser-induced backside etching) is developed and used to manufacture the shallow structures. In general, the backside writing technology can be distinguished as laser-induced backside wet etching (LIBWE) [75-77], laser-etching at a surface adsorbed layer (LESAL) [78], and laser-induced backside dry etching (LIBDE) [79-81].

Figure 3.3(b) shows the schematic diagram of laser-induced backside writing, where the laser beam passes through the transparent workpiece and then focuses on the metallic interface. The focused laser beam energy is absorbed at the interface between the backside layer of the transparent workpiece and the metallic target. Furthermore, the ablation plume is generated in the target surface to machine the backside layer of transparent workpieces. Due to the high temperature of the ablation plume, the removed material in this process is melted, evaporated, and mixed with the target material. After the laser-induced backside writing, some metallic elements are compounded and penetrated into the transparent workpiece. In order to improve these disadvantages mentioned above, the laser-induced backside process is improved by coating a layer of high absorption paint on the backside layer of transparent workpieces to enhance the laser beam absorption and to replace the metallic target [73].

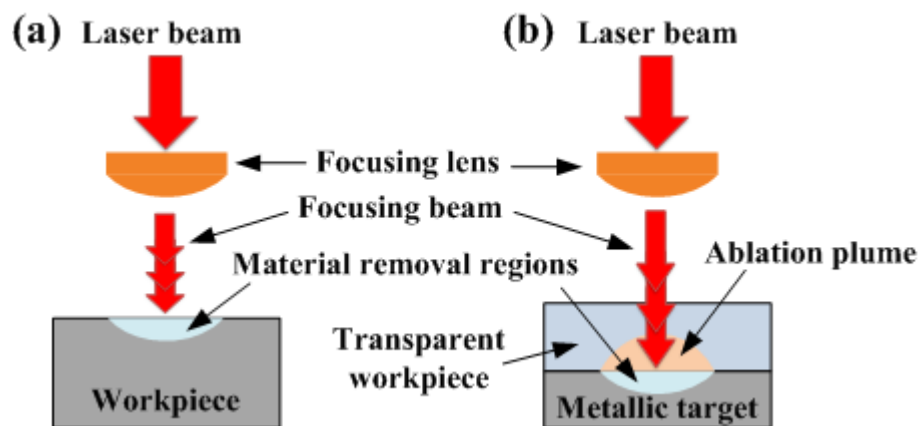


Figure 3.3 Schematic of laser direct writing (a) and laser-induced backside writing (b).

### 3.2 Laser processing parameters

Laser processing parameters including the laser exposure time, the pulse repetition frequency, the scanning speed of galvanometers, and laser fluence were used to remove unnecessary materials or to perform surface treatment in this dissertation. Figure 3.4 depicts the schematic diagram of pulsed laser output parameters. The laser average power ( $P_a$ ) can be represented as Eq. (3.6).

$$P_a = E \times F_r \quad (3.6)$$

where  $E$  and  $F_r$  are each pulsed laser energy and pulse repetition frequency, respectively. The pulsed energy can be defined as the power of the incident laser over time in seconds, and the unit is expressed in joules (J). The pulse repetition frequency can be defined as the number of laser pulses over time in seconds, and the frequency unit is expressed in hertz (Hz). The pulsed repetition frequency is the inverse of the pulsed period (T). Moreover, the actual average power can be measured by a laser power meter during the laser process. The unit of average power is watts (W). The laser peak power ( $P_p$ ) can be calculated as Eq. (3.7).

$$P_p = \frac{E}{t} \quad (3.7)$$

where  $t$  is the laser pulse width. The laser fluence (F) can be calculated as follows:

$$F = \frac{E}{A} \quad (3.8)$$

where  $A$  is the laser spot cross-section area normal to the laser direction. The units of laser fluence and laser spot cross-section area are  $\text{J}/\text{cm}^2$  and  $\text{cm}^2$ , respectively. For the laser material manufacturing process, the laser exposure time ( $t_e$ ) is another key factor and can be calculated as Eq. (3.9).

$$t_e = t \times F_r \quad (3.9)$$

The exposure time is a period during which a laser beam is incident on the material surface, and the unit is measured in seconds. The exposure time also referred as laser pulse duration or

irradiation time.

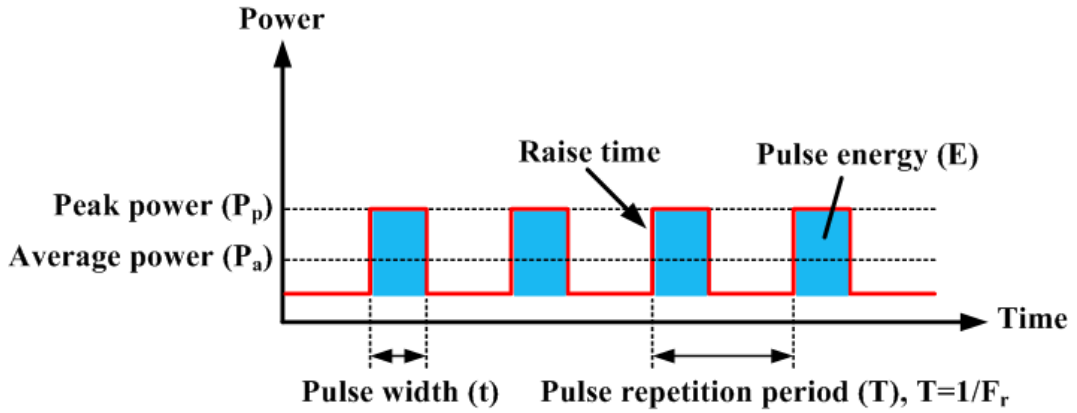


Figure 3.4 Schematic diagram of laser pulse output parameters.

The focused spot size of laser beam determines the maximum laser fluence as the laser power is set. Therefore, the focused spot size is an important factor for material processing. Figure 3.5 shows the characteristics of a laser beam when it passes through a focusing lens. Assuming a propagating Gaussian beam in free space, the diameter of focused spot size ( $2w_f$ ) at the beam waist can be derived as Eq. (3.10).

$$2w_f = 2.44 \frac{\lambda f}{2w_L} \quad (3.10)$$

where  $\lambda$  is the laser wavelength,  $f$  is the focal length of the focusing lens, and  $2w_L$  is the diameter of incident parallel laser beam before the focusing lens. The diameter of focused spot size as a function of axial distance  $z$  from the beam waist is given by [82]:

$$2w(z) = 2w_f \left[ 1 + \left( \frac{\lambda z}{\pi w_f^2} \right)^2 \right]^{1/2} \quad (3.11)$$

The Rayleigh range  $z_R$  is defined as the distance from the beam waist  $w_f$  to the transverse plane where the beam diameter is  $2\sqrt{2} w_f$  and can be calculated from:

$$z_R = \frac{\pi w_f^2}{\lambda} \quad (3.12)$$

The distance between these two points is called the depth of focus  $b$  of the beam and represents the permissible working distance for which the spot size variation can be ignored.

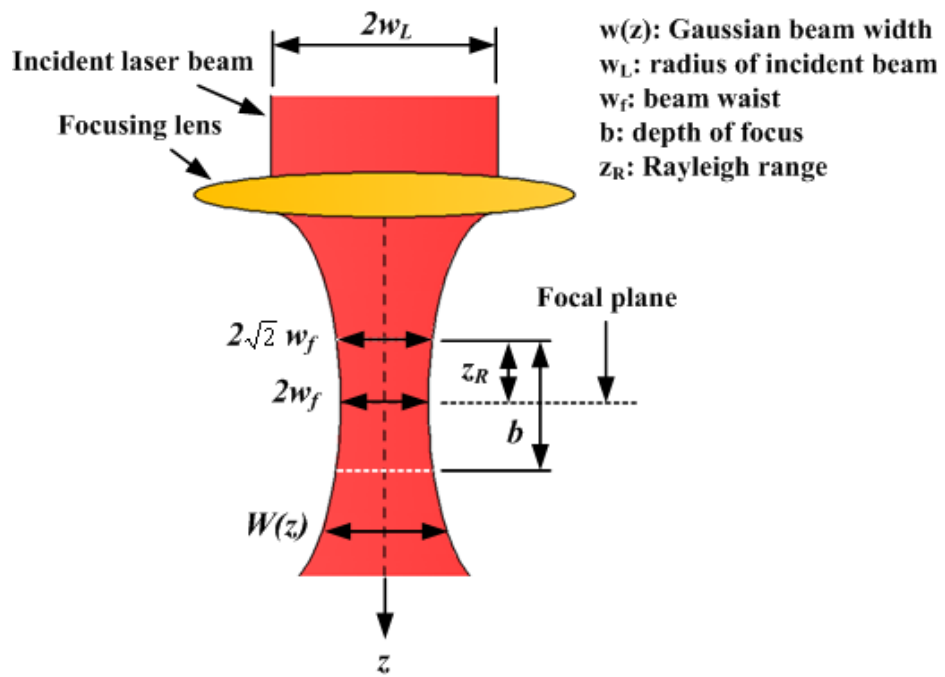
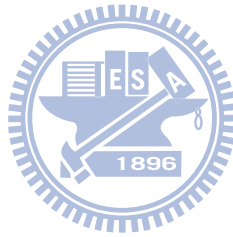


Figure 3.5 Characteristics of a focusing laser beam.



## Chapter 4 Experimental apparatus and sample preparation

### 4.1 Laser scribing of indium tin oxide (ITO) thin films deposited on various substrates for touch panels

#### 4.1.1 Laser scribing system

Figure 4.1 shows the schematic diagram of the experimental system. The fundamental neodymium-doped yttrium aluminum garnet crystal (Nd:YAG) laser processing system with wavelength of 1064 nm is used for patterning isolation lines in ITO thin film of the cell phone touch panels. The laser beam was delivered through a 5X beam expander, three reflective mirrors, and a high-speed galvanometric scanning head. The f-theta focusing lens was used in this system with the focal length of 184 mm and the scanning area of 112 mm × 112 mm. The Z-axis movable table with ball-screw mechanism in focusing alignment is used to adjust the focal point and finally to bring the focused beam on the ablated surface of ITO thin films.

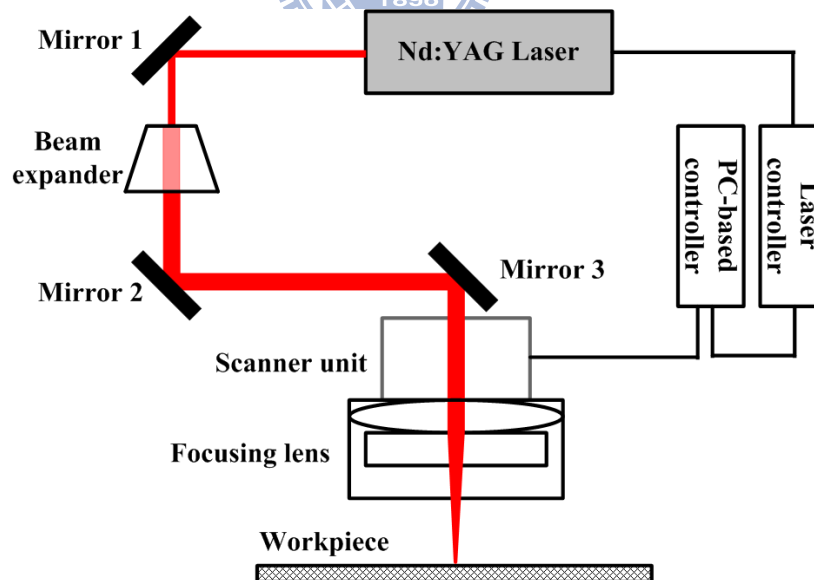


Figure 4.1 Schematic diagram of Nd:YAG laser system.

In this laser operation system, the pulse repetition frequency is adjusted from 1 kHz to 100 kHz. The values of the maximum pulse repetition rate, the maximum average output



power, and the pulse width are 100 kHz, 20.8 W, and 76 ns (FWHM). The energy per pulse exceeds 10 mJ. The nominal values of the laser beam diameter at the exit port and average spot size are approximately 0.8 mm and 30  $\mu\text{m}$ , respectively. The complete specification of the laser processing system is presented in Table 4.1. The average output power, the pulse repetition rate, the scanning speed of the galvanometer scanners, and the pulse duration of the Nd:YAG laser can be adjusted by the Human Machine Interface (HMI), which is a self-developed program written by Borland C++ Builder software to monitor and control the processes.

Table 4.1 Fundamental Nd:YAG laser system parameters.

|                                   |                   |
|-----------------------------------|-------------------|
| Wavelength (nm)                   | 1064              |
| Average Power (W)                 | >20               |
| Spatial Mode                      | TEM <sub>00</sub> |
| Beam Diameter, $\pm 10\%$ , (mm)  | 0.8               |
| Pulse Repetition Frequency, (kHz) | 1-100             |
| Pulse width, (ns)                 | 34-76             |

#### 4.1.2 Sample preparation

The Nd:YAG laser scribing system is designed to perform the electrode isolation of ITO thin films coated on different substrate materials including soda-lime glass, PC, and COC. Table 4.2 summarizes the properties of ITO films deposited on three substrate materials used in our experiment. These ITO films have sheet resistance of 315  $\Omega/\square$ , 433  $\Omega/\square$ , and 390  $\Omega/\square$ , respectively. Figure 4.2 depicts the dimensional layouts of the three cell phone touch panel models. The width of all three substrates is 48 mm. The lengths of the substrates are 90 mm, 100 mm, and 90 mm, shown in Fig. 4.2(a) to 4.2(c), respectively. Moreover, the thicknesses of the substrates are 0.7 mm, 1 mm, and 0.7 mm.

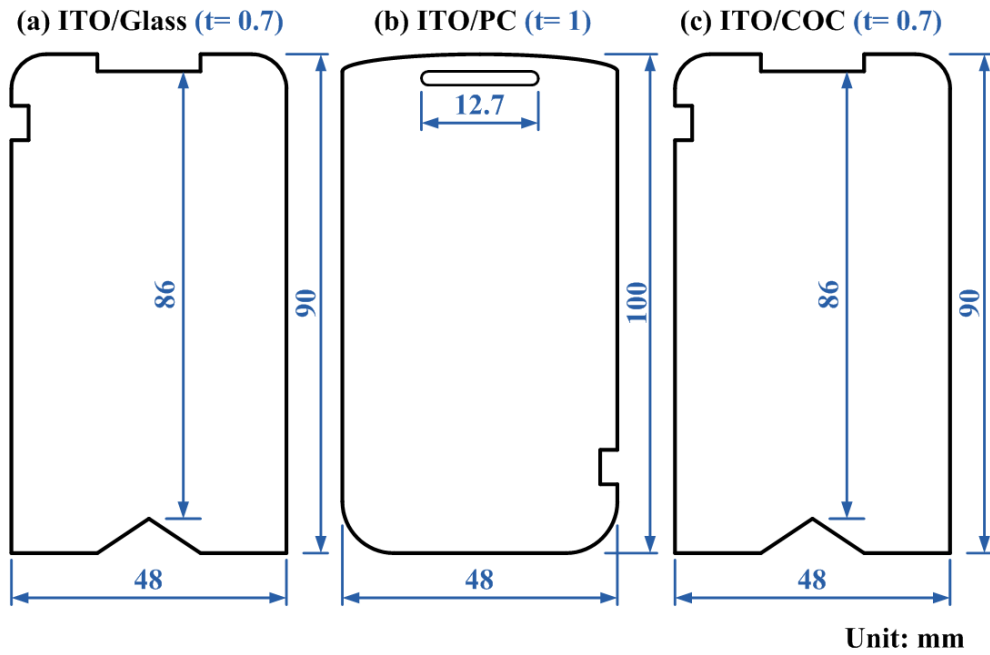


Figure 4.2 Dimensions and shapes of cell phone touch panels used in this study.

The commercial ITO thin films were deposited on soda-lime glass, PC, and COC substrates by sputtering method. An oxide buffer layer is deposited on each substrate to enhance adhesion between the ITO films and substrates. Before the thickness of these films coated on different substrates was measured by SEM, a focused ion beam (FIB) system (model SMI-3050, SEIKO, Japan) was used to mill a step for easy thickness observation. In order to protect the specimen surface during the FIB process, the silicon oxide ( $\text{SiO}_2$ ), platinum (Pt), and carbon (C) were coated on ITO film surface, respectively. Figure 4.3 shows the cross-section view SEM pictures of ITO films deposited on different types of substrates. Figure 4.3(a) shows that the ITO film is on soda-lime glass substrate. The ITO film and buffer layer were approximately 20 nm and 100 nm thick, respectively. Figure 4.3(b) shows that the ITO film is coated on PC material. The ITO film and buffer layer were approximately 30 nm and 140 nm thick, respectively. Figure 4.3(c) shows that the ITO film is coated on COC material. The ITO film and buffer layer were approximately 20 nm and 100 nm thick, respectively.

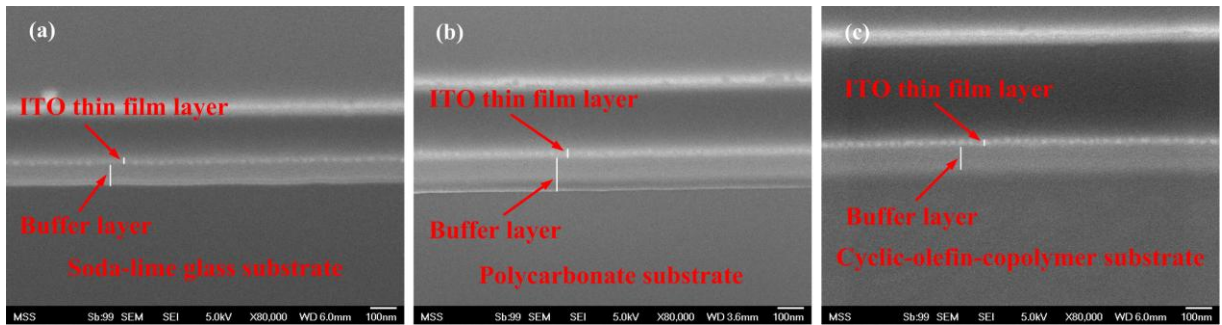


Figure 4.3 SEM cross-section views of ITO films deposited on different types of substrates. (a) ITO/Glass, (b) ITO/PC, and (c) ITO/COC.

Table 4.2 Optical and electrical properties of ITO film deposited on different substrates.

| Properties                            | ITO/Glass      | ITO/PC         | ITO/COC        |
|---------------------------------------|----------------|----------------|----------------|
| Thickness (film / substrate)          | 20 nm / 0.7 mm | 30 nm / 1.0 mm | 20 nm / 0.7 mm |
| Transmittance (%) (400-800 nm)        | 85.5           | 86.4           | 86.8           |
| Sheet resistance ( $\Omega/\square$ ) | 315            | 433            | 390            |
| Surface roughness (RMS, nm)           | 0.926          | 1.034          | 1.553          |

Figure 4.4 shows the surface roughness in 3D images of ITO films deposited on different substrates scanned by the atomic force microscope (Veeco di Dimension 3100, USA). The surface measuring region is  $1 \mu\text{m} \times 1 \mu\text{m}$ . The measured values of the root mean square (RMS) are of 0.181 nm, 0.936 nm, and 1.343 nm for the blank soda-lime glass, PC, and COC substrates, respectively, shown in Fig. 4.4(a) to 4.4(c). The RMS values of the ITO films deposited on soda-lime glass, PC, and COC optical materials are of 0.926 nm, 1.034 nm, and 1.553 nm, respectively, as shown in Fig. 4.4(d) to 4.4(f). Compared surface characteristic of the deposited films, the surface roughness of ITO film deposited on soda-lime glass substrate is better than that deposited on PC and COC substrates because of the flat glass surface.

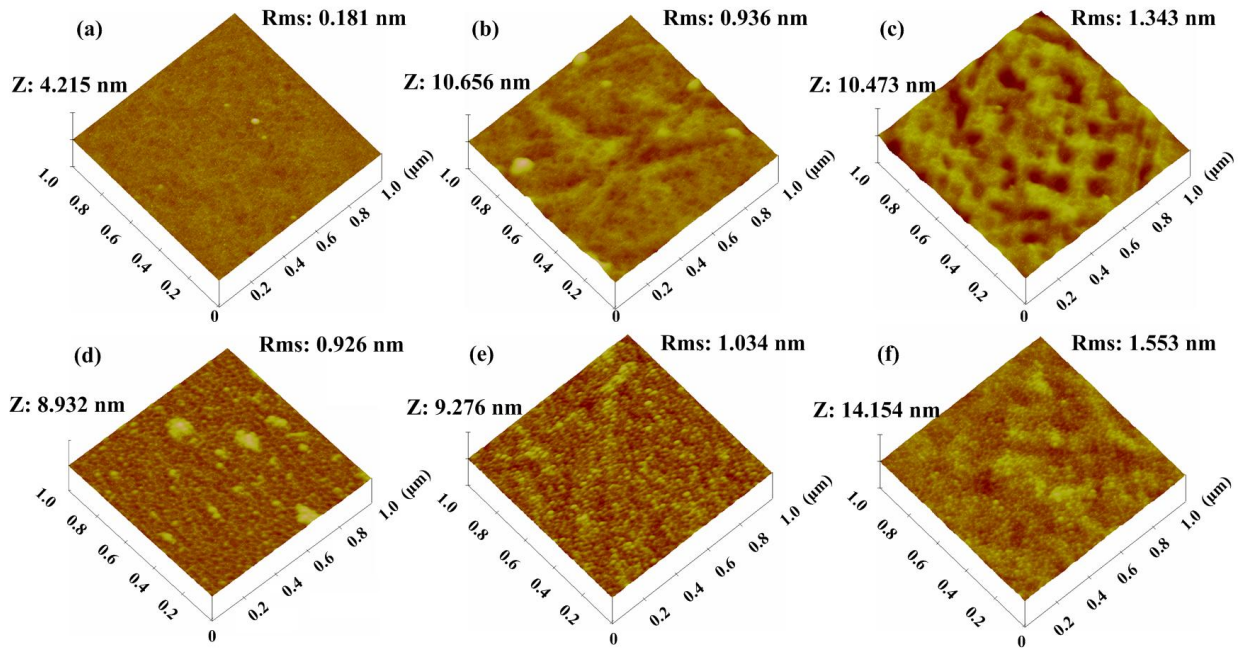
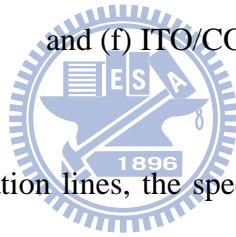


Figure 4.4 Surface roughnesses of different substrates and ITO films deposited on substrates.

(a) Soda-lime glass substrate, (b) PC substrate, (c) COC substrate, (d) ITO/Glass, (e) ITO/PC, and (f) ITO/COC.



Before the laser scribes isolation lines, the spectrometer (Lambda 900 UV/Vis/NIR) as shown in Fig. 4.5 [83] is used to measure the transmittance and reflectance of the ITO films deposited on the various substrates. The measured data is shown in Fig. 4.6. The light transmittance values at 1064 nm wavelength are approximately 76.88 %, 75.92 %, and 72.37 % for ITO/Glass, ITO/PC, and ITO/COC materials, respectively. The corresponding light reflectance values are 20.06 %, 23.53 %, and 25.17 %. After the laser scribes isolation lines, the surface morphology was measured by a 3D laser confocal microscope (KEYENCE VK-9700) as shown in Fig. 4.7. The electrical resistivity before and after laser scribing is measured by the four-point probe measurement system (QUATEK CH-5601Y) as shown in Fig. 4.8.



Figure 4.5 A photo of a spectrometer (Lambda 900 UV/Vis/NIR) [82].

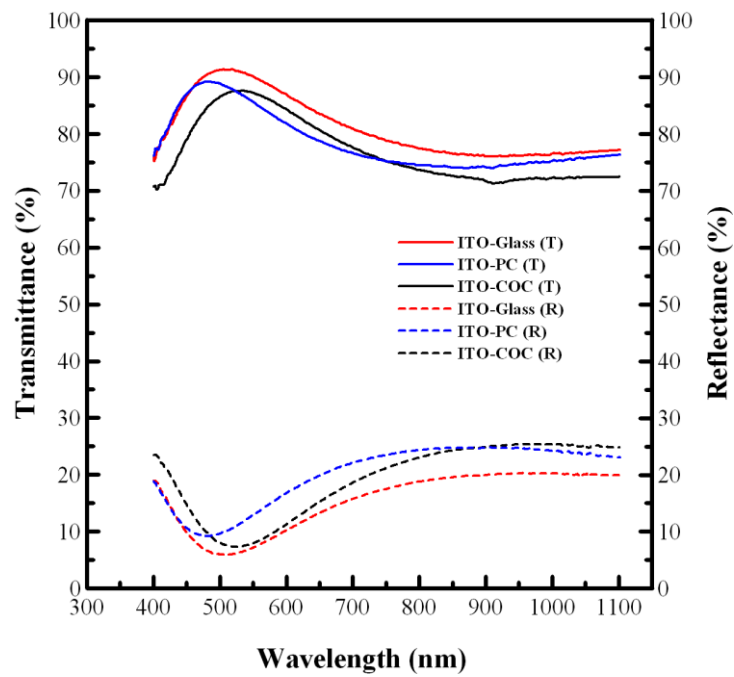


Figure 4.6 Light transmittance and reflectance versus wavelength for ITO thin film at various substrates.



Figure 4.7 A photo of a 3D laser confocal microscope (KEYENCE VK-9700, Japan).

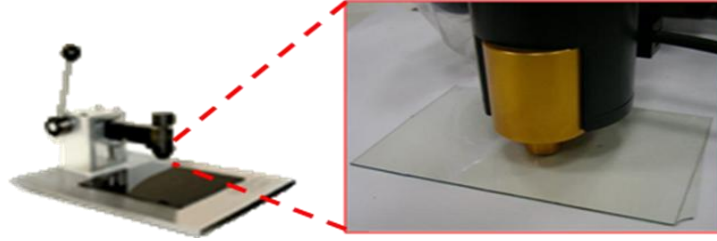


Figure 4.8 A photo of a four-point probe measurement system (QUATEK CH-5601Y).

### 4.1.3 Isolation line patterning parameter

Nanosecond pulsed Nd:YAG laser with wavelength of 1064 nm has been used to pattern the isolation lines of ITO thin films. The operation variables and constrains for patterning isolation lines were carried out as following:

- (1) The optimal average laser power was fixed at 2.2 W, and the pulse repetition frequency was fixed at 100 kHz.
- (2) The laser exposure times were adjusted from 10  $\mu$ s to 100  $\mu$ s, and the interval between each pulse was set by 10  $\mu$ s.
- (3) Machining time varies from 0.76 s to 2.25 s to pattern the isolation line length of 50 mm.
- (4) The position of laser focal point and workpiece fixture was fixed for laser patterning different thicknesses of these substrates.

## 4.2 Surface wettability of silicon substrates enhanced by laser ablation

### 4.2.1 Apparatus and sample

The current experimental studies focus on surface texturing created in silicon substrates using the diode-pumped, Q-switched Nd:YAG laser system (Optowave model Awave-IR). Figure 4.9 shows a schematic diagram of the experimental set-up used to fabricate rough-patterned templates. A laser beam via three reflective mirrors, a beam expander, two galvanometer scanners, and a telecentric lens is focused on the experimental surface. The nominal laser-beam diameter at the exit port and average spot size are 0.8 mm and 30  $\mu$ m,

respectively. The laser is emitted at the fundamental wavelength of 1064 nm, the maximum laser average power is approximately 20 W, and pulse repetition rate ranges from 20 kHz to 100 kHz. The laser pulse width is ranging from 34 to 76 ns. Additionally, the commercial silicon plates with single-face polished were chosen as substrates. The substrate is 500  $\mu\text{m}$  thick and 100 mm in diameter.

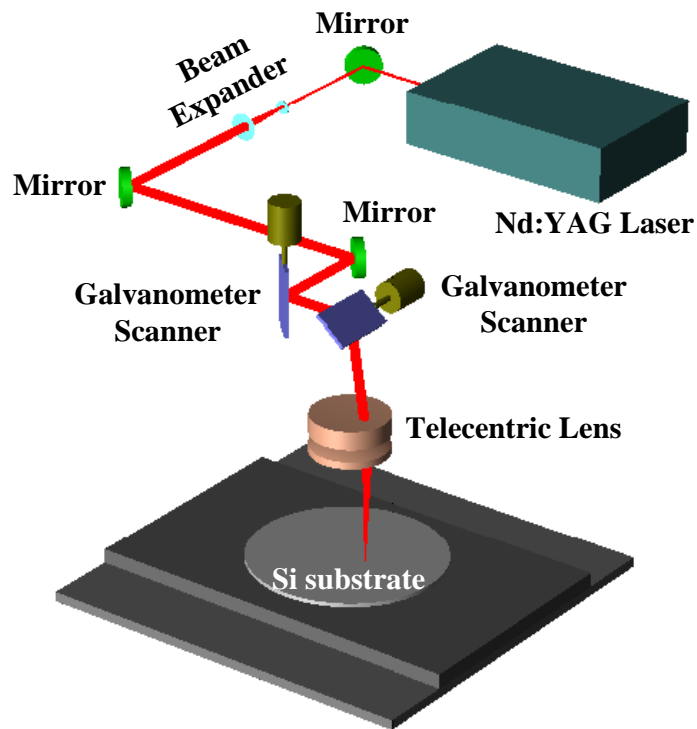


Figure 4.9 Schematic diagram of the Nd:YAG laser set-up.

Characterization measurements were performed with the following techniques and instrumentations. The surface micrograph and roughness patterns were measured using the SEM and the 3D confocal laser-scanning microscope (VK-9700, KEYENCE Corp.) with 0.1 nm resolution of vertical and horizontal measured range, respectively. The laser power was monitored with a Gentec Electro-Optics SOLO 2 laser power meter. The light reflection rate of the silicon substrate was measured using the spectrophotometer system (LAMBDA 900). Droplet characteristics, such as the contact angle, size, and shape were measured with a

FTA 188 video contact angle analyzer as shown in Fig. 4.10 [84].



Figure 4.10 A photo of a FTA 188 video contact angle analyzer [84].

#### 4.2.2 Surface texturing by laser ablation

Figure 4.11 shows the laser ablation path of parallel lines with equal scan spacing. The dimensions of ablated area and ablated pitch are  $20\text{ mm} \times 20\text{ mm}$  and  $65\text{ }\mu\text{m}$ , respectively. In addition, the experimental parameters including laser fluence ( $F$ ) and laser pulse duration ( $Pd$ ) were adjusted to create patterns of different roughness via a PC-based controller.

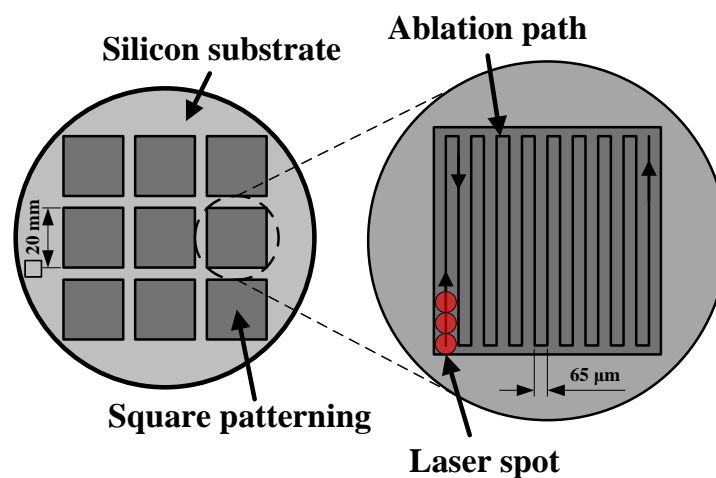


Figure 4.11 The illustration of laser ablation path.



### 4.2.3 Wettability characteristics of the textured surfaces

Droplet experiments were carried out to describe the wettability behavior of the textured surfaces used in this research. A droplet volume of 3  $\mu\text{L}$  was gently placed on the textured surfaces in these experiments using a micropipette and droplet shapes were captured to measure the apparent contact angle by a FTA 188 video contact angle analyzer. A cross-sectional view of the droplet on three types of target surfaces is shown in Fig. 4.12. From Fig. 4.12(a), a contact angle  $\theta_s$  of a liquid droplet on a flat solid surface is given by the classical Young's equation:

$$\cos\theta_s = \frac{\gamma_{SV} - \gamma_{SL}}{\gamma_{LV}} \quad (4.1)$$

where  $\gamma_{SV}$ ,  $\gamma_{LV}$ , and  $\gamma_{SL}$  are the interfacial free energies per unit area of the solid-vapor, liquid-vapor, and solid-liquid interfaces, respectively. The Young's equation describes wetting on an ideal surface, i.e., a smooth and chemically homogeneous surface at equilibrium. As for the rough surface of Fig. 4.12(b), Wenzel [16] proposed a theoretical mode describing the contact angle,  $\theta_r$ , by modifying Eq. (4.1) as follows:

$$\cos\theta_r = \frac{r(\gamma_{SV} - \gamma_{SL})}{\gamma_{LV}} = r \cos\theta_s \quad (4.2)$$

where  $r$  is the roughness factor defined as the ratio of the actual area of a rough surface to the geometric projected area. Because this factor is always larger than 1, the surface roughness enhances the hydrophilicity of hydrophilic surfaces and also enhances the hydrophobicity of hydrophobic ones. The liquid droplet is the only contact with the top side of the microstructures, as shown in Fig. 4.12(c). Cassie and Baxter [85] described this condition and the contact angle  $\theta_r$  for the microstructure surface using Eq. (4.3):

$$\cos\theta_r = \phi(\cos\theta_s + 1) - 1 \quad (4.3)$$

where  $\phi$  is the fraction of the solid-liquid interface below the drop. Equations (4.1) and (4.2) only consider droplets on a single morphological surface. Textured surfaces, however, often have complex morphologies that result in different surface energy configurations by laser

processes. Therefore, the characteristics of liquid droplets related to the surface roughness and the microstructure were investigated.

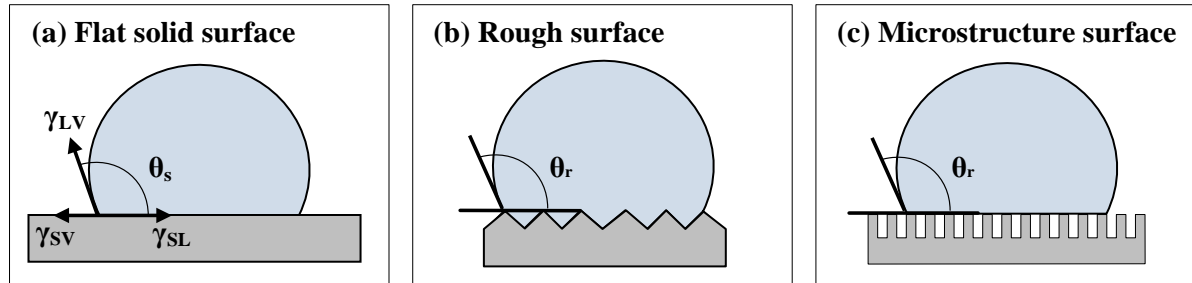


Figure 4.12 Cross-sectional view of the droplet on target surfaces.

### 4.3 Hydrophobic templates with rough patterns fabricated by laser micromachining for liquid droplets generation

#### 4.3.1 Laser micromachining system

Figure 4.13 shows a schematic representation of the experimental set-up used to fabricate rough patterned templates. The beam from a diode-pumped, Q-switched Nd:YAG laser (Optowave model Awave-IR) passes through three reflective mirrors, a beam expander, a galvanometer system, a telecentric lens with a 100 mm of focal length and a glass substrate and finally focuses on a metallic target. The nominal diameter of the laser beam at the exit port and average spot size are 0.8 mm and 30  $\mu\text{m}$ , respectively. The designed patterns are fabricated by deflected beam generated from the two mirrors of the galvanometer scanner. The emitted laser wavelength is the fundamental wavelength (1064 nm). The maximum pulse repetition rate, the maximum average output power, and the pulse width of full width at half maximum (FWHM) are 200 kHz, 20.8 W, and 76 ns, respectively. Energy per pulse exceeds 10 mJ. The average output power, the pulse repetition rate, the scanning speed of the galvanometer scanners, and the exposure time of the Nd:YAG laser can be adjusted by a Human Machine Interface (HMI), which is a program written by Borland C++ Builder software to monitor and control the process.

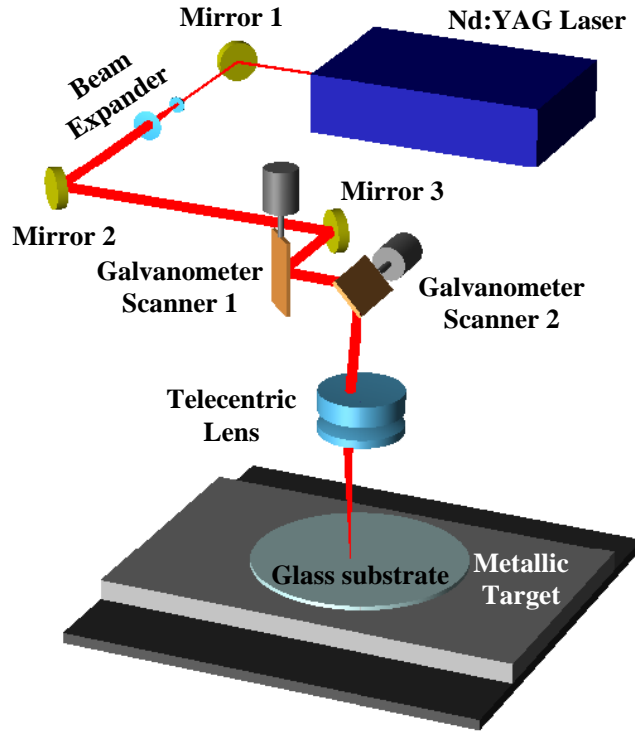
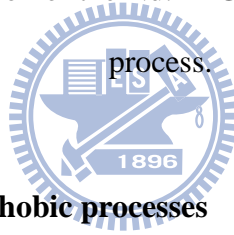


Figure 4.13 Schematic representation of the Nd:YAG laser process set-up for backside writing process.



### 4.3.2 Templates made by hydrophobic processes

Figure 4.14 illustrates the major fabrication steps for the hydrophobic template. The commercial soda-lime glass plates, shown in Fig. 4.14(a) were chosen as substrates due to their low cost and good thermal properties. The molar composition of soda-lime glass is mainly 72%  $\text{SiO}_2$ , 15%  $\text{Na}_2\text{O}$ , and 6%  $\text{CaO}$ ; but the glass also includes small portions of residual oxides of  $\text{MgO}$ ,  $\text{Al}_2\text{O}_3$ ,  $\text{SO}_3$ ,  $\text{Fe}_2\text{O}_3$ , and others. The soda-lime glass substrate is 0.55 mm thick and 100 mm in diameter. The top and bottom surfaces of the soda-lime glass were polished, producing surface qualities of 50/80 (dig/scratch). Figure 4.14(b) shows that the rough patterned templates are back-written by scanning the laser focused beam on the metallic target. The ablation plume generated in the metallic target reacts with the glass substrate and scratches cavities in it. Laser-induced high temperature caused the metallic evaporation and plasmas. The glass material removed in this process is first melted and ablated; then finally a

cavity is formed on the bottom glass and top metal surface [86]. In this study, the laser average power and pulse repetition rate were optimized to eliminate superficial thermal cracking on the glass substrate and exceed the threshold of ablating metal. A commercially available medium carbon steel (S45C) plate was placed below and in direct contact the glass plate substrate [87,88]. The thickness and surface roughness of medium carbon steel metal after grinding is 2 cm and  $0.402 \mu\text{m}$  (Ra), respectively. After the LBW process, the sample was cleaned by ultrasonic cleaning equipment for 1 h to remove ablation debris. Then, a 695 nm thick Teflon-(CF<sub>2</sub>)<sub>n</sub> thin film was deposited on the glass substrate using an Inductively Coupled Plasma Deep Reactive Ion Etching (ICP-DRIE) system (Surface Technology Systems), as depicted in Fig. 4.14(c). Figure 4.14(d) shows the schematic top view of a rough patterned template. The designed array pattern consists of 10-row by 10-column annular grooves. The inner diameter of each annular groove is 1 mm. The center distance from the annular groove to its neighboring annular groove is 3 mm.

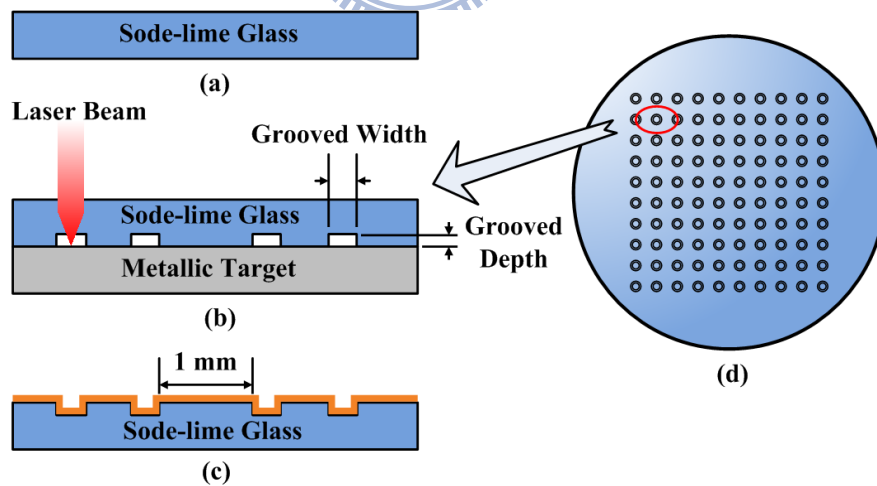


Figure 4.14 Major fabricated processes of the hydrophobic template. (a) Polished soda-lime glass substrate on top and bottom surfaces, (b) laser-induced backside writing process on glass backside surface, (c) Teflon thin film coating, and (d) template top view.

Characterization measurements were performed with the following techniques and instrumentations. The transmittance and reflectance of the soda-lime glass substrate were measured using the Spectrophotometer system (LAMBDA 900). Figure 4.15 shows the cross-section view of the droplet on a machined template. Droplet characteristics, such as contact angle, size, and shape, were measured with the FTA 188 contact angle and surface tension analyzer. The grooved surface roughness and profile of patterns were measured by the atomic force microscope (Veeco di Dimension 3100) with a vertical resolution of 0.1 nm and a Talyscan 150 Profilometer with a vertical resolution of 2 nm, respectively. Laser power was monitored with a Gentec Electro-Optics SOLO 2 laser power meter.

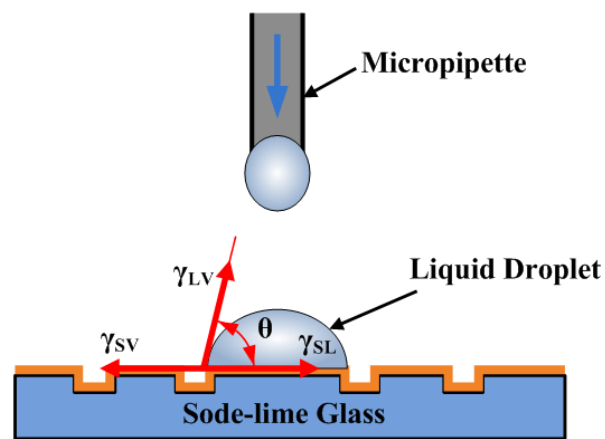


Figure 4.15 Schematic of the cross-section view of the droplet on a machined template.

#### **4.4 Characteristics of Ni-Ir and Pt-Ir hard coatings surface treated by pulsed Nd:YAG laser irradiation**

##### **4.4.1 Numerical simulation process**

Finite element analysis is a powerful tool for engineering prediction of material characteristics and manufacturing process parameters. We conduct thermal analysis on a FUJI J05 WC mold with Ir-based coatings treated by the laser using ANSYS software. The physical properties of the WC mold shown in Table 4.3 were used to evaluate temperature distribution. Because the single-pulse exposure time is very short on the material surface during laser

heating, the effects of convection and radiation were ignored in our simulation conditions. Some assumptions made are shown in the following:

- (1) The thermal properties of all analyzed materials are isotropic.
- (2) Laser beam intensity distribution is a  $TEM_{00}$  mode.
- (3) Any phase change phenomena is ignored in the heating process.
- (4) The heat conduction and thermal radiation are ignored in the parameter setting.

The finite element model was applied to analyze the temperature distribution of the WC molds with 10 mm in diameter and 5 mm thick. The mold samples were coated with different compositions of Pt-Ir and Ni-Ir alloys. The optical absorption parameters of specimens, including Ir-25 at.% Pt, Ir-50 at.% Pt, Ir-75 at.% Pt, Ir-25 at.% Ni, Ir-50 at.% Ni, and Ir-75 at.% Ni, were respectively calculated using ANSYS software for the mathematical model and temperature distribution. There are three analysis steps proceeded in ANSYS software: (1) pre-processing (2) solution processing (3) post-processing. The pre-processing includes modeling and meshing processes. To set up the thermal properties in the modeling process, the input parameters consist of density, thermal conductivity and specific heat of the WC mold substrate as shown in Table 4.3. The diameter and thickness of the WC mold were defined as 10 mm and 5 mm, respectively. Moreover, the grid size of the element unit was set 20  $\mu\text{m}$  during the meshing process. The boundary conditions for solution processing include the load of the material, initial temperature, and laser parameters. The initial temperature was 27°C, the pulse repetition frequency was fixed at 100 kHz, the single-pulse exposure time was 100  $\mu\text{s}$ , and a function-editor was employed to define the Gaussian heat source in our simulation condition. In the simulation processing, the surface temperature was approximately 1500°C; hence, the average power levels were adjusted to approach the high surface temperature of various Pt-Ir and Ni-Ir alloys thin films, depending on the absorption characteristics of the film alloys.

Table 4.3 Physical characteristics of Tungsten carbide (WC) mold for glass molding.

| Physical Properties  | FUJI J05 WC |
|--|-------------|
| Young modulus (GPa)  | 650         |
| Poison ratio   | 0.21        |
| Density (kg/m <sup>3</sup> )   | 14650       |
| Thermal conductivity (W/ m-°C )  | 63          |
| Coefficient of thermal expansion ( $\times 10^{-6}/\text{ }^\circ\text{C}$ ) | 5.1         |
| Specific heat (J/ Kg-°C )  | 314         |

#### 4.4.2 Laser surface treatment system

Figure 4.16 depicts the experimental system. The system consisted of a Nd:YAG laser, a beam delivery system, a focusing lens, and a PC-based controller. The Nd:YAG laser used in this study is a fundamental laser generator produced by Aptowave Corporation with a wavelength of 1064 nm. The pulse repetition rate can be adjusted from 1 kHz to 100 kHz and the maximum laser output power is 20W. The beam delivery system includes three perfect mirrors and a 5X magnification beam expander. The z-axis feeding system can adjust the position of the laser focusing point. The working distance of the used focusing lens is of 134 mm and the minimum spot size is of about 15  $\mu\text{m}$  focused in this Nd:YAG laser system.

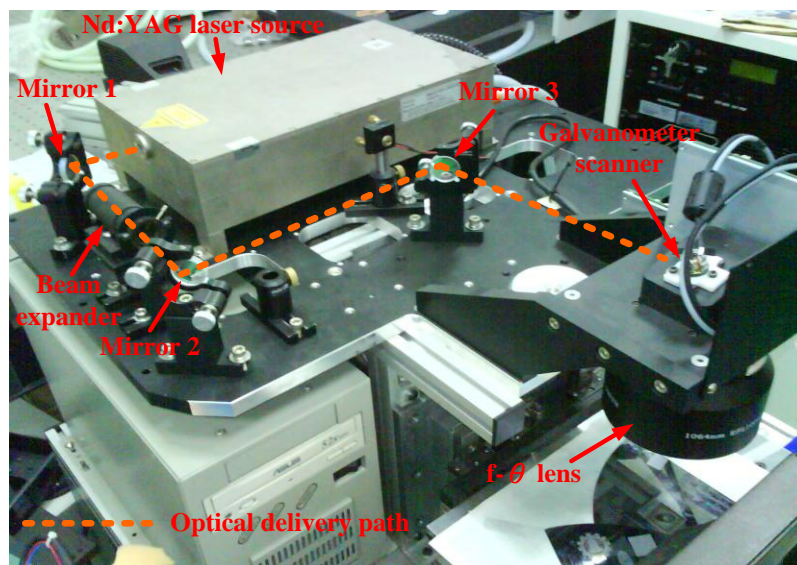


Figure 4.16 The experimental setup of the Nd:YAG laser system.

#### 4.4.3 Sample preparation

The Ni-Ir and Pt-Ir films of various compositions were deposited by an ion source assisted magnetron sputtering system (ISAMSS) on a substrate at a heated temperature of 400°C. The RF powers of 100 W at Pt and Ni targets, and the tunable RF powers of 100-200 W and 100-300 W at the Ir target are operated, respectively. The deposition conditions are conducted under an vacuum environment of less than  $5 \times 10^{-6}$  Torr, a working gas of argon, and a working pressure at 5 mTorr. All the Pt-Ir and Ni-Ir thin films were approximately 300 nm thick. To obtain better Pt-Ir and Ni-Ir alloy adhesion on the mold, a chromium (Cr) layer of 50 nm thickness was deposited on the WC mold surface to act as a buffer layer. The AFM (Veeco di Dimension 3100, USA) was used to measure the film surface roughness of the Pt-Ir and Ni-Ir alloy thin films before and after laser surface treatment, as shown in Fig. 4.17. A field emission scanning electron microscope (FESEM, Model JEOL JSM-7401F) with energy dispersive x-ray spectrometry (EDS) as shown in Fig. 4.18 was used to observe the cross-sectional view and to analyze chemical composition of the films. The microhardness and reduced modulus of these films were measured with a nanoindentation tester (Hysitron TriboLab, USA) equipped with a Berkovich indenter as shown in Fig. 4.19 [89].



Figure 4.17 A photo of an atomic force microscope (Veeco di Dimension 3100, USA).





Figure 4.18 A photo of a field emission scanning electron microscope (FESEM, Model JEOL JSM-7401F).

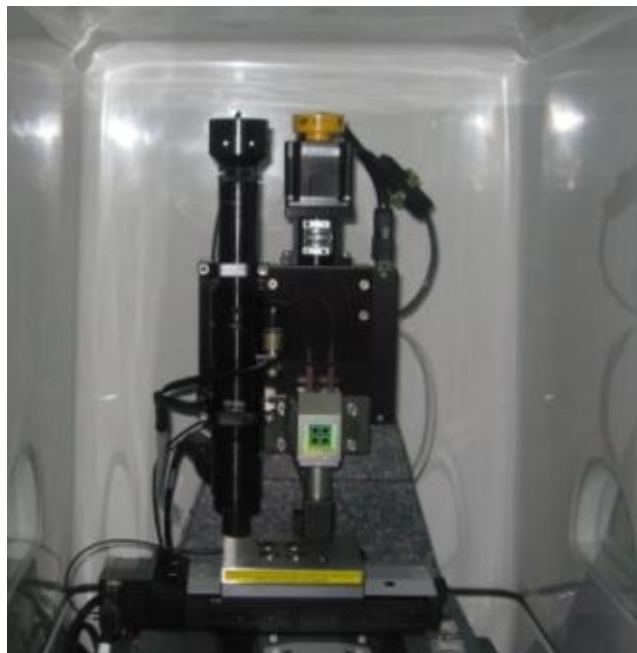


Figure 4.19 A photo of a nanoindentation tester (Hysitron TriboLab, USA) [89].

## Chapter 5 Experimental results and discussion

### 5.1 Laser scribing of indium tin oxide (ITO) thin films deposited on various substrates for touch panels

#### 5.1.1 Surface morphology, isolation line width, and depth

Figure 5.1 shows the photo-pictures of isolated lines on three different substrates by a fundamental Nd:YAG laser source. Figure 5.2 to 5.4 shows the photos of the scribed isolation lines on different substrates with 400 times magnification using the 3D laser confocal microscope. Figure 5.2(a) to 5.2(c) shows the surface morphologies of patterned isolated lines subjected to 10  $\mu$ s and 20  $\mu$ s exposure time on ITO/Glass, ITO/PC, and ITO/COC materials, respectively. The individual ablated mark, discontinuous isolated regions, and the residual area were clearly observed in the ITO films along a laser scribing path. The ablated marks on the ITO/PC are wider than that on both ITO/Glass and ITO/COC. The ablated mark widths of ITO/Glass and ITO/COC are similar. This is due to the thickness difference between these blank substrates, which result in different laser spot sizes focused on the ITO substrate surface. Moreover, the ITO/Glass substrate has slightly higher absorptance than the other two substrates that a few heat affected zone appeared near the ablated mark as shown in Fig. 5.2(a).

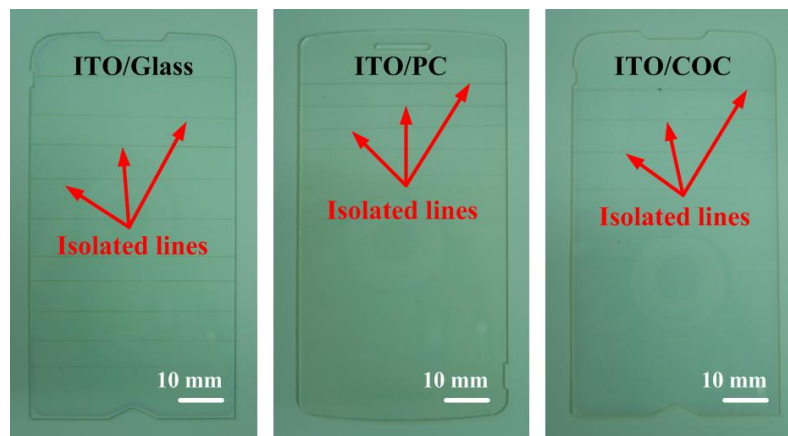


Figure 5.1 Pictures of laser scribing of isolated lines on different substrates.

When the exposure time was extended to 30  $\mu\text{s}$  and 60  $\mu\text{s}$ , the residual areas along a scribed path were gradually decreased, shown in Fig. 5.3. No clear existed residual areas on the scribed path of these substrates can be seen and shown in Fig. 5.3(a) to 5.3(c). There are no apparent damaged spots or melt burrs observed on the ablated substrate surfaces. Furthermore, the scribed lines shown in Figs. 5.3(b) and 5.3(c) have slightly heat affected zone near the scribing edge when the laser exposure time is 60  $\mu\text{s}$ . The scribed lines shown in Fig 5.3(a) obviously have wide heat affected zone near the scribing edge of ITO/Glass substrates. Figure 5.4 shows the surface morphologies of isolated lines on different substrates scribed by laser at laser exposure time of 70  $\mu\text{s}$  and 100  $\mu\text{s}$ . Figure 5.4(a) reveals the wide heat affected zone along the scribing path on ITO/Glass substrates. When the laser exposure time is longer than 60  $\mu\text{s}$ , the scorches and splashes also can be clearly observed in the isolated lines on PC and COC substrates. The photo evidences are shown in Figs. 5.4(b) and 5.4(c).

Figure 5.5 shows a relationship of isolation line width and depth versus the various exposure times. The isolated line width increases with increasing exposure time for all of ITO substrates. When the PC is adopted as the substrate, the line width is average 10  $\mu\text{m}$  wider than that of glass and COC adopted as substrate under the studied exposure time ranges, shown in Fig. 5.5(a). The PC thickness is 1 mm and thicker than the other two substrates, hence the thickness difference results in different laser spot size focused on the ITO substrate surface. The ITO thickness on PC is 30 nm compared to 20 nm thick on the other two, and the ITO thickness difference causes the larger thermal diffusion difference and results in ablated spots difference. Moreover, the isolated line depth measured on the ITO/PC increases gradually with increasing exposure time, as shown in Fig. 5.5(b). Because the thermal stability of glass substrate is better than plastic substrate, the ITO/Glass results show that the isolated line depth is very close with increasing exposure time. The average depth of ITO/PC and ITO/Glass substrates are approximately 2  $\mu\text{m}$ . However, the isolated line depth measured on the ITO/COC is slightly low than other two substrates with increasing exposure time. The

average depth of ITO/COC substrates is approximately 1.25  $\mu\text{m}$ .

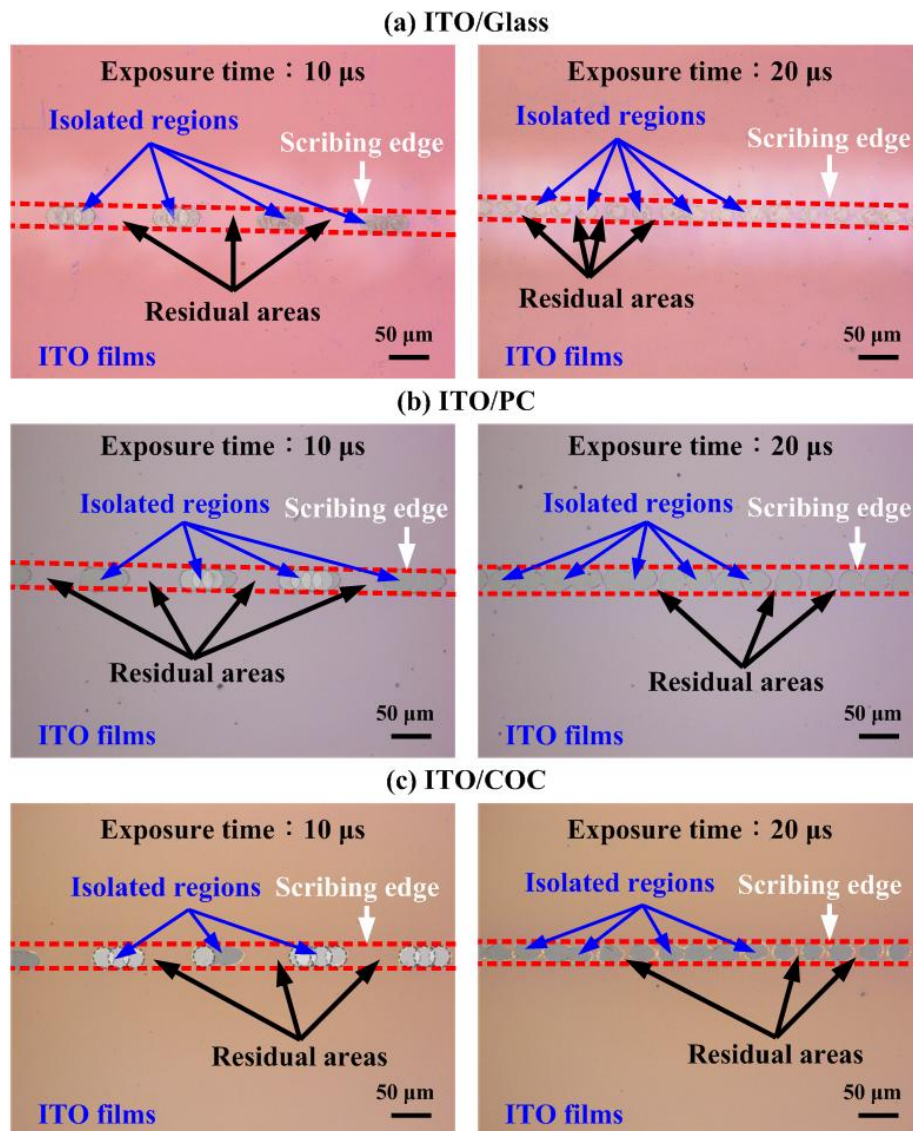


Figure 5.2 Surface morphologies of laser scribing of isolated lines at laser exposure time of 10  $\mu\text{s}$  and 20  $\mu\text{s}$  on different types of substrates coated indium tin oxide thin films. (a) ITO/Glass, (b) ITO/PC, and (c) ITO/COC.

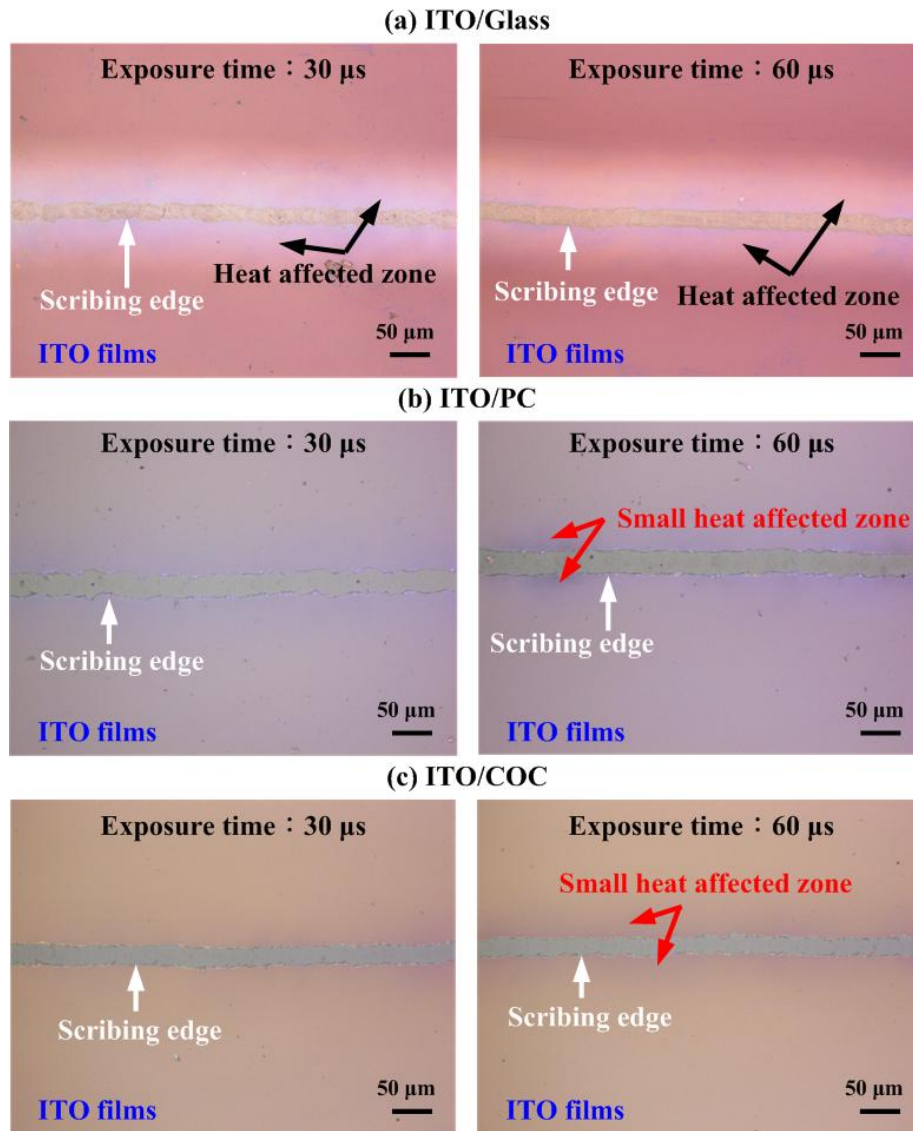


Figure 5.3 Surface morphologies of laser scribing of isolated lines at laser exposure time of 30 μs and 60 μs on different types of substrates coated indium tin oxide thin films. (a) ITO/Glass, (b) ITO/PC, and (c) ITO/COC.

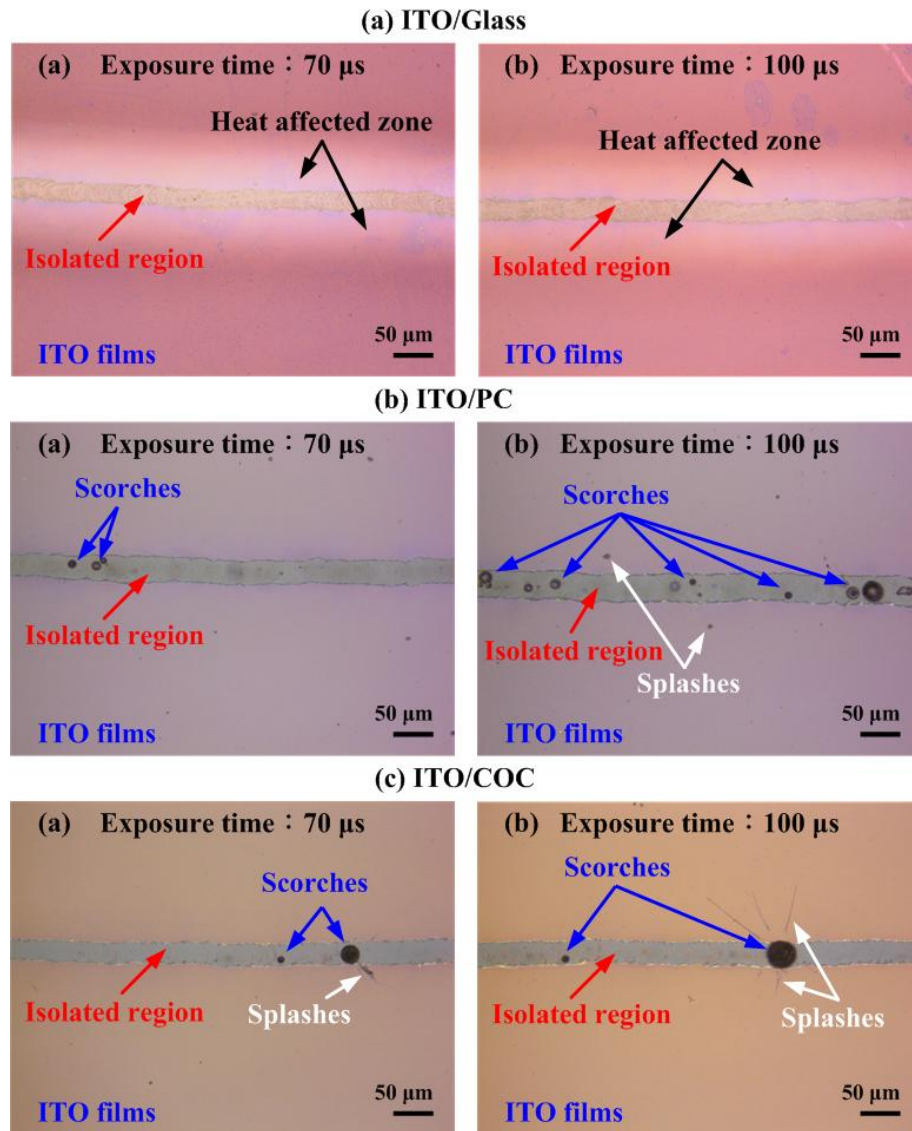


Figure 5.4 Surface morphologies of laser scribing of isolated lines at laser exposure time of 70  $\mu\text{s}$  and 100  $\mu\text{s}$  on different types of substrates coated indium tin oxide thin films. (a) ITO/Glass, (b) ITO/PC, and (c) ITO/COC.

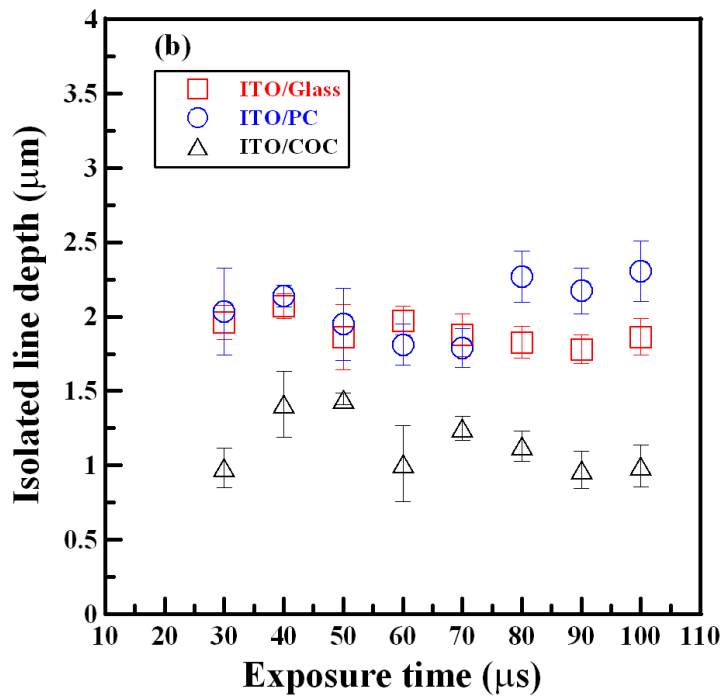
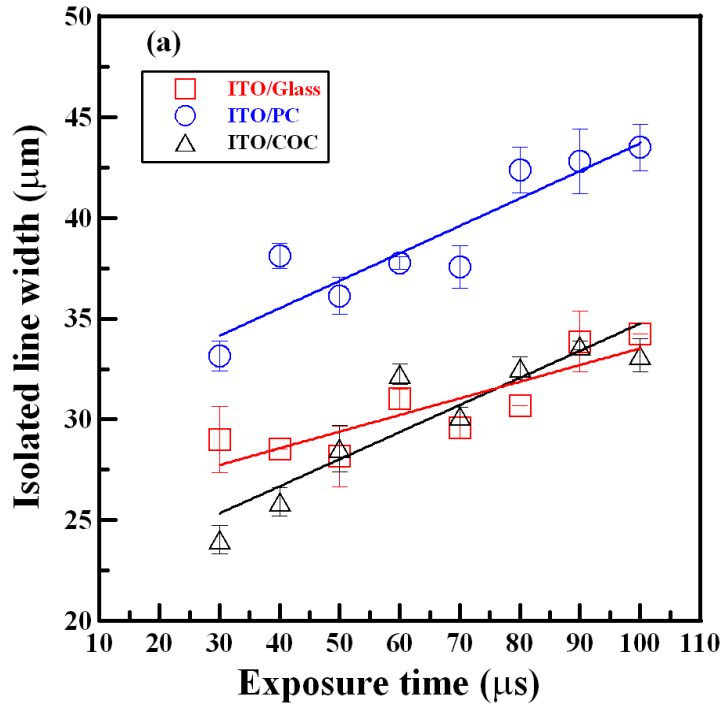


Figure 5.5 Relationship of isolated line width and depth on various exposure times. (a) Isolated line width versus different laser exposure time, and (b) isolated line depth versus different laser exposure time.

### 5.1.2 Electrical conductivity measurement

ITO films deposited on glass, PC and COC substrates with film thickness of 20 nm, 30 nm, and 20 nm were successfully isolated when laser exposure time is longer than 20  $\mu\text{s}$ . The results of electrical conductivity near the isolated line edge were measured by the four-point probe as shown in Fig. 5.6. The three dash-lines represent the original resistivity levels before laser scribing, and the symbols represent the measured data and the solid-lines are the regression result after laser scribing. All resistivity values after laser scribing were greater than the original resistivity. The measured results show that the resistivity values gradually increase with increasing the laser exposure time. Because the thicknesses of ITO films coated on glass and COC substrates are the same, thus the resistivity values after laser scribing are very similar. However, the thickness of ITO films coated on PC substrate is larger than others; the resistivity values are obviously larger than others.

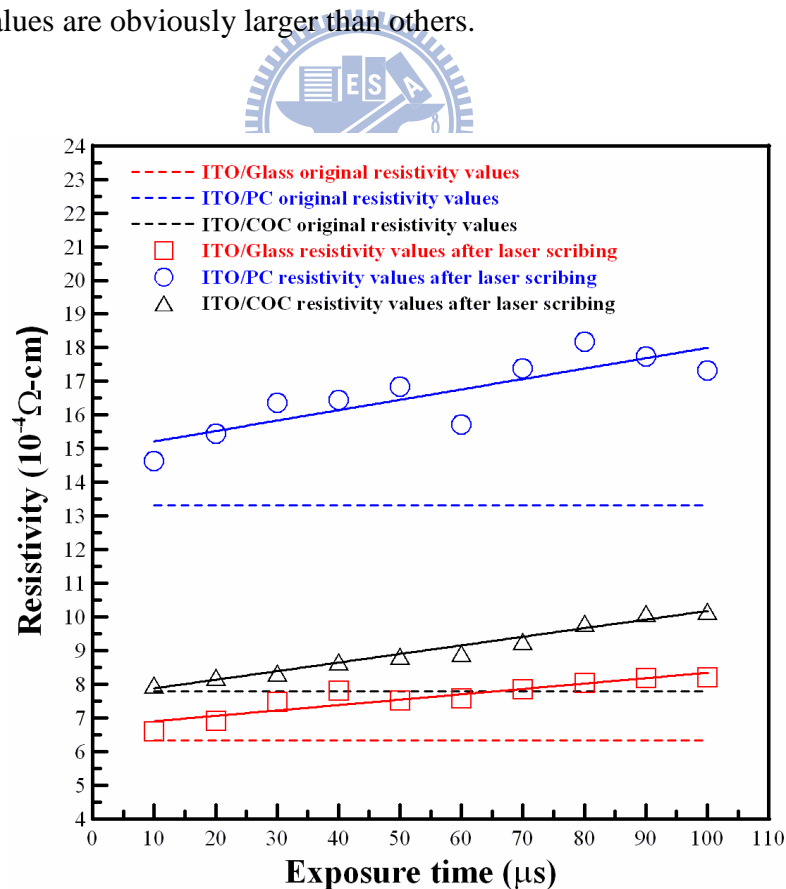


Figure 5.6 Electrical properties of ITO thin films coated on glass, PC, and COC with un-scribing and after laser scribing at different laser exposure time.



### 5.1.3 Summary

The direct writing technology and the nanosecond pulsed Nd:YAG laser were successfully used to fabricate the isolated lines on indium tin oxide films. The line patterns were discontinuous and led to residual films produced along a laser scribing path when laser exposure time is less than 30  $\mu$ s. The burned and damaged substrates can be observed by the 3D confocal laser scanning microscope when laser exposure time is larger than 60  $\mu$ s. Moreover, the partial burned areas including scorches and splashes were observed in scribed thin films on PC and COC substrates. When the exposure time is tuned within 30  $\mu$ s and 60  $\mu$ s, the better edge quality of the scribed lines can be obtained. After laser scribing of isolated lines, all of resistivity values of substrates coated on ITO films near the isolated line edge were greater than the original ones. Moreover, the isolated line width values increase with increasing laser exposure time.



## 5.2 Surface wettability of silicon substrates enhanced by laser ablation

### 5.2.1 Square patterning on silicon substrates

Figure 5.7 shows the light reflection rate of the untextured silicon substrate before the laser ablation, using a spectrophotometer system to measure the optical characteristics of the silicon substrate. The reflection rate is 32.5% for the Nd:YAG laser (1064 nm) wave band. The value of absorptivity ( $A$ ) varies with the reflectivity ( $R$ ). For opaque materials, the absorption rate can be calculated as  $A = 1 - R$ . Thus, the absorption rate of the untextured silicon substrate is 67.5%. The laser-ablated samples with square patterning under different test parameters are shown in Fig. 5.8. These images show the color change by different thermal effects on the textured surface.

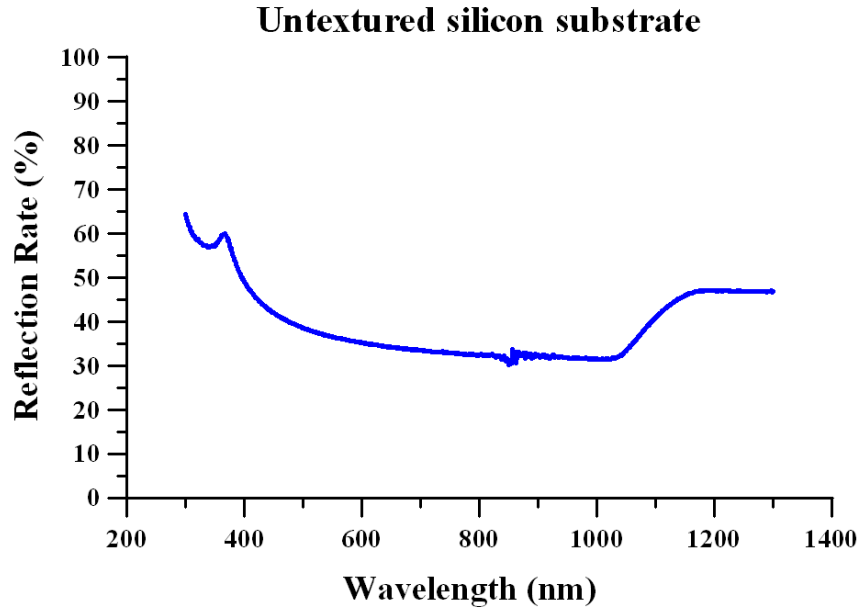


Figure 5.7 Optical characteristics of untextured silicon substrate.

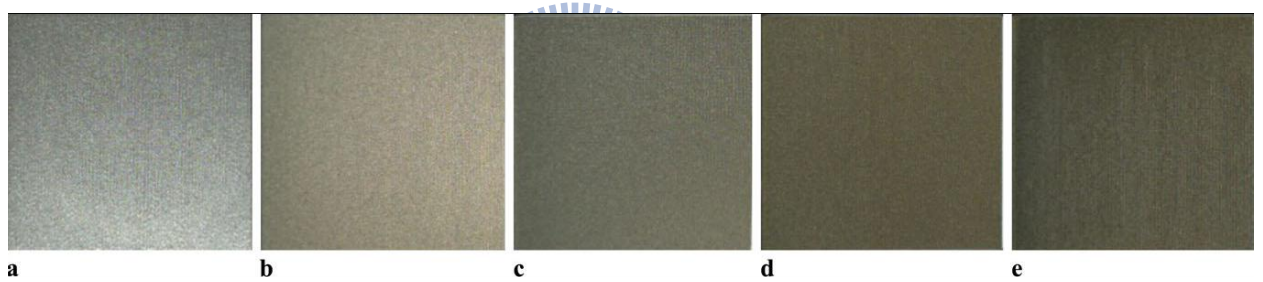


Figure 5.8 Some examples for laser-ablated squares on silicon substrate under different test parameters. (a)  $F=49.5 \text{ J/cm}^2$ ,  $Pd=100 \mu\text{s}$ , (b)  $F=53.8 \text{ J/cm}^2$ ,  $Pd=100 \mu\text{s}$ , (c)  $F=11.8 \text{ J/cm}^2$ ,  $Pd=300 \mu\text{s}$ , (d)  $F=53.8 \text{ J/cm}^2$ ,  $Pd=300 \mu\text{s}$ , (e)  $F=53.8 \text{ J/cm}^2$ ,  $Pd=500 \mu\text{s}$ .

### 5.2.2 Surface morphologies

In this study, the designed image was  $400 \times 400$  pixels from a BMP file translation for square patterning on silicon substrates; each bit size and scan spacing is about  $65 \mu\text{m}$ . After laser texturing was carried out on the silicon substrates, the surface morphologies of the microstructures produced by pulses with  $F$  ranging from  $17.1$  to  $92 \text{ J/cm}^2$  were analyzed using an SEM. Figure 5.9 shows the SEM micrographs at  $150\times$  magnification, demonstrating the

effect of Pd on the surface structures for  $F = 53.8 \text{ J/cm}^2$  and various Pd values of  $100 \mu\text{s}$  (a),  $300 \mu\text{s}$  (b), and  $500 \mu\text{s}$  (c), respectively. By increasing Pd, honeycombed structures with deeper holes are formed on the textured surface, as shown in Fig. 5.9(c). However, by decreasing these values, the laser spots are linked together and a structure with shallow grooves is formed (Fig. 5.9(a)). Figures 5.10 and 5.11 show a series of SEM micrographs at  $300\times$  magnification, demonstrating the effect of various F values on the surface structures for Pd values of  $300 \mu\text{s}$  and  $500 \mu\text{s}$ , respectively. By increasing the value of F, honeycombed structures with deeper and bigger holes are formed on the textured surface, and more molten slag is piled around these holes to create micro-sized craters. Figure 5.12 shows typical 3D topographies of textures formed at  $1000\times$  magnification on silicon surfaces for  $F = 70.7 \text{ J/cm}^2$  and various Pd values. The ablated volume of each maximum crater height was calculated using a 3D confocal laser scanning microscope analyzer, and the crater heights increased from  $18.9 \mu\text{m}$  (a) to  $45.7 \mu\text{m}$  (b) to and  $63.9 \mu\text{m}$  (c) as the Pd were increased to  $100 \mu\text{s}$ ,  $300 \mu\text{s}$ , and  $500 \mu\text{s}$ , respectively. Therefore, it appears that increasing Pd pushes the molten silicon outward and increases the crater height.

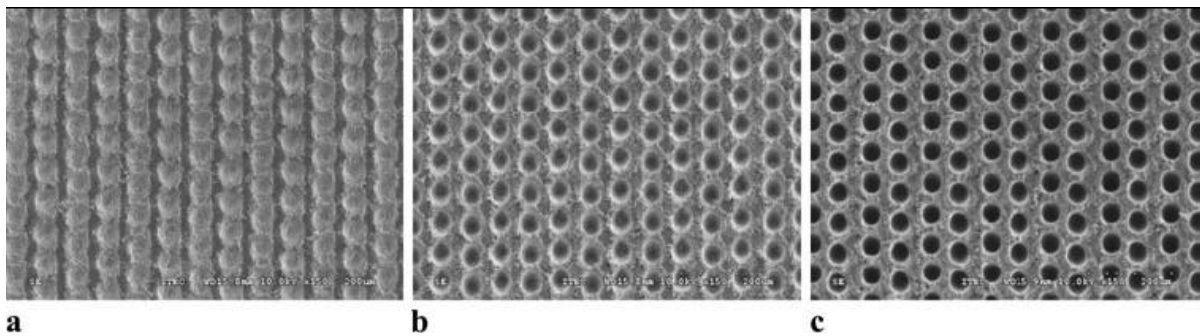


Figure 5.9 SEM micrographs showing the effect of laser pulse duration on surface structures

at  $F=53.8 \text{ J/cm}^2$ : (a) Pd= $100 \mu\text{s}$ , (b) Pd= $300 \mu\text{s}$ , (c) Pd= $500 \mu\text{s}$ .

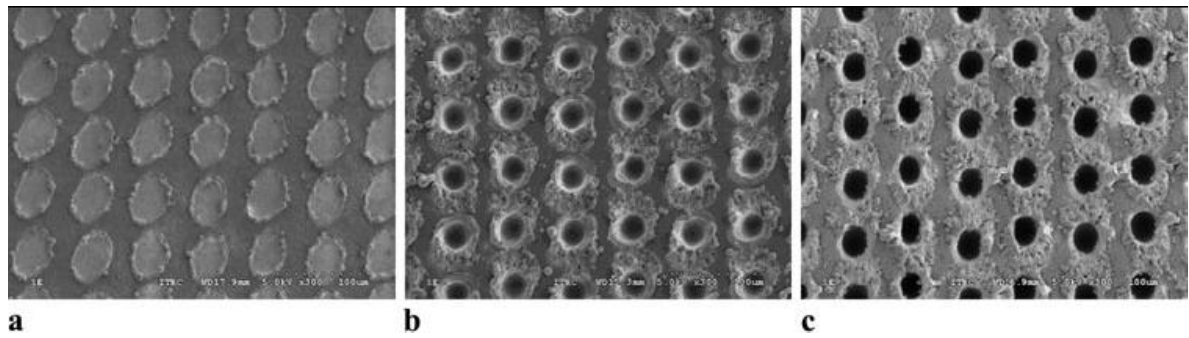


Figure 5.10 SEM micrographs showing the effect of laser fluence on surface structures at Pd=300  $\mu$ s: (a)  $F=17.1 \text{ J/cm}^2$ , (b)  $F=29.1 \text{ J/cm}^2$ , (c)  $F=37.5 \text{ J/cm}^2$ .

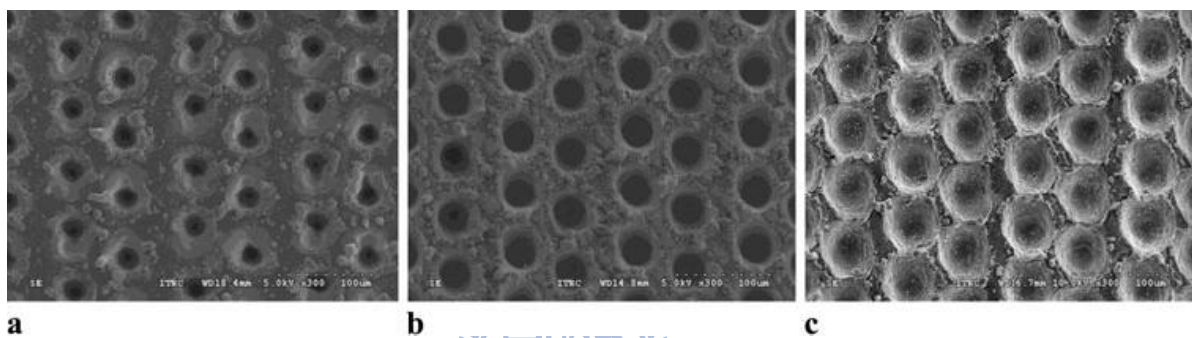


Figure 5.11 SEM micrographs showing the effect of laser fluence on surface structures at Pd=500  $\mu$ s: (a)  $F=29.1 \text{ J/cm}^2$ , (b)  $F=42.1 \text{ J/cm}^2$ , (c)  $F=92 \text{ J/cm}^2$ .

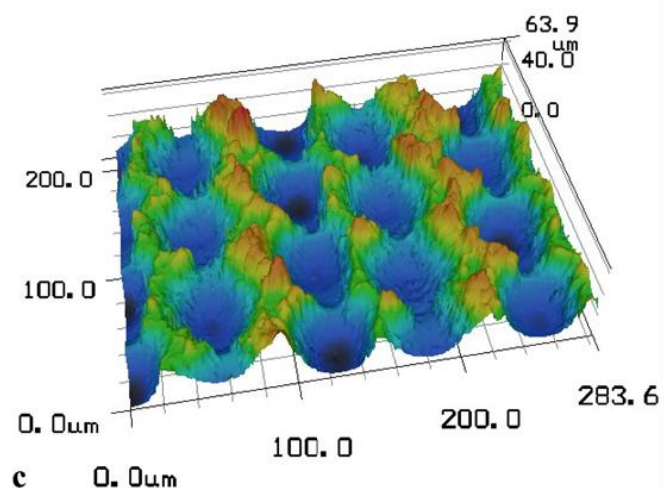
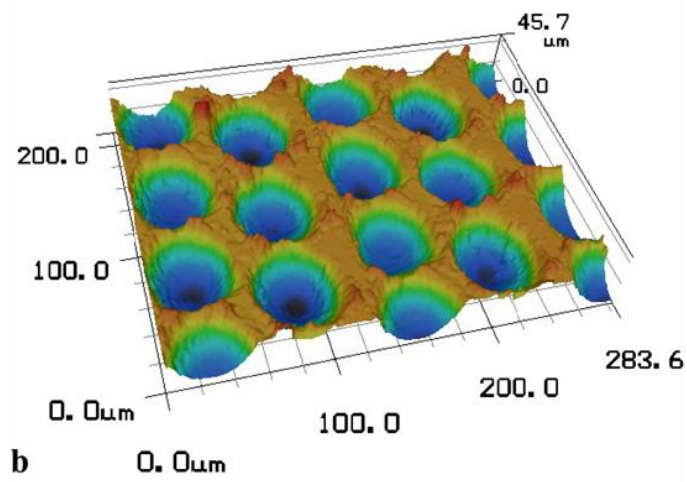
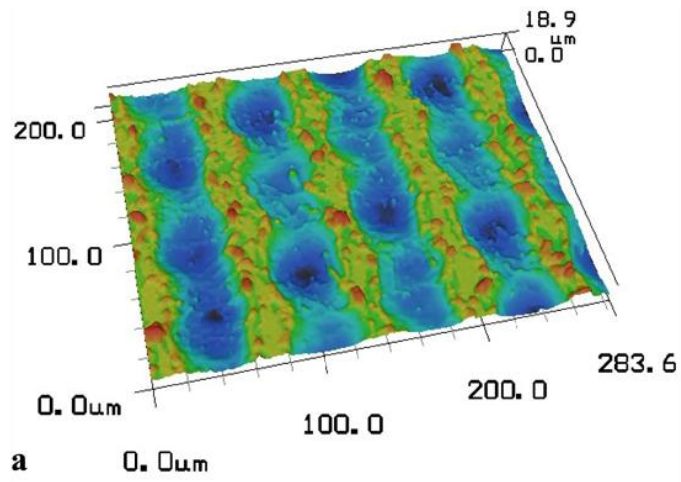


Figure 5.12 Typical 3D confocal laser scanning microscope topographies of texture formed on silicon surface at  $F=70.7 \text{ J/cm}^2$ : (a)  $Pd=100 \text{ } \mu\text{s}$ , (b)  $Pd=300 \text{ } \mu\text{s}$ , (c)  $Pd=500 \text{ } \mu\text{s}$ .

### 5.2.3 Surface roughness

Figure 5.13 shows the effect of the laser fluence on the surface roughness measured using the 3D confocal laser scanning microscope with a measuring region of  $200 \times 200 \mu\text{m}^2$ , for different test conditions. The results show that the surface roughness gradually increases with increasing Pd and demonstrate that the laser fluence has a strong effect on the surface roughness. This trend is similar to the results reported in the femtosecond laser micromilling of Si wafers [90] and in UV laser ablation of InP surfaces [91].

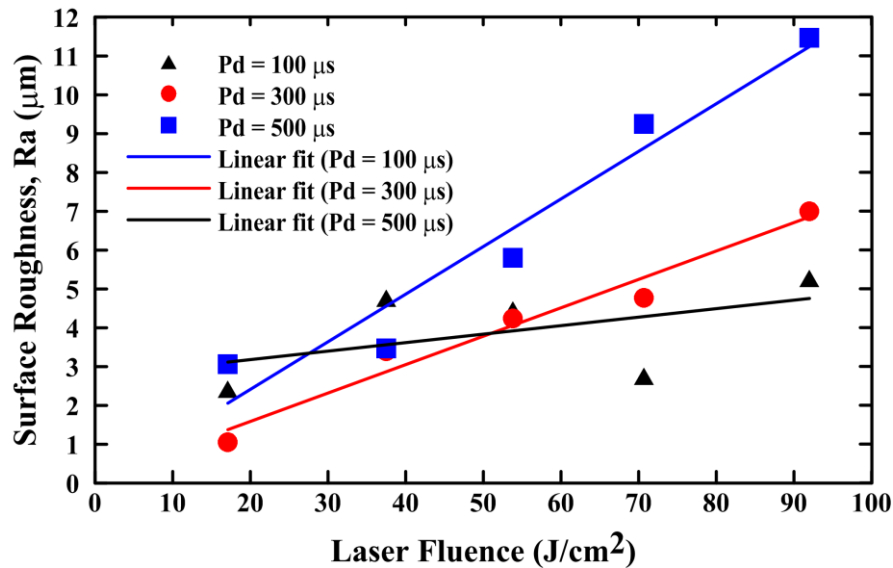


Figure 5.13 The effect of the laser fluence on the surface roughness for different conditions.

### 5.2.4 Enhanced wettability of liquid droplets on laser textured surfaces

After laser ablation of the silicon substrates, these surfaces exhibited complex morphologies and roughness that resulted in different surface energy configurations. Figure 5.14 displays typical image sequences of spreading liquid droplets on an untextured surface and a laser-textured surface with parameters of  $F=53.8 \text{ J}/\text{cm}^2$  and  $\text{Pd}=500 \mu\text{s}$ . According to Eq. (4.2), the surface roughness enhances the hydrophilicity of hydrophilic surfaces and enhances the hydrophobicity of hydrophobic ones. Thus, the results show that the water droplet spreads very quickly and almost disappears within 0.5167 s on a laser-textured surface,

compared to a contact angle of  $47.9^\circ$  on an untextured surface.

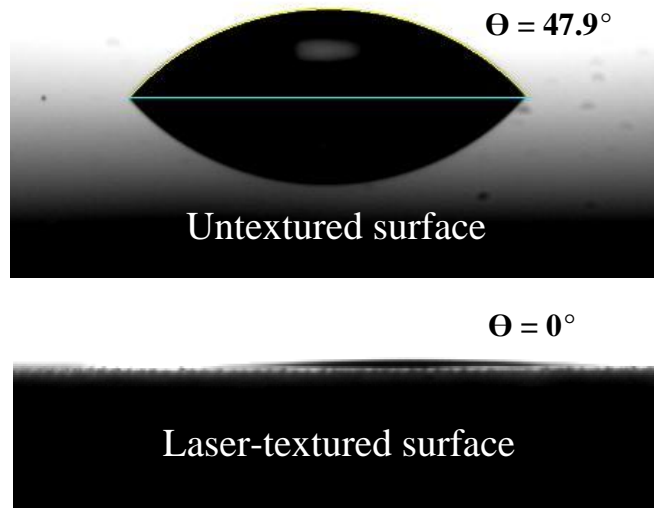


Figure 5.14 Comparison with images of spreading liquid droplets on untextured and laser-textured surfaces within 0.516 s.

### 5.2.5 Summary

This research had successfully demonstrated that the use of laser ablation to create rough patterns on a silicon substrate. Experimental parameters such as laser fluence and laser pulse duration were discussed. Using the SEM and the 3D confocal laser scanning microscope, the surface micrograph and roughnesses of the textured substrates were observed. By increasing the laser fluence and laser pulse duration during laser ablation, more molten slag was piled around the formed holes to create micro-sized craters and the crater height and surface roughness also increased. However, decreasing these parameters caused the laser spots to link together and a structure with shallow grooves was formed on the textured surface with decreased crater height and surface roughness. A typical example of placing a  $3 \mu\text{L}$  droplet on the laser-textured surface showed that the droplet spread very quickly and almost disappeared within 0.5167 s, compared to a contact angle of  $47.9^\circ$  on an untextured surface.

## 5.3 Hydrophobic templates with rough patterns fabricated by laser micromachining for liquid droplets generation

### 5.3.1 Surface morphologies of machined templates

Utilizing the spectrophotometer system to measurement the optical characteristics of soda-lime glass substrate, figure 5.15 shows the light transmissivity and reflectivity. Due to the high transparency (88.9 %) of the glass substrate for the Nd:YAG laser waveband, this study presents a combined method to connect laser-induced backside writing (LBW) process and laser-induced plasma assisted ablation (LIPAA) technique. This method fabricates rough array-patterns on a soda-lime glass substrate via metal target ablation. The array-pattern consists of 10-row by 10-column annular grooves. The diameter of each inner annular groove in the original design is  $1000\ \mu\text{m}$  ( $\emptyset_i$ ), and each grooved width in the original design is  $100\ \mu\text{m}$  ( $w$ ). After several preliminary trial tests for achieving machined conditions, the optimal laser parameters of 20 kHz pulsed repetition rate and 3W laser average power are determined. The effect of single-shot laser exposure time ( $T_s$ ) and number of passes ( $N_p$ ) on the surface profiles and morphologies of the glass substrate is investigated. Figure 5.16 shows an annular groove image taken by optical microscope. From Fig. 5.16(a) to Fig. 5.16(d), the  $T_s$  and  $N_p$  are  $2000\ \mu\text{s}$  and 20 times,  $3000\ \mu\text{s}$  and 20 times,  $2000\ \mu\text{s}$  and 22.5 times, and  $2000\ \mu\text{s}$  and 20 times, respectively. Table 5.1 gives the results of nine separate experimental data sets. The measured values of the inner diameter and grooved width approach to  $1000\ \mu\text{m}$  and  $100\ \mu\text{m}$  for the original design, respectively. The current study controls the laser-machined accuracy to fabricate rough patterned templates. The groove boundary after laser micro-machining is clearly observed in Fig. 5.16. The residual micro-chips are spread around the groove and seen by SEM. The SEM result is shown in Fig. 5.17. Two local heat affected zones (HAZ) underneath the laser beam focal position of the glass are marked in Fig. 5.17. The width of HAZ increases with penetrating depth.



Table 5.1 Machining parameters of the annular groove and measured results.

| Number of experiments | Machining parameters    |  | Measured values                   |                       |
|-----------------------|-------------------------|--|-----------------------------------|-----------------------|
|                       | Number of passes, $N_p$ | Single-shot laser exposure time, $T_s$ ( $\mu\text{s}$ ) | $\varnothing_i$ ( $\mu\text{m}$ ) | $w$ ( $\mu\text{m}$ ) |
| 1                     | 20                      | 2000   | 1086.38                           | 110.75                |
| 2                     | 20                      | 2500   | 1089.70                           | 156.53                |
| 3                     | 20                      | 3000   | 1116.28                           | 129.00                |
| 4                     | 22.5                    | 2000   | 1076.41                           | 126.25                |
| 5                     | 22.5                    | 2500   | 1099.67                           | 178.02                |
| 6                     | 22.5                    | 3000   | 1089.70                           | 136.98                |
| 7                     | 25                      | 2000   | 1119.38                           | 138.93                |
| 8                     | 25                      | 2500   | 1076.20                           | 119.07                |
| 9                     | 25                      | 3000   | 1073.09                           | 144.79                |

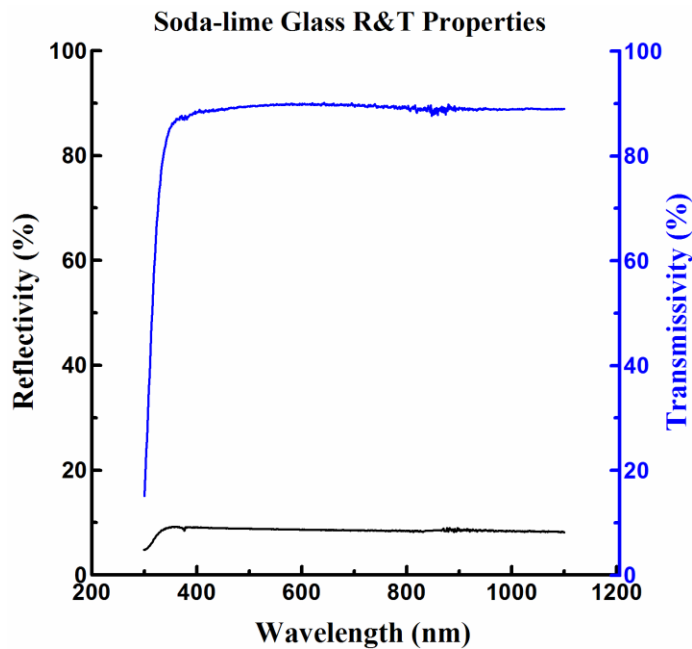


Figure 5.15 Optical characteristics of soda-lime glass substrate.

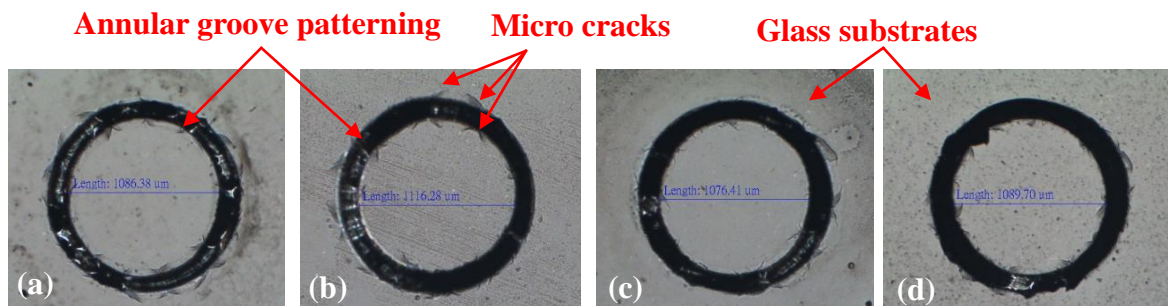


Figure 5.16 Optical microscope pictures of the annular groove fabricated by various  $T_s$  and  $N_p$ : (a) 2000  $\mu\text{s}$ , 20 times, (b) 3000  $\mu\text{s}$ , 20 times, (c) 2000  $\mu\text{s}$ , 22.5 times, (d) 3000  $\mu\text{s}$ , 22.5

times.

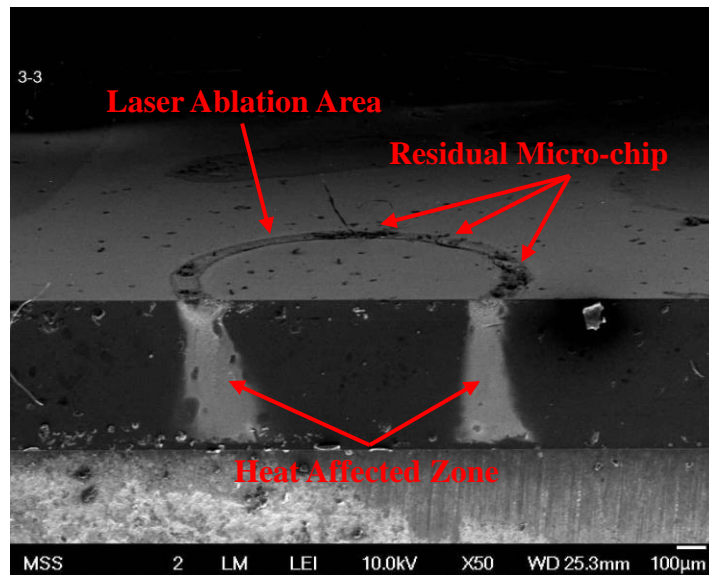


Figure 5.17 A SEM planar and cross-section image of rough patterned template fabricated by  $T_s = 3000 \mu\text{s}$  and  $N_p = 20$  times.

### 5.3.2 Surface profiles of machined templates

The surface profiles of a crater produced by a LBW process and LIPAA technique with laser machined parameters of  $T_s = 2000 \mu\text{s}$  and  $N_p = 22.5$  times is analyzed using a Talyscan 150 profilometer, shown in Fig. 5.18. Meanwhile, Fig. 5.18 shows the measured surface profile of a single sided groove. Based on the morphological observations of craters, the average crater height surrounding the annular groove is raised  $12 \mu\text{m}$  above the glass substrate surface. Furthermore, the average crater depth surrounding the annular groove is  $3 \mu\text{m}$  below the glass substrate surface. Figure 5.19 plots the crater height and depth via the three different  $T_s$ . Figure 5.19(a) shows the relationship between crater height versus  $T_s$  and  $N_p$ . The crater height gradually increases with increasing  $T_s$  and  $N_p$ . Figure 5.19(b) graphs the crater depth versus  $N_p$  and three different  $T_s$ . The crater depth increases immediately with the increase of the  $T_s$  and  $N_p$ . Simultaneously, crater depth generated by  $2000 \mu\text{s}$  is extremely shallower than that generated by  $2500 \mu\text{s}$  or  $3000 \mu\text{s}$ .

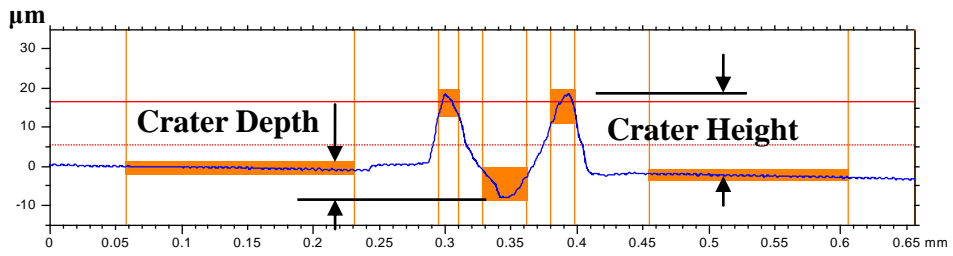


Figure 5.18 A single sided profile of annular groove fabricated by  $T_s = 2000 \mu\text{s}$  and  $N_p = 22.5$  times.

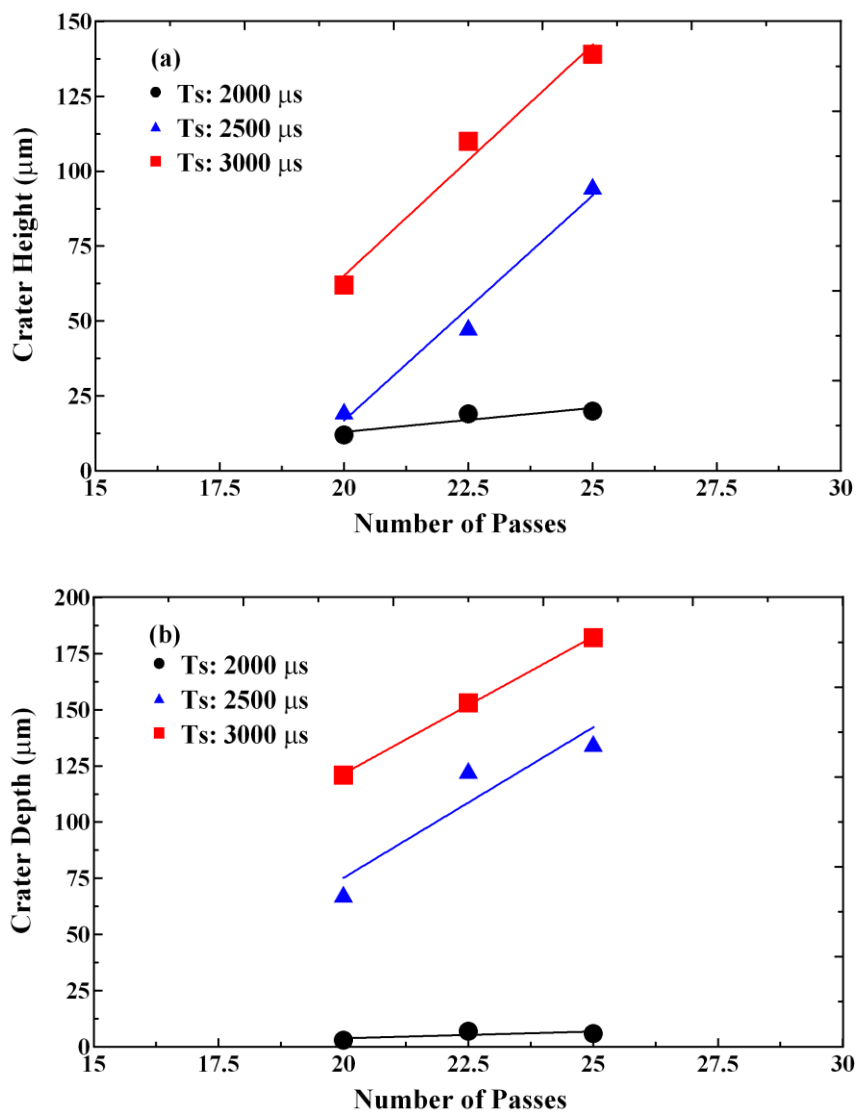


Figure 5.19 Plots of the crater height and depth via the three different  $T_s$ . (a) Crater height versus  $T_s$  and  $N_p$ , (b) crater depth versus  $T_s$  and  $N_p$ .

### 5.3.3 Contact angle of water droplets on the hydrophobic template

Figure 5.20 shows the SEM cross-section view of a planar glass substrate coated with Teflon thin film. The thickness of Teflon thin film is 695 nm. A water droplet is deposited onto the template and condenses into a planar-convex droplet to minimize droplet energy. A camera captures the cross-section profile of the droplet on the template, to determine the contact angle. The typical measured contact angle on a glass substrate coated with Teflon is  $118.6^\circ$ . This contact angle is measured the included angle between liquid-solid and liquid-vapour interfaces. Using the same approach, the different micro-droplet volumes of water are deposited onto a rough annular-grooved template coated with Teflon and measured the resulting contact angle. The groove contour can confine the water quantity and result in increasing contact angle. Figure 5.21 shows the typical result. The measured contact angle ranges from  $119.9^\circ$  to  $131.3^\circ$  when the droplet volumes increase from  $1.1 \mu\text{L}$  to  $9 \mu\text{L}$ . The maximum angle of  $131.3^\circ$  is achieved on the groove as  $2.9 \mu\text{L}$  of water is added. As added volume of water is more than  $2.9 \mu\text{L}$ , the droplet overflows the constraint. The rough annular-grooved template can accumulate more liquid and obtain a larger contact angle compared to the planar glass substrate coated with Teflon.

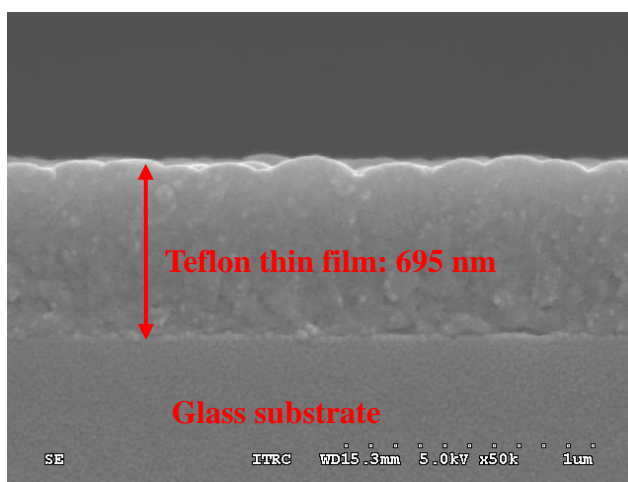


Figure 5.20 A SEM cross-section photograph of a planar glass substrate coated with Teflon thin film.

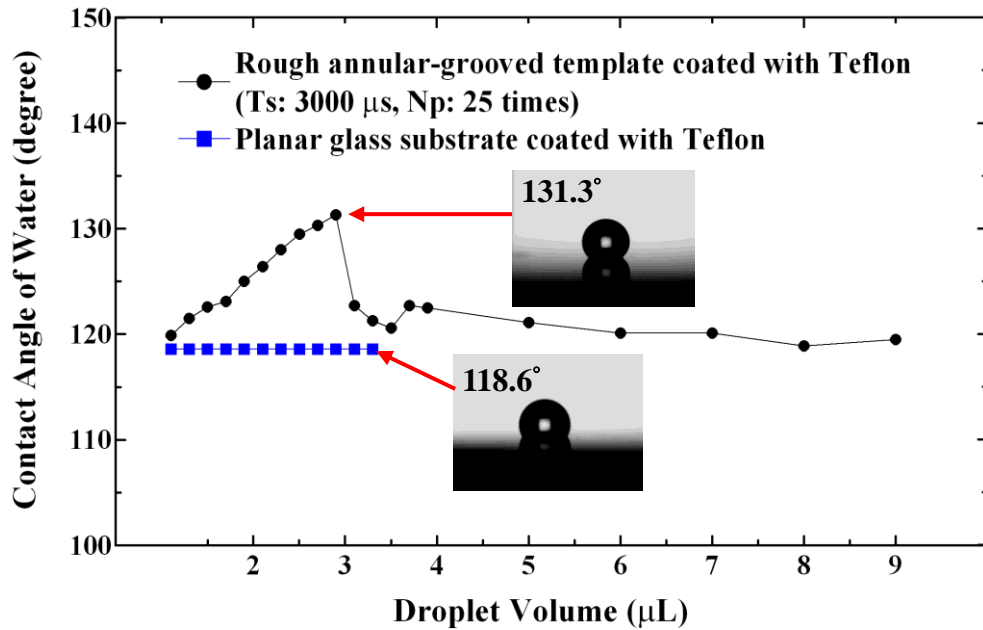


Figure 5.21 The contact angle versus droplet volume relation between the annular-grooved and planar templates coated with thin Teflon.

### 5.3.4 Summary

This work presented laser-induced backside writing (LIBW) processes and laser-induced plasma assisted ablation (LIPAA) techniques on a soda-lime glass substrate via metal target ablation to fabricate rough round patterned templates. The measured results showed that crater height and depth gradually increased with increasing number of passes and single-shot laser exposure time. After a 695 nm thick Teflon thin film was deposited on the glass plate, the micro-machined template surface became hydrophobic. The typical measured contact angle on a planar glass substrate coated with Teflon was 118.6°. The contact angle increased to 131.3° when the water drop was added on a round annular-grooved template coated with Teflon. The maximum volume of water to hold the contact angle was about 2.9 μL. The formed water drop flowed out of the constrained groove when the water volume was more than 2.9 μL. Therefore, the shape and contact angle of the water drops could be adjusted through the water volume and surface morphology of the micro-machined surface.

## 5.4 Characteristics of Ni-Ir and Pt-Ir hard coatings surface treated by pulsed Nd:YAG laser irradiation

### 5.4.1 SEM observations on different composition alloy films

Figure 5.22 shows the cross-section images of Pt-Ir and Ni-Ir alloy films deposited on a silicon substrate taken by a scanning electron microscope (SEM). Figure 5.22 (a) shows that the film layer of Ir-50 at.% Ni alloy was approximately 300 nm thick while the Cr buffer layer was approximately 58 nm thick. Figure 5.22 (b) shows that the film layers of Ir-50 at.% Pt alloy and Cr were approximately 306 nm and 51 nm thick, respectively. The clear and typical column crystallines of Pt-Ir and Ni-Ir coatings grown from the chromium buffer layer deposited on a silicon substrate are observed by SEM.

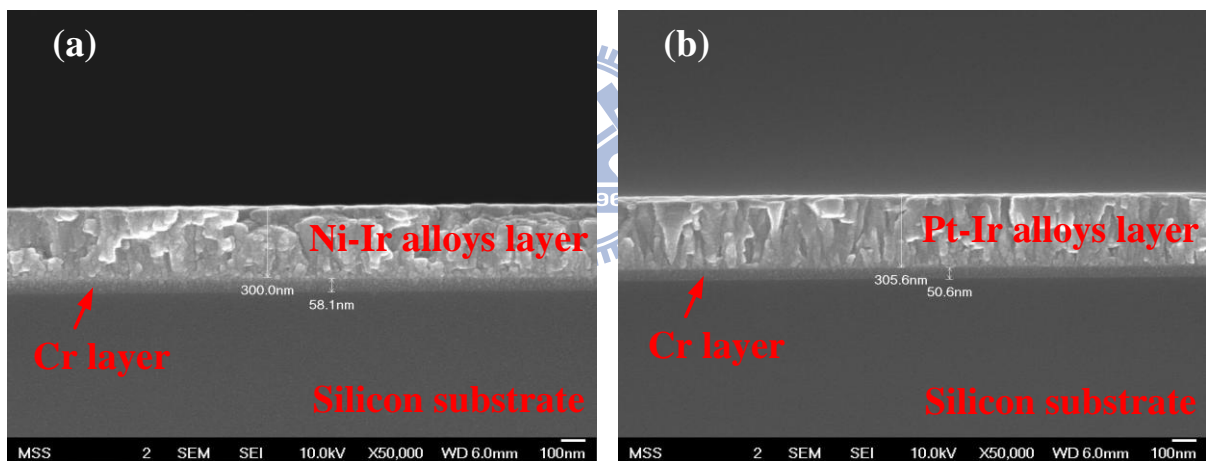


Figure 5.22 Cross-section views of Ni-Ir and Pt-Ir films deposited on silicon substrates observed by SEM. (a) Ir-50 at.% Ni, (b) Ir-50 at.% Pt.

### 5.4.2 The temperature distribution profile of the different composition alloy films

First, spectrophotometry (Lambda 900) is used to determine the reflectance (R) of the WC substrate with different Ir-based alloy coatings. Figure 5.23 shows the reflectance spectra of different Pt-Ir and Ni-Ir alloy composition films. These results show that reflectivity in the Nd:YAG laser infrared spectrum (wavelength@1064 nm) is from 76% to 81% . Because the

thin films were not transparent for the Nd:YAG laser wavelength, the absorptance (A) is calculated to be from 24% to 19% by substituting reflectance values into  $A=1-(R+T)$ .

Figure 5.24 displays a cross-section view of the temperature distribution on the WC substrate with Ir-25 at.% Ni coating after a 100  $\mu$ s single-pulse exposure time, a pulse repetition frequency of 100 kHz and a laser output power level of 5.2W. The initial temperature of irradiation was 27°C and the maximum heating temperature was controlled at approximately 1500°C. A series of the laser output power levels were calculated by ANSYS software to be 5.2W, 5.13W, 4.55W, 5.07W, 5.76W and 5.58W for Ir-25 at.% Ni, Ir-50 at.% Ni, Ir-75 at.% Ni, Ir-25 at.% Pt, Ir-50 at.% Pt, and Ir-75 at.% Pt, respectively. Hence, the processing parameter values of laser treatment calculated by ANSYS simulation are summarized in Table 5.2.

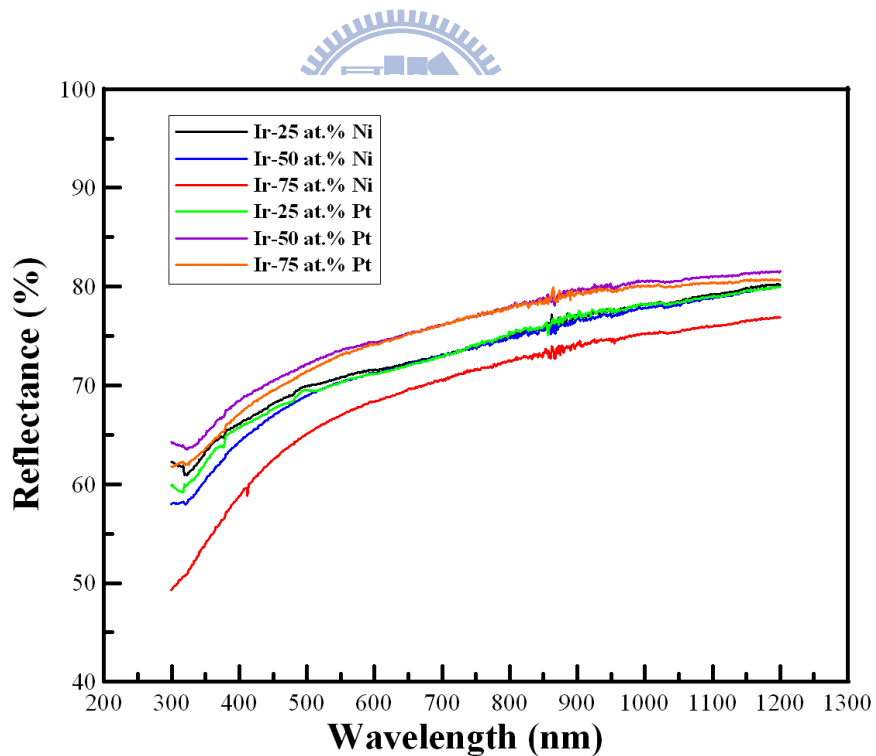


Figure 5.23 Optical reflectance versus wavelength for different composition alloys.

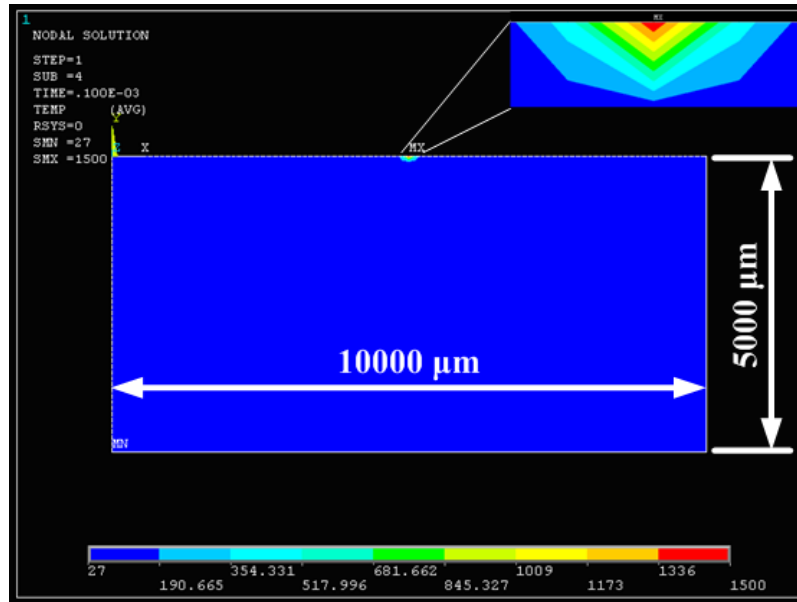


Figure 5.24 A cross-section view of temperature distribution on WC mold with Ir-25 at.% Ni coating calculated by ANSYS simulation.

Table 5.2 Summarized table of processing parameters for laser treatment.

| Compositions  | Absorptance<br>@1064 nm | Single-pulse<br>exposure time<br>( $\mu$ s) | Pulse repetition<br>frequency (kHz) | Laser<br>power<br>(W) | Treatment<br>temperature ( $^{\circ}$ C) |
|---------------|-------------------------|---|-------------------------------------|-----------------------|--|
| Ir-25 at.% Ni | 21.28                   |   |                                     | 5.2                   | 1500                                     |
| Ir-50 at.% Ni | 21.59                   |   |                                     | 5.13                  | 1501                                     |
| Ir-75 at.% Ni | 24.33                   | 100   | 100                                 | 4.55                  | 1501                                     |
| Ir-25 at.% Pt | 21.38                   |   |                                     | 5.07                  | 1500                                     |
| Ir-50 at.% Pt | 19.21                   |   |                                     | 5.76                  | 1500                                     |
| Ir-75 at.% Pt | 19.82                   |   |                                     | 5.58                  | 1499                                     |

### 5.4.3 Description of surface roughness of Pt-Ir and Ni-Ir films treated by laser annealing

All Pt-Ir and Ni-Ir thin films were deposited on WC molds by ion source assisted magnetron sputtering. Because the overlapping area of the sequential laser spot is over 99% during the laser treatment on these films, and we apply laser treatment on the whole film which is 10 mm diameter side. The AFM was used to measure the film surface roughness in



the middle film surface. Table 5.3 shows the surface roughness of different alloy compositions before and after the laser treatments. Before the laser treatment, the surface roughness values  $R_a$  are ranged from 34.26 nm to 12.5 nm with a measuring region of  $10 \times 10 \mu\text{m}^2$ . The roughness increases dramatically up to 1-order high after the laser treatments. The geometric surface features of films after laser treatments are summarized in Fig. 5.25. Figure 5.25 shows the surface roughness after laser treatment, clearly showing that the surface roughness increases over 100 nm. Moreover, the values of surface roughness are obviously increased as increasing concentrations of Pt or Ni. This trend is similar to the results reported in the glass-molding machine annealing on Pt-Ir and Ni-Ir coatings [56]. Furthermore, a comparison of different Ni-Ir alloy compositions verses laser output power of treatment parameters indicates that higher film surface absorption produced greater surface roughness.

Table 5.3 Comparison of surface roughness before and after laser treatment.

| Compositions  | Surface roughness (nm) |                       |
|---------------|------------------------|-----------------------|
|               | Before laser treatment | After laser treatment |
| Ir-25 at.% Ni | 12.50                  | 137.71                |
| Ir-50 at.% Ni | 17.21                  | 154.14                |
| Ir-75 at.% Ni | 34.26                  | 189.09                |
| Ir-25 at.% Pt | 12.52                  | 117.24                |
| Ir-50 at.% Pt | 14.92                  | 157.09                |
| Ir-75 at.% Pt | 17.90                  | 178.00                |

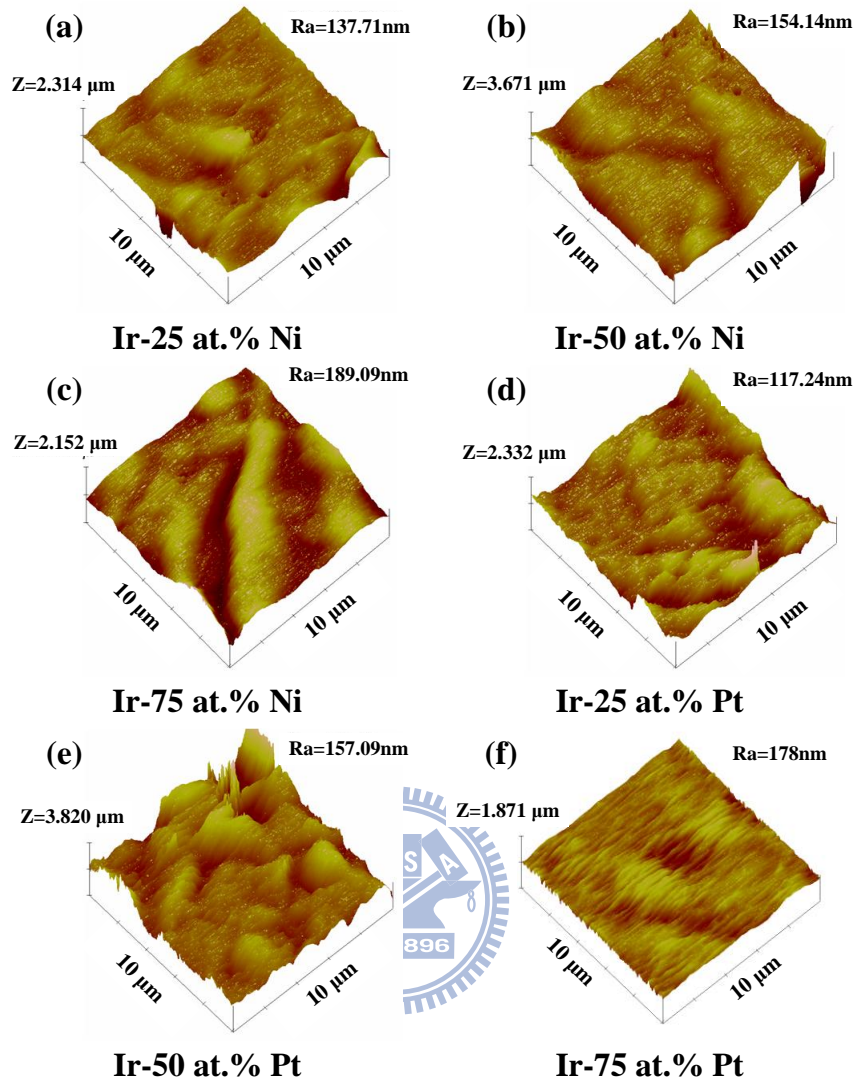


Figure 5.25 Surface roughness of different alloy coatings after laser surface treatment. The coatings composition are (a) Ir-25 at.% Ni, (b) Ir-50 at.% Ni, (c) Ir-75 at.% Ni, (d) Ir-25 at.% Pt, (e) Ir-50 at.% Pt and (f) Ir-75 at.% Pt.

#### 5.4.4 Oxidation analysis using EDS

The oxide effect on the surface roughness is examined because the surface roughness is an important parameter in the glass-molding process and the rough surface is resulted from oxide. In this research, the laser surface treatment of Pt-Ir and Ni-Ir alloys was conducted at room temperature without protection during laser irradiation. Figure 5.26 shows the oxygen concentrations of Ir-based alloys measured by EDS after laser treatment. The oxygen

concentration of Pt-Ir coatings is lower than that of Ni-Ir coatings, and the difference is approximately 3 to 5 at.% O. Moreover, the oxygen concentration of these alloys increases obviously with increasing Pt or Ni doping. For Ir-75 at.% Ni coatings, in particular, the deposited film was seriously oxidized and the roughness Ra value is the largest one among all Ir-based coatings subjected to the oxidation testing. Due to the serious oxidation, the thin film that contained 75 at.% Ni is unusable to be a protective coating applied on glass-molding dies. To investigate the anti-oxidation behaviour, these thin films are annealed at 700°C under a nitrogen gas atmosphere using a glass-molding machine conducted by Tseng et al. [56]. However, the oxygen concentration of these films is greatly increased because the operation environment of this laser treatment is at the 1500°C elevated temperature in the air and not filled with protective gas.

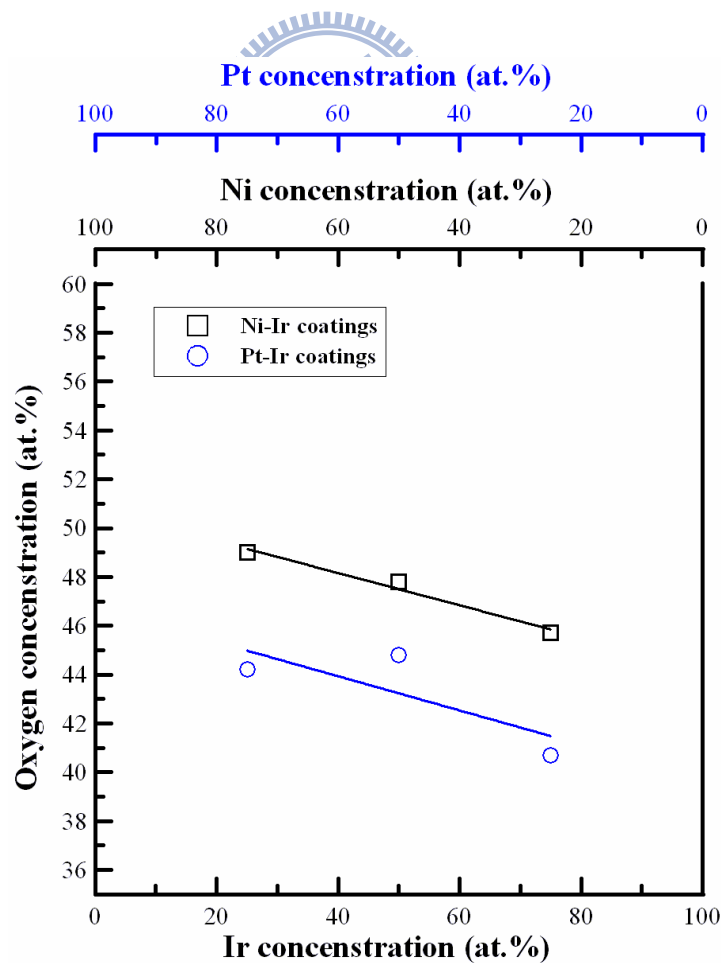


Figure 5.26 Oxygen concentration of Pt-Ir and Ni-Ir coatings after laser surface treatment.

#### 5.4.5 Microhardness and reduced modulus property

Figures 5.27 and 5.28 show the microhardness and reduced modulus test results measured by the nanoindentation instrument, respectively. The microhardness and reduced modulus measurement procedure is introduced and each process including loading, holding, and unloading takes 5 s. An indentation depth of  $30 \text{ nm} \pm 10\%$  and a maximal loading of  $50 \text{ }\mu\text{N}$  were adopted in this study. The average values with the standard deviation measured from five spots on each specimen were illustrated. After laser surface treatment at  $1500^\circ\text{C}$ , the microhardness values of Ni-Ir and Pt-Ir coatings increased from 0.4812 to 0.824 GPa and from 0.79 to 1.5 GPa with decreasing concentrations of Ni and Pt, respectively. All the microhardness values of laser treated films are lower than the original ones. In addition, the reduced modulus values decreased from 31.89 to 15.02 GPa as the Pt concentrations decreased. Moreover, the Ir-25 at.% Ni of reduced modulus had a minimum value of 15.91 GPa. Due to the oxidation reaction between alloy materials and oxygen [92,93], these tested values of microhardness and reduced modulus of laser treated coatings apparently decreased than the un-treated ones.

#### 5.4.6 Summary

The subjects of this study were to develop a laser surface treatment technology for the protective coatings of glass-molding dies and to better understand the interaction between laser beam and materials coated on the die surface. After laser surface treatment at  $1500^\circ\text{C}$ , the values of surface roughness were obviously increased as increasing concentrations of Pt or Ni. Moreover, the anti-oxide ability of Pt-Ir thin films had been validated to be better than Ni-Ir thin films. The Pt-Ir and Ni-Ir coatings were unable to withstand the working temperature over  $1500^\circ\text{C}$ , which was considered for quartz molding process and hot embossing process. The surface films were high roughness, low microhardness and low reduced modulus because of the film oxidation that occurred in a high working temperature

process. Therefore, these Ir-alloy coatings operated under the vacuum environment and filled with protective gas were useful in glass molding to avoid the severe surface oxidation and to reduce surface roughness.

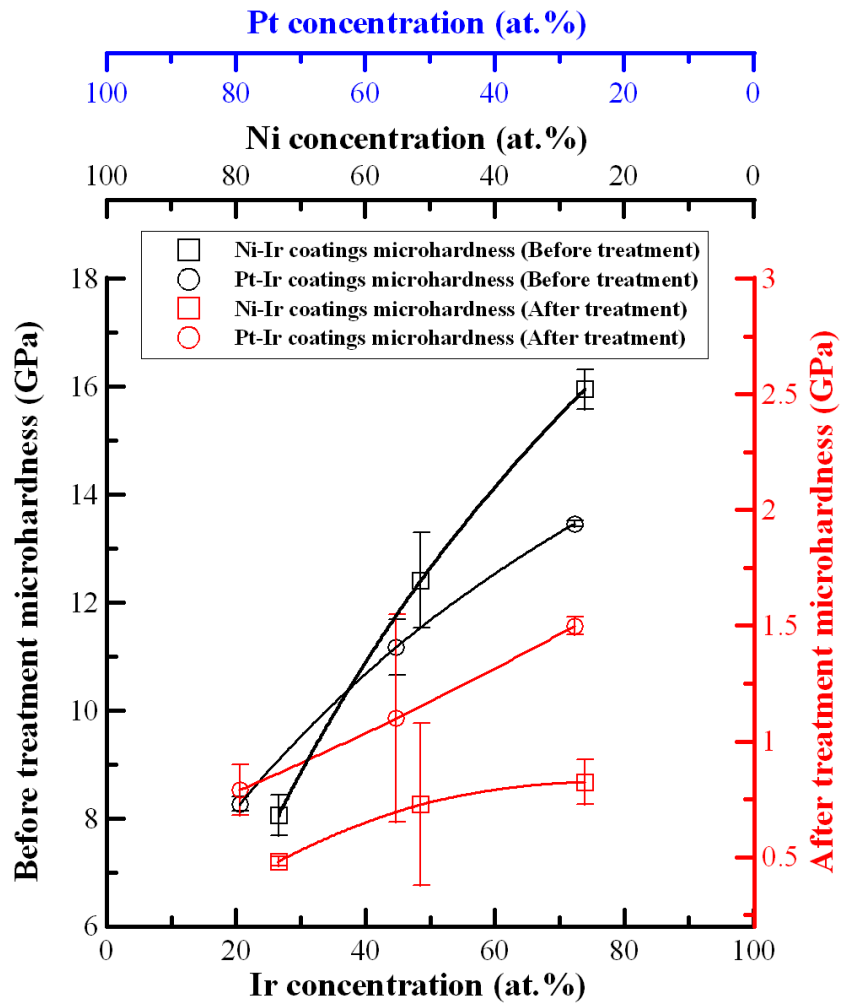


Figure 5.27 Plot of microhardness testing under different compositions of Pt-Ir and Ni-Ir coatings.

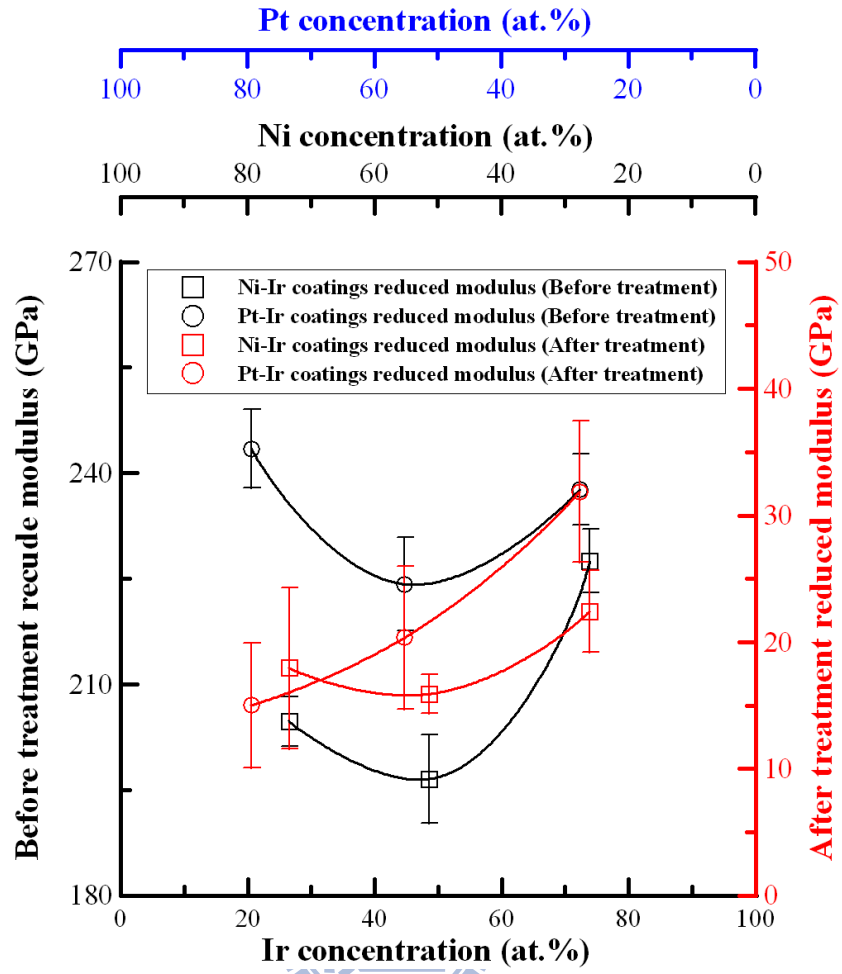


Figure 5.28 Plot of reduced modulus testing under different contents of Pt-Ir and Ni-Ir coatings.

## Chapter 6 Conclusions and future work

### 6.1 Conclusions

The purposes of this dissertation aim to develop the surface processing techniques on materials used for the optoelectric applications by the nanosecond pulsed Nd:YAG laser system and to better understand the interaction between laser beam and materials. From the research on the electrode isolation of touch panel applications, the Nd:YAG laser with the optimal average laser power of 2.2 W was used to scribe the indium tin oxide (ITO) thin films deposited on three kinds of substrate materials, i.e. soda-lime glass, polycarbonate (PC), and cyclic-olefin-copolymer (COC) materials. The following conclusions were obtained:

- (1) After the laser scribing process, the residual ITO thin film was produced on the scribed path with the laser exposure times from 10  $\mu\text{s}$  to 20  $\mu\text{s}$ .
- (2) The better edge qualities of the scribed lines could obtain when the exposure time extended from 30  $\mu\text{s}$  to 60  $\mu\text{s}$ .
- (3) When the laser exposure time was longer than 60  $\mu\text{s}$ , the partially burned areas of the scribed thin films on PC and COC substrates were observed.
- (4) The isolated line width and resistivity values increased when the laser exposure time increased.
- (5) All resistivity values after laser scribing were greater than the original resistivity.

The following conclusions are drawn from pattern creation on silicon substrate by pulsed Nd:YAG laser using the surface texturing technique :

- (1) Increasing the laser fluence and laser pulse duration pushed more molten slag piled around the ablated trenches to create micro-sized craters and led to higher crater height and surface roughness.
- (2) The droplet spread very quickly on a laser textured surface and almost disappeared within 0.5167 s, compared to that with a contact angle of  $47.9^\circ$  on an untextured surface.

- (3) This processing technique can also be used to fabricate silicon based solar cells to increase the absorption efficiency of light.

The pulsed Nd:YAG laser fabricated rough array-patterns on a soda-lime glass plate by the laser-induced backside writing (LIBW) process and the laser-induced plasma assisted ablation (LIPAA) technique. The following conclusions were obtained:

- (1) The crater height and depth gradually increased with increasing number of passes and single-shot laser exposure time.
- (2) The micro-machined template surface became hydrophobic after a 695 nm thick Teflon thin film was deposited on the glass plate.
- (3) The typical measured contact angle on a planar glass substrate coated with a Teflon film was 118.6°.
- (4) The contact angle increased to 131.3° when the water drop was poured in a round annular-grooved template coated with a Teflon film.
- (5) This processing technique can also be used to manufacture hemispherical drug-loaded particles.

In the Nd:YAG laser surface treatment technology for the protective coatings on the glass-molding dies, one can draw the following obvious conclusions:

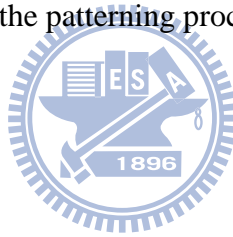
- (1) The Pt-Ir and Ni-Ir film coatings were unable to withstand the working temperatures over 1500°C, which was considered for quartz molding and hot embossing process.
- (2) The films showed high roughness, low microhardness and low reduced modulus because of the film oxidation occurred in high working temperature process.
- (3) These Ir-alloy coatings operated under the vacuum environment and filled with protective gas were effective in glass molding to avoid the severe surface oxidation and to reduce surface roughness.



## 6.2 Future work

The suggestions of future studies are summarized as follows:

- (1) The laser scribing technique can apply in the edge isolation of silicon (Si) solar panels and in the isolated line of thin-film solar cells to prevent the electrical contact.
- (2) The laser texturing technique can fabricate microstructures in Si solar panels to increase the absorption efficiency of light.
- (3) The laser-induced backside writing (LIBW) processes and laser-induced plasma assisted ablation (LIPAA) techniques can apply for uniform lens array formation.
- (4) The laser treatment technology can apply for cleaning material surface to remove contaminants, oxides, and paints without damaging the substrate.
- (5) The laser direct writing also can apply in the annealing process of transparent conductive oxide (TCO) thin films and in the patterning process of light guiding plates.



## References

- [1] <http://www.cmxr.com/Industrial/Handbook/Chapter3.htm>
- [2] <http://www.cmxr.com/Industrial/Handbook/Chapter5.htm>
- [3] B.G. Lewis, D.C. Paine, Applications and processing of transparent conducting oxides, MRS Bull. 25 (2000), pp.22-27.
- [4] L. Zhao, Y.H. Zuo, C.L. Zhou, H.L. Li, H.W. Diao, W.J. Wang, A highly efficient light-trapping structure for thin-film silicon solar cells, Sol. Energy 84 (2010), pp.110-115.
- [5] F.F. Ngaffo, A.P. Caricato, M. Fernandez, M. Martino, F. Romano, Structural properties of single and multilayer ITO and TiO<sub>2</sub> films deposited by reactive pulsed laser ablation deposition technique, Appl. Surf. Sci. 253 (2007), pp.6508-6511.
- [6] S. Venkat, C. Dunskey, Laser patterning of ITO in flat panel display manufacturing, Proc. SPIE Int. Soc. Opt. Eng. 6106 (2006), pp.610602.1- 610602.7.
- [7] T. Minami, Present status of transparent conducting oxide thin-film development for Indium-Tin-Oxide (ITO) substitutes, Thin Solid Films 516 (2008), pp.5822-5828.
- [8] V.L. Calil, C. Legnani, G.F. Moreira, C. Vilani, K.C. Teixeira, W.G. Quirino, R. Machado, C.A. Achete, M. Cremona, Transparent thermally stable poly(etherimide) film as flexible substrate for OLEDs, Thin Solid Films 518 (2009), pp.1419-1423.
- [9] <http://duniaebook.wordpress.com/2010/04/05/elonex-ebook-reader-by-borders-uk/>
- [10] <http://fwd.five.tv/gadgets/phones/apple-iphone-3g-s>
- [11] [http://www.hanwhananotech.com/WebContent/cnt/cnt\\_app1\\_idx.jsp](http://www.hanwhananotech.com/WebContent/cnt/cnt_app1_idx.jsp)
- [12] O.A. Ghandour, D. Constantinide, R. Sheets, Excimer ablation of ITO on flexible substrates for large format display application, Proc. SPIE Int. Soc. Opt. Eng. 4637 (2002), pp.90-101.
- [13] <http://en.wikipedia.org/wiki/Wetting>

- [14] S. Shibuichi, T. Onda, N. Satoh, K. Tsujii, Super water-repellent surfaces resulting from fractal structure, *J. Phys. Chem.* 100 (1996), pp.19512-19517.
- [15] H.Y. Erbil, A.L. Demirel, Y. Avci, O. Mert, Transformation of a simple plastic into a superhydrophobic surface, *Science* 299 (2003), pp.1377-1380.
- [16] R.N. Wenzel, Resistance of solid surfaces to wetting by water, *J. Ind. Eng. Chem.* 28 (1936), pp.988-994.
- [17] M. Miwa, A. Nakajima, A. Fujishima, K. Hashimoto, T. Watanabe, Effects of the surface roughness on sliding angles of water droplets on superhydrophobic surfaces, *Langmuir* 16 (2000), pp.5754-5760.
- [18] Z. Yoshimitsu, A. Nakajima, T. Watanabe, K. Hashimoto, Effects of surface structure on the hydrophobicity and sliding behavior of water droplets, *Langmuir* 18 (2002), pp.5818-5822.
- [19] C. Neinhuis, W. Barthlott, Characterization and distribution of water-repellent, self-cleaning plant surfaces, *Ann. Bot.* 79 (1997), pp.667-677.
- [20] R. Bolssey, Self-cleaning surfaces - virtual realities, *Nat. Mater.* 2 (2003), pp.301-306.
- [21] O. Bossart, G. Calzaferri, Selfassembly of zeolite L crystals on biological self-cleaning surfaces, *Microporous Mesoporous Mater.* 109 (2008), pp.392-397.
- [22] [http://www.narl.org.tw/tw/topic/topic.php?topic\\_id=67](http://www.narl.org.tw/tw/topic/topic.php?topic_id=67)
- [23] <http://www.itrc.org.tw/Publication/Newsletter/no91/p08.php>
- [24] TOSHIBA MACHINE CO., LTD, <http://www.toshiba-machine.co.jp/>
- [25] C.M. Dunskey, Laser material processing in microelectronics manufacturing: status and near-term opportunities, *Proceeding of SPIE* 5713 (2005), pp.200-214.
- [26] H. Yoo, H. Shin, M. Lee, Direct patterning of double-layered metal thin films by a pulsed Nd:YAG laser beam, *Thin Solid Films* 518 (2010), pp.2775-2778.
- [27] J. Chae, L. Jang, K. Jain, High-resolution, resistless patterning of indium-tin-oxide thin films using excimer laser projection annealing process, *Mater. Lett.* 64 (2010),

pp.948-950.

- [28] A. Solieman, A.H. Moharram, M.A. Aegerter, Patterning of nanoparticulate transparent conductive ITO films using UV light irradiation and UV laser beam writing, *Appl. Surf. Sci.* 256 (2010), pp.1925-1929.
- [29] H. Shin, B. Sim, M. Lee, Laser-driven high-resolution patterning of indium tin oxide thin film for electronic device, *Opt. Lasers Eng.* 48 (2010), pp.816-820.
- [30] O. Yavas, M. Takai, High-speed maskless laser patterning of indium tin oxide thin films, *Appl. Phys. Lett.* 73 (1998), pp.2558-2560.
- [31] O. Yavas, M. Takai, Effect of substrate absorption on the efficiency of laser patterning of indium tin oxide thin films, *J. Appl. Phys.* 85 (1999), pp.4207-4212.
- [32] J.G. Lunney, R.R. O'Neill, K. Schulmeister, Excimer laser etching of transparent conducting oxides, *Appl. Phys. Lett.* 59 (1991), pp.647-649.
- [33] C. Molpeceres, S. Lauzurica, J.L. Ocaña, J.J. Gandía, L. Urbina, J. Cárabe, Microprocessing of ITO and a-Si thin films using ns laser sources, *J. Micromech. Microeng.* 15 (2005), pp.1271-1278.
- [34] M. Park, B.H. Chon, H.S. Kim, S.J. Jeoung, D. Kim, J.I. Lee, H.Y. Chu, H.R. Kim, Ultrafast laser ablation of indium tin oxide thin films for organic light-emitting diode application, *Opt. Lasers Eng.* 44 (2006), pp.138-146.
- [35] M.F. Chen, Y.P. Chen, W.T. Hsiao, Z.P. Gu, Laser direct write patterning technique of indium tin oxide film, *Thin Solid Films* 515 (2007), pp.8515-8518.
- [36] M.F. Chen, W.T. Hsiao, Y.S. Ho, S.F. Tseng, Y.P. Chen, Laser patterning with beam shaping on indium tin oxide thin films of glass/plastic substrate, *Thin Solid Films* 518 (2009), pp.1072-1078.
- [37] Q. Qiao, K. Ma, Y.Q. Wang, G.C. Zhang, Z.R. Shi, G.H. Li, Optimization of laser patterning of textured gallium-doped zinc oxide for amorphous silicon photovoltaics, *Appl. Surf. Sci.* 256 (2010), pp.4656-4660.

- [38] H.J. Kim, M.S. Lee, D.G. Lee, M.K. Son, K.J. Lee, Optimal ablation of fluorine-doped tin oxide (FTO) thin film layers adopting a simple pulsed Nd:YAG laser with TEM<sub>00</sub> mode, *Opt. Lasers Eng.* 47 (2009), pp.558-562.
- [39] S. Haas, G. Schöpe, C. Zahren, H. Stiebig, Analysis of the laser ablation processes for thin-film silicon solar cells, *Appl. Phys. A* 92 (2008), pp.755-759.
- [40] R. Kannan, D. Sivakumar, Drop impact process on a hydrophobic grooved surface, *Colloids Surf., A* 317 (2008), pp.694-704.
- [41] K. Callewaert, Y. Martelé, L. Breban, K. Naessens, P. Vandaele, R. Baets, G. Geuskens, E. Schacht, Excimer laser induced patterning of polymeric surfaces, *Appl. Surf. Sci.* 208-209 (2003), pp.218-225.
- [42] H.Y. Kwong, M.H. Wong, Y.W. Wong, K.H. Wong, Superhydrophobicity of polytetrafluoroethylene thin film fabricated by pulsed laser deposition, *Appl. Surf. Sci.* 253 (2007), pp.8841-8845.
- [43] S.F. Tseng, W.T. Hsiao, M.F. Chen, K.C. Huang, S.Y. Hsiao, Y.S. Lin, C.P. Chou, Surface wettability of silicon substrates enhanced by laser ablation, *Appl. Phys. A* 101 (2010), pp.303-308.
- [44] X. Hou, F. Zhou, B. Yu, W. Liu, Superhydrophobic zinc oxide surface by differential etching and hydrophobic modification, *Mater. Sci. Eng., A* 452-453 (2007), pp.732-736.
- [45] L.P. Lee, S.A. Berger, D. Liepmann, L. Pruitt, High aspect ratio polymer microstructures and cantilevers for bioMEMS using low energy ion beam and photolithography, *Sens. Actuators, A* 71 (1998), pp.144-149.
- [46] J. Lee, B. He, N.A. Patankar, A roughness-based wettability switching membrane device for hydrophobic surfaces, *J. Micromech. Microeng.* 15 (2005), pp.591-600.
- [47] J.H. Chen, J.T. Yang, C.S. Yu, Y.C. Hu, Droplet manipulation on hydrophobic textured surfaces with roughened patterns, *In: Proceedings of HT-FED 2004, 2004 ASME Heat Transfer/Fluids Engineering Summer Conference*, Charlotte, North Carolina, USA, July

11-15, 2004, pp.1-8.

- [48] M. R. Kim, S.Y. Heo, D.J. Jang, Nanopattern transfer and wettability modification of regularly structured metallic and polymeric surfaces with replication, *J. Colloid Interface Sci.* 339 (2009), pp.217-221.
- [49] N.B. Dahotre, S.R. Paital, A.N. Samant, C. Daniel, Wetting behavior of laser synthetic surface micro textures on Ti-6Al-4V for bioapplication, *Phil. Trans. R. Soc. A* 368 (2010), pp.1863-1889.
- [50] A. Stojanovic, G.R.J. Artus, S. Seeger, Micropatterning of superhydrophobic silicone nanofilaments by a near-ultraviolet Nd:YAG laser, *Nano Res.* 3 (2010), pp.889-894.
- [51] V. Oliveira, B. Nunes, R. Vilar, Wetting response of KrF laser ablated polyimide surfaces, *Nucl. Instrum. Methods Phys. Res., Sect. B* 268 (2010), pp.1626-1630.
- [52] B.H. Luo, P.W. Shum, K.Y. Li, Preparation of hydrophobic surface on steel by patterning using laser ablation process, *Surf. Coat. Technol.* 204 (2010), pp.1180-1185.
- [53] J. Bekesi, J.J.J. Kaakkunen, W. Michaeli, F. Klaiber, M. Schoengart, J. Ihlemann, P. Simon, Fast fabrication of super-hydrophobic surfaces on polypropylene by replication of short-pulse laser structured molds, *Appl. Phys. A* 99 (2010), pp.691-695.
- [54] J. Noh, J.H. Lee, S. Na, H. Lim, D.H. Jung, Fabrication of hierarchically micro- and nano-structured mold surfaces using laser ablation for mass production of superhydrophobic surfaces, *Jpn. J. Appl. Phys.* 49 (2010), pp.106502.
- [55] M. Tang, M.H. Hong, Y.S. Choo, Z. Tang, D.H.C. Chua, Super-hydrophobic transparent surface by femtosecond laser micro-patterned catalyst thin film for carbon nanotube cluster growth, *Appl. Phys. A* 101 (2010), pp.503-508.
- [56] S.F. Tseng, C.T. Lee, K.C. Huang, D. Chiang, C.Y. Huang, C.P. Chou, Mechanical properties of Pt-Ir and Ni-Ir binary alloys for glass-molding dies coating, *J. Nanosci. Nanotechnol.* 11 (2011). (In Press, DOI: 10.1166/jnn.2011.3502)
- [57] C.H. Lin, J.G. Duh, B.S. Yau, Processing of chromium tungsten nitride hard coatings for

- glass molding, *Surf. Coat. Technol.* 201 (2006), pp.1316-1322.
- [58] L.C. Chang, Y.I. Chen, J.W. Lee, H.Y. Lin, Y.C. Kuo, C.J. Wang, Detaching mechanism for Mo–Ru hard coating on tungsten carbide, *Surf. Coat. Technol.* 202 (2007), pp.967-972.
- [59] Y.I. Chen, L.C. Chang, J.W. Lee, C.H. Lin, Annealing and oxidation study of Mo–Ru hard coatings on tungsten carbide, *Thin Solid Films* 518 (2009), pp.194-200.
- [60] C.T. Wei, H.P. D. Shieh, Effects of processing variables on tantalum nitride by reactive-ion-assisted magnetron sputtering deposition, *Jpn. J. Appl. Phys.* 45 (2006), pp.6405-6410.
- [61] D. Rosenthal, Mathematical theory of heat distribution during welding and cutting, *Weld. J.* 20 (1941), pp.220-234.
- [62] D.H. Kang, K.J. Son, Y.S. Yang, Analysis of laser weldment distortion in the EDFA LD pump packaging, *Finite Elem. Anal. Des.* 37 (2001), pp.749-760.
- [63] P. Gordon, B. Balogh, B. Sinkovics, Thermal simulation of UV laser ablation of polyimide, *Microelectron. Reliab.* 47 (2007), pp.347-353.
- [64] T.J. McKee, How lasers mark, *Electron. Technol.* 7 (1996), pp.27-31.
- [65] H.B. Liu, D.P. Wan, D.J. Hu, Microstructure and wear behavior of laser-textured and micro-alloyed Co-based WC and TiC composite sintered-carbide coating, *J. Mater. Process. Technol.* 209 (2009), pp.805-810.
- [66] R.S. Razavi, M. Salehi, M. Monirvaghefi, G.R. Gordani, Laser surface treatment of electroless Ni-P coatings on Al356 alloy, *J. Mater. Process. Technol.* 195 (2008), pp.154-159.
- [67] A. Erdemir, Review of engineered tribological interfaces for improved boundary lubrication, *Tribol. Int.* 38 (2005), pp.249-256.
- [68] A. Kovalchenko, O. Ajayi, A. Erdemir, G. Fenske, I. Etsion, The effect of laser surface texturing on transitions in lubrication regimes during unidirectional sliding contact,

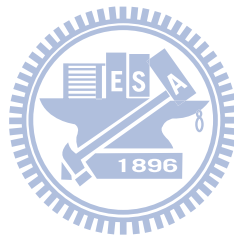
- Tribol. Int. 38 (2005), pp.219-225.
- [69] X. Wang, K. Kato, K. Adachi, K. Aizawa, The effect of laser texturing of SiC surface on the critical load for the transition of water lubrication mode from hydrodynamic to mixed, Tribol. Int. 34 (2001), pp.703-711.
- [70] D.P. Wan, B.K. Chen, Y.M. Shao, S.L. Wang, D.J. Hu, Microstructure and mechanical characteristics of laser coating-texturing alloying dimples, Appl. Surf. Sci. 255 (2008), pp.3251-3256.
- [71] W.M. Steen, Laser Material Processing, Springer-Verlag, London, 1991.
- [72] D.T. Pham, S.S. Dimov, P.V. Petkov, Laser milling of ceramic components, Int. J. Mach. Tools Manuf. 47 (2007), pp.618-626.
- [73] N.B. Dahotre, Laser surface engineering, Adv. Mater. Process. 160 (7) (2002), pp.35-39.
- [74] Y. Zhou, B. Wu, Experimental study on infrared nanosecond laser-induced backside ablation of sapphire, J. Manuf. Processes 12 (2010), pp.57-61.
- [75] M.H. Yen, C.W. Huang, W.C. Hsu, T.H. Young, K. Zimmer, J.Y. Cheng, Crack-free micromachining on glass substrates by visible LIBWE using liquid metallic absorbers, Appl. Surf. Sci. 257 (2010), pp.87-92.
- [76] B. Hopp, T. Smausz, C. Vass, G. Szabó, R. Böhme, D. Hirsch, K. Zimmer, Laser-induced backside dry and wet etching of transparent materials using solid and molten tin as absorbers, Appl. Phys. A 94 (2009), pp.405-410.
- [77] X. Ding, Y. Yasui, Y. Kawaguchi, H. Niino, A. Yabe, Laser-induced back-side wet etching of fused silica with an aqueous solution containing organic molecules, Appl. Phys. A 75 (2002), pp.437-440.
- [78] K. Zimmer, R. Böhme, B. Rauschenbach, Laser etching of fused silica using an adsorbed toluene layer, Appl. Phys. A 79 (2004), pp.1883-1885.
- [79] B. Hopp, Cs. Vass, T. Smausz, Laser induced backside dry etching of transparent materials, Appl. Surf. Sci. 253 (2007), pp.899-904.



- [80] K. Zimmer, R. Böhme, C. Vass, B. Hopp, Time-resolved measurements during backside dry etching of fused silica, *Appl. Surf. Sci.* 255 (2009), pp.9617-9621.
- [81] K. Zimmer, R. Böhme, M. Ehrhardt, B. Rauschenbach, Mechanism of backside etching of transparent materials with nanosecond UV-lasers, *Appl. Phys. A* 101 (2010), pp.405-410.
- [82] J.J. Yoh, A.B. Gojani, Metal and polymer melt jet formation by the high-power laser ablation, *Appl. Surf. Sci.* 256 (2010), pp.2423-2427.
- [83] <http://www.itrc.org.tw/Research/Product/Vacuum/thinfilm.php>
- [84] <http://www.firsttenangstroms.com/faq/IntroductionToTheFta188.html>
- [85] A.B.C. Cassie, S. Baxter, Wettability of porous surfaces, *Trans Faraday Soc.* 40 (1944), pp.546-551.
- [86] H. Yamada, T. Sano, T. Nakayama, I. Miyamoto, Optimization of laser-induced forward transfer process of metal thin films, *Appl. Surf. Sci.* 197 (2002), pp.411-415.
- [87] A. Castelo, D. Nieto, C. Bao, M.T. Flores-Arias, M.V. Pérez, C. Gómez-Reino, C. López-Gascón, G.F. de la Fuente, Laser backwriting process on glass via ablation of metal targets, *Opt. Commun.* 273 (2007), pp.193-199.
- [88] M.T. Flores-Arias, A. Castelo, C. Gomez-Reion, G.F. de la Fuente, Phase diffractive optical gratings on glass substrates by laser ablation, *Opt. Commun.* 282 (2009), pp.1175-1178.
- [89] [http://www.eng.lhu.edu.tw/all\\_lab/nano\\_lab/link\\_3.html](http://www.eng.lhu.edu.tw/all_lab/nano_lab/link_3.html)
- [90] S. Lee, D. Yang, S. Nikumb, Femtosecond laser micromilling of Si wafers, *Appl. Surf. Sci.* 254 (2008), pp.2996-3005.
- [91] O.R. Musaev, O.S. Kwon, J.M. Wrobel, D.-M. Zhu, M.B. Kruger, Evolution of InP surfaces under low fluence pulsed UV irradiation, *Appl. Surf. Sci.* 254 (2008), pp.5803-5806.
- [92] Y.C. Chim, X.Z. Ding, X.T. Zeng, S. Zhang, Oxidation resistance of TiN, CrN, TiAlN

and CrAlN coatings deposited by lateral rotating cathode arc, *Thin Solid Films* 517 (2009), pp.4845-4849.

- [93] O.K. Ezekoye, A.R. Drews, H.-W. Jen, R.J. Kudla, R.W. McCabe, M. Sharma, J.Y. Howe, L.F. Allard, G.W. Graham, X.Q. Pan, Characterization of alumina-supported with advanced electron microscopy Pt and Pt-Pd NO oxidation catalysts with advanced electron microscopy, *J. Catal.* 280 (2011), pp. 125-136.



## Vitas

**Shih-Feng Tseng** was born on October 25, 1978 in Hsinchu city, Taiwan. He received the B.Sc. and M.Sc. degrees in department of industrial education and in mechatronics engineering from National Changhua University of Education in Changhua in 2001 and 2003, respectively. He received the Ph.D. degree in Department of Mechanical Engineering from National Chiao Tung University in Hsinchu in 2011. His Ph.D. researches include the development of laser processing system for optoelectric and biomedical applications and the development of glass-molding process. He is currently an associate researcher at Instrument Technology Research Center, National Applied Research Laboratories. His research interests include studies of the laser material process, the fabrication and testing of optical components, and the optomechanical design and analysis.



## 簡 歷

|        |  |          |          |   |        |    |
|--------|--|----------|----------|---|--------|----|
| 姓名     | 曾釋鋒  | 性別       | 男        |  |        |    |
| 出生地    | 新竹市  | 出生日期     | 67.10.25 |   |        |    |
| 身高     | 168 cm   | 體重       | 78 kg    |   |        |    |
| 聯絡地址   | 新竹縣竹北市東海里東興路一段 871 號   |          |          |   |        |    |
| 聯絡電話   | (03)5501225  |          |          |   |        |    |
| 手機     | 0986-009677  |          |          |   |        |    |
| E-mail | <a href="mailto:tsengsf@itrc.narl.org.tw">tsengsf@itrc.narl.org.tw</a> ; <a href="mailto:feng10252002@yahoo.com.tw">feng10252002@yahoo.com.tw</a>  |          |          |   |        |    |
| 學歷     | 學位   | 學校名稱     | 科系       | 起   | 迄      | 地點 |
|        | 博士   | 國立交通大學   | 機械工程研究所  | 97/09   | 100/09 | 新竹 |
|        | 碩士   | 國立彰化師範大學 | 機電工程研究所  | 90/09   | 92/06  | 彰化 |
|        | 學士   | 國立彰化師範大學 | 工業教育學系   | 86/09   | 90/06  | 彰化 |
| 工作經驗   | 公司學校   |          | 職務       | 起迄時間  |        |    |
|        | 國研院儀器科技研究中心  |          | 副研究員     | 98/01~迄今  |        |    |
|        | 國研院儀器科技研究中心  |          | 助理研究員    | 94/01~97/12   |        |    |
|        | 國科會精密儀器發展中心  |          | 專案助理研究員  | 93/10~94/01   |        |    |
|        | 國立新竹高級工業職業學校   |          | 實習教師     | 92/09~93/06   |        |    |
| 榮譽     | <p>1.馬劍清、黃國政、張敬源、曾釋鋒，「透鏡偏心量測裝置及其量測方法」，台北國際發明展，獲頒<b>金牌獎</b>、波蘭人發明人協會頒發<b>特別獎</b>，2008。</p> <p>2.台灣雷射應用發展協會<b>永久名譽會員</b>(2008~迄今)。</p> <p>3.榮獲國研院儀器科技研究中心九十七年度<b>研究創新獎</b>個人組第二名。</p> <p>4.馬劍清、黃國政、張敬源、曾釋鋒，「A LENS MEASURING DEVICE AND METHOD APPLIED THEREIN」，德國紐倫堡發明展，獲頒<b>金牌獎</b>，2009。</p> <p>5.擔任 2009 AMPT 國際研討會中 High Energy Beam Process (HEBP)場次之<b>共同主席</b>。</p> <p>6.榮獲國研院儀器科技研究中心九十九年度<b>論文績優獎</b>個人組第一名。</p> |          |          |   |        |    |
| 專長     | 雷射加工與系統整合、玻璃模造技術開發、光機系統設計  |          |          |   |        |    |
| 電腦軟體   | TracePro、SolidWorks、CAMWorks、AutoCAD、ANSYS、Matlab  |          |          |   |        |    |

## Publications

### A. Referred National Journal Papers

1. 余宗儒、曾釋鋒、黃國政、郭慶祥，非球面負形拋光系統研製，科儀新知，第二十七卷第二期，pp.210-219，2005。
2. 林煒晟、陳炤彰、黃國政、曾釋鋒，軟式變焦鏡頭之研製，科儀新知，第二十八卷第四期，pp.82-92，2007。
3. 曾釋鋒、黃國政、陳明飛、蕭文澤，高功率二氧化碳雷射切割金屬材料模擬與分析，科儀新知，第二十九卷第六期，pp.50-57，2008。
4. 曾釋鋒、黃國政，雷射熱破裂技術於玻璃切割之應用，國研科技，第十八期，pp.58-65，2008。
5. 黃建堯、黃國政、郭朝輝、施至柔、曾釋鋒、周長彬，精密玻璃模造技術在微光學元件製造上之應用，科儀新知，第三十二卷第三期，pp.85-97，2010。

### B. Referred International Journal papers

1. Ming-Fei Chen, Wen-Tse Hsiao, Yu-Sen Ho, **Shih-Feng Tseng**, Yu-Pin Chen, **Laser patterning with beam shaping on indium tin oxide thin films of glass/plastic substrate**, Thin Solid Films, 518, pp.1072-1078, 2009. (SCI)
2. **Shih-Feng Tseng**, Wen-Tse Hsiao, Ming-Fei Chen, Kuo-Cheng Huang, Sheng-Yi Hsiao, Yung-Sheng Lin, Chang-Pin Chou, **Surface wettability of silicon substrates enhanced by laser ablation**, Applied Physics A: Materials: Science & Processing, 101, pp.303-308, 2010. (SCI)
3. **Shih-Feng Tseng**, Wen-Tse Hsiao, Kuo-Cheng Huang, Ming-Fei Chen, Chao-Te Lee, Chang-Pin Chou, **Characteristics of Ni-Ir and Pt-Ir hard coatings surface treated by pulsed Nd:YAG laser**, Surface and Coatings Technology, 205, pp. 1979-1984, 2010. (SCI)
4. **Shih-Feng Tseng**, Wen-Tse Hsiao, Kuo-Cheng Huang, Donyau Chiang, Ming-Fei Chen, Chang-Pin Chou, **Laser scribing of indium tin oxide (ITO) thin films deposited on various substrates for touch panels**, Applied Surface Science, 257, pp.1487-1494, 2010. (SCI)
5. **Shih-Feng Tseng**, Kuo-Cheng Huang, Donyau Chiang, Ming-Fei Chen, Sheng-Yi Hsiao, Yung-Sheng Lin, Chang-Pin Chou, **Hydrophobic templates with rough patterns fabricated by laser micromachining for liquid droplets generation**, Advanced Materials Research, 264-265, pp.1234-1239, 2011. (EI)

6. Kuo-Cheng Huang, Min-Wei Hung, **Shih-Feng Tseng**, Chi-Hung Hwang, **A Study on Thermal Fracture Processing Models Applied to Glass Substrate Cutting**, *Advanced Materials Research*, 264-265, pp.1252-1257, 2011. (EI)
7. Wen-Hong Wu, Kuo-Cheng Huang, **Shih-Feng Tseng**, **Multi-sphere mirror design of YAG laser applied for glass substrate cutting**, *Advanced Materials Research*, 264-265, pp.1246-1251, 2011. (EI)
8. Chien-Yao Huang, Kuo-Cheng Huang, Jun-Cheng Chen, Keng-Souo Chang, **Shih-Feng Tseng**, Chang-Pin Chou, **Development of a novel rapid manufacturing process for micro-cylindrical lens array**, *Advanced Materials Research*, 264-265, pp.78-83, 2011. (EI)
9. **Shih-Feng Tseng**, Chao-Te Lee, Kuo-Cheng Huang, Donyau Chiang, Chien-Yao Huang, Chang-Pin Chou, **Mechanical properties of Pt-Ir and Ni-Ir binary alloys for glass-molding dies coating**, *Journal of Nanoscience and Nanotechnology*, 2011. (SCI) (In press) (DOI: 10.1166/jnn.2011.3502)
10. Chien-Yao Huang, Jyh-Rou Sze, Kuo-Cheng Huang, Chao-Hui Kuo, **Shih-Feng Tseng**, Chang-Pin Chou, **The glass-molding process of planar-integrated micro-optical component**, *Optical review*, 18, pp.96-98, 2011. (SCI)
11. Yu-Chung Tsai, Chinghua Hung, Jung-Chung Hung, **Shih-Feng Tseng**, **Finite element prediction of the lens shape of molded optical glass lenses**, *Proceedings of the Institution of Mechanical Engineers, Part B, Journal of Engineering Manufacture*, 225, pp.224-234, 2011. (SCI)
12. Ming-Fei Chen, Yu-Sen Ho, Wen-Tse Hsiao, Tse-Hung Wu, **Shih-Feng Tseng**, Kuo-Cheng Huang, **Optimized laser cutting on light guide plates using grey relational analysis**, *Optics and Lasers in Engineering*, 49, pp.222-228, 2011. (SCI)
13. **Shih-Feng Tseng**, Wen-Tse Hsiao, Kuo-Cheng Huang, Chien-Yao Huang, Chang-Pin Chou, **Investigation of profile cutting on glass plates using a pulsed UV laser system**, *International Journal of Automation Technology*, 5, pp.270-276, 2011.
14. Wen-Tse Hsiao, **Shih-Feng Tseng**, Kuo-Cheng Huang, Yan-Hsin Wang, Ming-Fei Chen, **Pulsed Nd:YAG laser treatment of monocrystalline silicon substrate**, *International Journal of Advanced Manufacturing Technology*, 56, pp.223-231, 2011. (SCI)
15. **Shih-Feng Tseng**, Wen-Tse Hsiao, Donyau Chiang, Kuo-Cheng Huang, Chang-Pin Chou, **Mechanical and optoelectric properties of post-annealed fluorine-doped tin oxide films by ultraviolet laser irradiation**, *Applied Surface Science*, 257, pp. 7204-7209, 2011. (SCI)

16. **Shih-Feng Tseng**, Wen-Tse Hsiao, Kuo-Cheng Huang, Donyau Chiang, Ming-Fei Chen, Chang-Pin Chou, **Edge isolation of transparent conductive polymer (TCP) thin films on flexible substrates using UV laser ablation**, Journal of Nanoscience and Nanotechnology, 2011. (SCI) (Accept)
17. **Shih-Feng Tseng**, Wen-Tse Hsiao, Kuo-Cheng Huang, Donyau Chiang, **The effect of laser patterning parameters on fluorine-doped tin oxide films deposited on glass substrates**, Applied Surface Science, 257, pp.8813-8819, 2011. (SCI)
18. Wen-Tse Hsiao, **Shih-Feng Tseng**, Chao-Hui Kuo, Kuo-Cheng Huang, Donyau Chiang, Pin-Chiun Yao, Ming-Fei Chen, **Fabrication of electrodes on zinc oxide doped aluminum thin films using an ultraviolet laser direct-patterning technology**, Physics Procedia, 19, pp.456-465, 2011. (EI)

### C. National Conference Papers

1. 曾釋鋒、楊忠衡、陳明飛，具彈簧補償之氣靜壓導軌設計，The 18<sup>th</sup> National conference on mechanical Engineering，2001。
2. 曾釋鋒、林育廷、陳明飛，階梯扇形止推動壓軸承性能分析，The 18<sup>th</sup> National conference on mechanical Engineering，2001。
3. 林育廷、曾釋鋒、陳明飛，高速進給對具配流槽氣靜壓軸承特性分析，The 18<sup>th</sup> National conference on mechanical Engineering，2001。
4. 曾釋鋒、陳金安、陳明飛、謝銘雄，高速氣靜壓主軸止推軸承動態特性分析，The 19<sup>th</sup> National conference on mechanical Engineering，2002。
5. 張堯盛、曾釋鋒、陳明飛，聲光調制暨雷射都卜勒干涉術在主軸迴轉精度之應用研究，OPT 台灣光電科技研討會，2002。
6. 張堯盛、曾釋鋒、陳明飛，Zeeman 雙頻雷射干涉儀在 CNC 工具機動態循圓量測之研究分析，OPT 台灣光電科技研討會，2003。
7. 張堯盛、黃盛偉、曾釋鋒，奈米微型雷射干涉儀之應用研究，OPT 台灣光電科技研討會，2004。
8. 曾釋鋒、余宗儒、黃國政、郭慶祥，振動研磨對非球面鏡表面品質之研究，The 22<sup>th</sup> National conference on mechanical Engineering，2005。
9. 黃國政、余宗儒、曾釋鋒、郭慶祥，非球面鏡片之負形拋光系統，The 22<sup>th</sup> National conference on mechanical Engineering，2005。
10. 曾釋鋒、黃國政、郭慶祥、余宗儒、林文龍，補償調整機構在非球面光學元件加

工之應用研究，OPT 台灣光電科技研討會，2005。

11. 曾釋鋒、黃國政、吳文弘、郭慶祥，應用 CAD/CAM 系統發展非球面光學元件快速成形技術，第四屆精密機械與製造技術研討會，2006。
12. 黃國政、吳文弘、鄭源傑、曾釋鋒，玻璃基板之快速熱破裂切割研究，第四屆精密機械與製造技術研討會，2006。
13. 黃國政、曾釋鋒、余宗儒，螺旋式負形鑽石刀具應用於非球面玻璃研磨製程之研究，第五屆 SME 精密製造學術研討會，2006。
14. 張敬源、馬劍清、黃國政、曾釋鋒，光學鏡片之應力與變形檢測，The 23<sup>th</sup> National conference on mechanical Engineering，2006。
15. 曾釋鋒、余宗儒、黃國政、郭慶祥，非球面負形拋光之研磨參數最佳化研究，The 23<sup>th</sup> National conference on mechanical Engineering，2006。
16. 林煒晟、陳炤彰、黃國政、曾釋鋒，軟式變焦鏡頭光機設計之研究，The 23<sup>th</sup> National conference on mechanical Engineering，2006。
17. 王嘉偉、黃國政、洪景華、余宗儒、曾釋鋒，光學玻璃透鏡之熱壓成形研究，The 23<sup>th</sup> National conference on mechanical Engineering，2006。
18. 林煒晟、陳炤彰、汪怡欣、黃國政、曾釋鋒，氣壓控制變焦鏡頭之光學設計，OPT 台灣光電科技研討會，2006。
19. 黃國政、曾釋鋒、楊力權、陳炤彰，光學鏡片模仁加工參數之波前誤差補償法，OPT 台灣光電科技研討會，2007。
20. 黃國政、曾釋鋒、吳文弘、余宗儒，均勻研磨與拋光於非球面鏡加工之研究，The 25<sup>th</sup> National conference on mechanical Engineering，2008。
21. 張敬源、馬劍清、黃國政、曾釋鋒，光學鏡片傾斜與偏心之極化量測方法，AOI Forum & Show，2008。
22. 黃建堯、黃國政、陳俊成、張耿碩、曾釋鋒、周長彬，玻璃微柱狀鏡陣列之快速成形法，The 26<sup>th</sup> National conference on mechanical Engineering，2009。
23. 方治偉、黃建堯、曾釋鋒、黃國政、曾彥彬、周長彬，玻璃微透鏡陣列之複合成形技術，The 27<sup>th</sup> National conference on mechanical Engineering，2010。
24. 黃建堯、郭朝輝、蘇育政、蕭文澤、黃國政、曾釋鋒、周長彬，結合雷射與玻璃模造技術於玻璃晶片上微流道製程之研究，The 27<sup>th</sup> National conference on mechanical Engineering，2010。



#### D. International Conference Papers

1. **Shih-Feng Tseng**, Kuo-Cheng Huang, Ming-Fei Chen, Wen-Tse Hsiao, **Development of a Rapid Prototyping Technique for Aspherical Optical Components**, The 9<sup>th</sup> International Conference on Automation Technology, Taipei, Taiwan, 2007.
2. Ming-Fei Chen, Kuo-Cheng Huang, Yu-Pin Chen, Wen-Tse Hsiao, Yu-Sen Ho, **Shih-Feng Tseng**, **Investigation of laser micro-drilling for silicon wafer substrate**, The 8<sup>th</sup> Asia-Pacific Conference on Materials Processing, Guilin-Guangzhou, China, 2008.
3. Ming-Fei Chen, Kuo-Cheng Huang, Yu-Pin Chen, Wen-Tse Hsiao, Yu-Sen Ho, **Shih-Feng Tseng**, **Study on fabrication of taper microvias for aluminum alloy using UV laser**, The 8<sup>th</sup> Asia-Pacific Conference on Materials Processing, Guilin-Guangzhou, China, 2008.
4. Ching-Yuan Chang, Chien-Ching Ma, Kuo-Cheng Huang, **Shih-Feng Tseng**, **Development of a High-Speed Inspection Method for Optical Lenses Tilt and Decenter**, The 6<sup>th</sup> International Conference on Optics-photonics Design & Fabrication, Taipei, Taiwan, 2008.
5. Ming-Fei Chen, Wen-Tse Hsiao, Yu-Sen Ho, **Shih-Feng Tseng**, Yu-Pin Chen, **Laser beam shaping applied to patterning on indium tin oxide thin films of glass and pastic substrate**, The 2<sup>nd</sup> International Symposium on Transparent Conductive Oxides, Greece, 2008.
6. Ching-Yuan Chang, **Shih-Feng Tseng**, Chien-Ching Ma, Kuo-Cheng Huang, **Investigation of High-Speed Inspection Method for Optical Lenses with Tilt and Decenter**, Asia Pacific Conference on Optics Manufacture, Taipei, Taiwan, 2009.
7. Ming-Fei Chen, Wen-Tse Hsiao, Yu-Sen Ho, Hong-Wei Chang, Wei-Lun Huang, **Shih-Feng Tseng**, Yu-Pin Chen, **Effect of electronic properties on transparent conductive thin films by UV laser direct writing**, The 6<sup>th</sup> International Symposium on Transparent Oxide Thin Films for electronics and Optics, Tokyo, Japan, April 15-17, 2009.
8. Kuo-Cheng Huang, Min-Wei Hung, **Shih-Feng Tseng**, Chi-Hung Hwang, **A study on thermal fracture processing models applied to glass substrate cutting**, Advances in Materials and Processing Technologies (AMPT), Kuala Lumpur, Malaysia, October 26-29, 2009.
9. Wen-Hong Wu, Kuo-Cheng Huang, **Shih-Feng Tseng**, **Multi-sphere Mirror Design of YAG Laser Applied for Glass Substrate Cutting**, Advances in Materials and

- Processing Technologies (AMPT), Kuala Lumpur, Malaysia, October 26-29, 2009.
10. **Shih-Feng Tseng**, Kuo-Cheng Huang, Don-Yau Chiang, Ming-Fei Chen, Sheng-Yi Hsiao, Yung-Sheng Lin, Chang-Pin Chou, **Laser micromachining of rough patterned templates for generation of liquid droplets**, Advances in Materials and Processing Technologies (AMPT), Kuala Lumpur, Malaysia, October 26-29, 2009.
  11. Chien-Yao Huang, Kuo-Cheng Huang, Jun-Cheng Chen, Keng-Souo Chang, **Shih-Feng Tseng**, Chang-Pin Chou, **Development of a new rapid manufacturing process for micro-cylindrical lens array**, Advances in Materials and Processing Technologies (AMPT), Kuala Lumpur, Malaysia, October 26-29, 2009.
  12. **Shih-Feng Tseng**, Chao-Te Lee, Kuo-Cheng Huang, Don-Yau Chiang, Chien-Yao Huang, Chang-Pin Chou, **Investigation on protective coatings of Pt-Ir and Ni-Ir binary alloys for glass-molding dies**, The 4<sup>th</sup> NANOSMAT conference, Rome, Italy, October 19-22, 2009.
  13. **Shih-Feng Tseng**, Wen-Tse Hsiao, Ming-Fei Chen, Kuo-Cheng Huang, Sheng-Yi Hsiao, Yung-Sheng Lin, Chang-Pin Chou, **Surface wettability of silicon substrates enhanced by laser ablation**, The 10<sup>th</sup> International Conference on Laser Ablation (COLA), Singapore, November 22-27, 2009.
  14. **Shih-Feng Tseng**, Wen-Tse Hsiao, Kuo-Cheng Huang, Ming-Fei Chen, Chao-Te Lee, Chang-Pin Chou, **Nd:YAG Laser Surface Treatment of Pt-Ir and Ni-Ir Thin Films**, TACT 2009 International Thin Films Conference, Taipei, Taiwan, December 14-16, 2009.
  15. Chien-Yao Huang, Jyh-Rou Sze, Kuo-Cheng Huang, Chao-Hui Kuo, **Shih-Feng Tseng**, Chang-Pin Chou, **The glass-molding process of planar-integrated micro-optical component**, The 7<sup>th</sup> International Conference on Optics-photonics Design & Fabrication (ODF'10), Yokohama, Japan, April 19-21, 2010.
  16. Ching-Yuan Chang, Chien-Ching Ma, Kuo-Cheng Huang, **Shih-Feng Tseng**, **An Instrument Designed for Tilt and Decenter Measurements of Lenses Produced on Production Line**, The 7<sup>th</sup> International Conference on Optics-photonics Design & Fabrication (ODF'10), Yokohama, Japan, April 19-21, 2010.
  17. **Shih-Feng Tseng**, Wen-Tse Hsiao, Kuo-Cheng Huang, Chien-Yao Huang, Chang-Pin Chou, **Investigation of profile cutting on glass plates using a pulsed UV laser system**, Proceedings of 4<sup>th</sup> CIRP International Conference on High Performance Cutting, Gifu, Japan, October 24-26, 2010.
  18. Kuo-Cheng Huang, Wen-Hong Wu, **Shih-Feng Tseng**, Ching-Ching Yang, **An**

**asymmetric cutting on glass substrates based on thermal fracture theorem**, Proceedings of 4<sup>th</sup> CIRP International Conference on High Performance Cutting, Gifu, Japan, October 24-26, 2010.

19. Ming-Fei Chen, Yu-Sen Ho, Wen-Tse Hsiao, Pei-Sheng Lo, **Shih-Feng Tseng**, Kuo-Cheng Huang, **Fabrication of electrode trench on multicrystalline silicon solar cells using laser grooving technology**, The 36<sup>th</sup> Micro & Nano Engineering International Conference, Genoa, Italy, September 19-22, 2010.
20. **Shih-Feng Tseng**, Wen-Tse Hsiao, Donyau Chiang, Kuo-Cheng Huang, Ming-Fei Chen, Chang-Pin Chou, **Edge Isolation of Transparent Conductive Polymer (TCP) Films on a Flexible Substrate Using UV Laser Ablation**, The 5<sup>th</sup> NANOSMATE Conference, Oct. 19-21, 2010.
21. **Shih-Feng Tseng**, Wen-Tse Hsiao, Kuo-Cheng Huang, Donyau Chiang, Ching-Yuan Chang, Chang-Pin Chou, **Mechanical properties of the post-annealing fluorine-doped tin oxide (FTO) films by UV laser irradiation**, The 5<sup>th</sup> NANOSMATE Conference, Oct. 19-21, 2010.
22. Kuo-Cheng Huang, Wen-Hong Wu, **Shih-Feng Tseng**, Chi-Hung Hwang, **The mixed processing models development of thermal fracture and laser ablation on glass substrate**, Advances in Materials and Processing Technologies Conference (AMPT) 2010, Oct. 24-27, 2010.
23. Wen-Tse Hsiao, **Shih-Feng Tseng**, Donyau Chiang, Kuo-Cheng Huang, Ming-Fei Chen, **High positioning accuracy of a dual-axis feeding system enhanced by using error compensation methods for UV laser processing system**, IEEE I2MTC, Hangzhou, P. R. China, May 10-12, 2011.
24. **Shih-Feng Tseng**, Wen-Tse Hsiao, Kuo-Cheng Huang, Donyau Chiang, **Laser patterning of fluorine-doped tin oxide (FTO) thin films deposited on glass substrates for touch screen applications**, International Conference on Optics in Precision Engineering and Nanotechnology, Singapore, March 23-25, 2011.
25. Wen-Tse Hsiao, **Shih-Feng Tseng**, Chao-Hui Kuo, Kuo-Cheng Huang, Donyau Chiang, Pin-Chiun Yao, Ming-Fei Chen, **Fabrication of electrodes on zinc oxide doped aluminum thin films using an ultraviolet laser direct-patterning technology**, International Conference on Optics in Precision Engineering and Nanotechnology, Singapore, March 23-25, 2011.

#### E. Patents

1. 曾釋鋒、黃國政、郭慶祥、余宗儒，**光學元件自動拋光補償調整裝置及方法**，中

- 中華民國發明專利證號：I291569，2007。
- 許巍耀、曾釋鋒、林宇仁，用於檢測設備的透鏡拼接方法及其系統，中國發明專利證號：CN101315470，2008。
  - 黃國政、黃建堯、曾釋鋒、吳文弘，Schneidevorrichtung zum Schneiden von hart-sprödem Material，德國發明專利證號：DE102007050872，2009。
  - 黃建堯、曾釋鋒、黃國政，用於硬脆材料之快速破裂切割裝置，中華民國發明專利證號：I332425，2010。
  - 黃國政、林煒晟、黃鼎名、曾釋鋒，光學元件的交界面輪廓之檢測方法及其裝置，中華民國發明專利證號：I336765，2011。
  - 黃國政、黃建堯、曾釋鋒、吳文弘，硬脆材料切割裝置，中華民國發明專利證號：I341242，2011。
  - 曾釋鋒、林宇仁、黃國政、吳文弘、許偉昌，利用折反式望遠之顯微取像系統，中華民國發明專利證號：I342408，2011。
  - 黃國政、黃建堯、曾釋鋒、吳文弘，CUTTING DEVICE FOR CUTTING HARD-BRITTLE MATERIAL，美國發明專利證號：US07919724，2011。
  - 馬劍清、張敬源、黃國政、曾釋鋒，A LENS MEASURING DEVICE AND METHOD APPLIED THEREIN，美國發明專利證號：US07969563，2011。
  - 許巍耀、曾釋鋒、林宇仁，用於檢測設備的透鏡拼接方法及其系統，中華民國發明專利證號：I348022，2011。

#### F. Book

- 曾釋鋒，光學元件精密製造與檢測，第 3.5 節-常用的晶體材料特性、第 4.2 節-英國光學製圖標準、第 11.1 節-形狀精度、第 11.2 節-表面粗糙度，全華科技出版社，2007.06。

#### G. Other Publications

- 曾釋鋒、陳明飛，氣體靜壓平面止推軸承設計，機械月刊，第二十八卷第三期，pp.96-110，2002。
- 曾釋鋒、陳明飛、張堯盛，單頻雷射暨麥克森干涉技術在高速氣靜壓主軸動平衡校正之應用研究，機械月刊，第二十九卷第三期，pp.460-473，2003。
- 曾釋鋒，高功率 CO<sub>2</sub> 雷射應用於金屬加工市場，大中華工具機展專刊機械五金總覽，經濟日報，pp.210-219，2009。

4. 曾釋鋒，雷射加工技術於太陽能產業之應用，台灣雷射，第四期，台灣雷射應用發展協會，pp.7-14，2011。

